INVESTIGATING THE INTERNAL STRESS/STRAIN STATE OF THE FOOT USING MAGNETIC RESONANCE IMAGING AND FINITE ELEMENT ANALYSIS

by

MARC THOMAS PETRE

Submitted in partial fulfillment of the requirements
for the degree of Doctor of Philosophy

Dissertation Adviser: Peter R. Cavanagh, Ph.D., D.Sc.

Department of Biomedical Engineering
Case Western Reserve University

August, 2007

CASE WESTERN RESERVE UNIVERSITY

SCHOOL OF GRADUATE STUDIES

We hereby approve the dissertation of

Marc Thomas Petre

candidate for the Ph.D. degree *.

(signed) Patrick Cragg
(chair of the committee)

Peter R. Cavanagh

Vassilis Panoskaltsis

Xin Yu

Brian Davis

Ahmet Erdemir

(date) May 15, 2007

*We also certify that written approval has been obtained for any proprietary material contained therein.

Table of Contents

List of Tables

List of Figures

Acknowledgements

This work would not have been possible without the suggestions, comments, and support of my committee members. This research relies on, intermingles with, and hopefully aids the strong work of my lab mates and friends, Sachin Budhabhatti, Tammy Owings, and Scott Sibole. Steve Fening was a much appreciated source of comments, suggestions and encouragement throughout. I am also grateful for enriching interactions with clinical collaborators Georgeanne Botek, DPM, James Hall, DPM, Paul Tokar, RN, Debra Kostar, RN, and Tiffany Johnson, MA.

I am thankful for the funding and opportunities provided by National Institutes of Health training grants T32 EB04314 & T32 AR05095 which supported me during my graduate work. Much of the advanced equipment needed to complete this work was funded by National Institutes of Health grant 5R01 HD037433 and additional support for the research contained in this dissertation was provided by the Cleveland Clinic Research Programs Council.

Investigating the Internal Stress/Strain State of the Foot Using Magnetic Resonance Imaging and Finite Element Analysis

Abstract

by

Marc Thomas Petre

It is known that mechanical forces acting within the soft tissues of the foot can contribute to the formation of neuropathic ulcers. Unfortunately, only surface measurements (plantar pressure) are used clinically to estimate foot risk due to mechanical loading. In the absence of equipment to monitor the internal stress and strain states, it is currently unknown how these surface measurements relate to what is happening inside of the foot.

Magnetic resonance imaging (MRI) has the potential to provide high resolution *in vivo* images of the internal structure of the foot. When combined with a device capable of applying loads to the limb during imaging, MRI can be used to visualize 3-dimensional internal strains. If the load applied during imaging is known, finite element models can be used to estimate the internal stress state which corresponds to the visualized deformation.

This dissertation describes the development and use of an MRI-compatible loading device to perform an *in vivo* load-deformation experiment on the human forefoot, a common site of neuropathic ulceration. The collected load-displacement field data was used in conjunction with a novel, 3-dimensional,

layered-tissue finite element model of the forefoot to simultaneously optimize the material properties of three tissue layers: skin, plantar fat pad, and muscle.

2-dimensional and 3-dimensional finite element models of the forefoot incorporating separate skin, fat, and muscle tissue sections were used to investigate the relationship between peak plantar pressure and peak internal stress. To determine the effect of the clinical goal of lowering peak plantar pressures on the internal stress and strain measures, a cushioning foam mat was modeled underneath the forefoot.

The location of peak internal stresses (sub-metatarsal 3) did not agree with the location of peak plantar pressure (sub-metatarsal 2). Inserting a cushioning foam mat decreased the peak plantar contact pressure by 66%, but did not change the location of peak internal stresses and only decreased their magnitudes by about 2%. Internal stresses were, however, reduced by 78.5% in the skin near the site of peak plantar pressure. The 3-dimensional multi-tissue model developed in this study is the first of its kind and provides novel insight into the mechanical responses of foot tissues.

CHAPTER 1

Introduction

1.1 Background

Diabetes mellitus is a heterogeneous group of diseases characterized by the common trait of excessive levels of glucose in the blood. The systemic nature of diabetes leads to a wide range of interacting complications affecting all parts of the body including the vessels (angiopathy), kidneys (nephropathy), eyes (retinopathy), nerves (neuropathy), and feet. Diabetic foot complications are the number one cause of non-traumatic lower limb amputations in the United States and a person with diabetes has a ten times higher lifetime risk of amputation than a person without (ADA, 2002).

It has been reported that over 80% of all lower limb amputations in diabetes are preceded by a non-healing wound known as an ulcer (Pecoraro, et al., 1990). The development of foot ulcers is attributed to a combination of factors including control of blood sugar, vascular status, motor, sensory, and autonomic nervous function, patient compliance, activity level, and mechanical loading (Dinh and Veves, 2005, Reiber, 2001). The exact role of mechanical loading in the formation and development of ulcers is not known, but removal of mechanical loading has been shown to be critical for ulcer healing (Ulbrecht, et al., 2004). High concentrations of force are also anecdotally linked to locations of ulceration and in the one available prospective study on ulcer incidence and plantar pressure,

only the patients with abnormally high plantar pressures developed plantar ulcers (Veves, et al., 1992).

If people with diabetes are to maintain a normal, active lifestyle, then the forces exerted on the feet due to walking, stair climbing, and other daily activities cannot be removed or even reduced. Instead, risk due to mechanical loading must be decreased by altering the distribution of these forces to avoid high concentrations of force over small areas of tissue (i.e. high stresses). Therapeutic footwear typically implements such an approach, shifting load from areas of high stress, such as the metatarsal heads, to areas of low stress, such as the midfoot.

Researchers (and some technologically advanced diabetic foot clinics) evaluate foot risk due to mechanical loading by measuring the distribution of contact forces acting on the plantar surface of the foot (Bus and de Lange, 2005, Perry, et al., 2002). The efficacy of therapeutic footwear (Mueller, et al., 2006) and ulcer healing strategies (Petre, M., et al., 2005) are similarly evaluated by measuring the peak surface pressure within the device. Even though reduction of surface stress remains the main clinical goal, efforts to determine a safe pressure level, below which ulcers do not form, have been largely unsuccessful (Armstrong, et al., 1998). This is probably due a combination of the multifactorial etiology of ulceration, wide inter-patient variation, and a general lack of understanding of the way surface stresses contribute to the formation of ulcers.

Many experts have theorized that ulcers begin subcutaneously and progress to the skin's surface (Brand, 1978, Delbridge, et al., 1985, IWGDF,

2005). Unfortunately, current measurement techniques only provide information about what is happening at the exterior surface of the skin. Studies in other areas of the body, such as the buttocks which is another area at high risk for ulceration, have implied that measured contact stresses do not correlate well with stresses deeper inside of the tissues (Oomens, et al., 2003).

In the absence of a means to experimentally measure the internal stress state of the foot, a numerical model may be used predict the internal state. The accuracy of the model prediction depends on realistic model geometry, boundary conditions, and material descriptions. The use of finite element (FE) modeling to predict internal foot stresses is currently limited by a lack of anatomically correct, 3-dimensional, multi-tissue geometry and accurate descriptions of the mechanical properties of foot tissues.

1.2 Objectives

The end goal of this investigation was to use FE modeling to make predictions about the internal stress-strain state of the foot at the moment in the gait cycle when contact pressure beneath the metatarsal heads reached a peak. Comparison of internal stresses to contact stresses at this moment in time might provide insight into ulcer formation and its relationship to the most common clinical evaluation tool, plantar contact pressure measurement.

Achieving this goal required the gathering of accurate inputs to the FE model in the form of measured loading boundary conditions, an anatomically accurate 3-dimensional FE mesh, and subject-specific tissue mechanical properties. The following three specific aims were pursued:

SPECIFIC AIM 1: Develop a device capable of applying gait-like loading to the foot during magnetic resonance imaging (MRI).

SPECIFIC AIM 2: Use inverse finite element modeling and data from an MRI load-deformation experiment to determine material parameters for various foot tissues.

SPECIFIC AIM 3: Use finite element modeling to evaluate the relationship between peak plantar pressure and peak internal stress.

1.3 Dissertation Overview

The remainder of this dissertation is comprised of three sequential studies designed to measure and characterize the mechanical responses of plantar foot tissues to loading and then use this information to predict some clinically relevant, but presently un-measurable, internal variables. Each chapter contains a review of the literature relevant to the portion of the work it describes. A compiled list of references is supplied at the end of the dissertation.

Chapter 2 describes the development and application of a novel foot-loading device designed to apply known vertical and shear loads to the forefoot within the bore of an extremity MRI. A method for determining material parameters from the MRI load-deformation data using inverse finite element modeling is developed in Chapter 3. Chapter 4 describes the use of a novel layered finite element model with experimentally validated material parameters to investigate the relationship between surface pressure and internal stress and strain.

Chapter 5 draws conclusions from the combined results of all three studies and discusses possible future research directions. The two novel experimental techniques described in this work, in-vivo MRI load-deformation testing and optimization of material parameters from MRI image data, are described in greater detail in appendices A and B, respectively.

CHAPTER 2

An MRI-Compatible Foot-Loading Device for Assessment of Internal Strain

Marc Petre, Ahmet Erdemir, and Peter R. Cavanagh, *Journal of Biomechanics*, in review.

2.1 Abstract

It is well known that mechanical forces acting within the soft tissues of the foot can contribute to the formation of neuropathic ulcers in people with diabetes. Presently, only surface measurements of plantar pressure are used clinically to estimate risk status due to mechanical loading. It is not currently known how surface measurements relate to the three-dimensional internal stress and strain state of the foot. This article describes the development of a foot-loading device that will allow the direct observation of the internal state of strain of the foot under known forces in a magnetic resonance imaging (MRI) system.

Forces and plantar pressure distributions during normal walking were measured in 10 healthy young adults. One instant in the gait cycle, when pressure under the metatarsal heads reached a peak, was extracted for simulation in the MRI machine. T_1-weighted 3-D gradient echo MRI sets were collected as the simulated walking ground reaction force was incrementally applied to the foot by the novel foot-loading device.

Incremental increases in force caused the soft-tissue thickness under the second metatarsal head to decrease rapidly at first and then reach a plateau. Plantar pressure measurements collected within the loading device were lower in magnitude and less focal than pressures measured during walking. This finding implies that although the device successfully applied full walking ground reaction forces to the foot, they were not distributed in the same manner as during walking. We conclude that the foot-loading device can be used in combination with an MRI system to determine *in vivo* foot tissue material properties and examine the relationship between surface loading and internal stress.

2.2 Introduction

Peripheral neuropathy is a long-term complication of diabetes mellitus that results in a loss of protective sensation in the distal extremities. Patients lose the ability to recognize damaging trauma, and this misrecognition can lead to the formation of neuropathic foot ulcers. The link between mechanical loading and ulceration is not well understood, but it is known that neuropathic ulceration does not occur in the absence of mechanical loading. In addition, a critical component of any strategy to heal neuropathic ulcers is the removal of interface loads, either through total removal of load (bed rest) or an ambulatory off-loading device such as a total contact cast (Ulbrecht, et al., 2004). Laboratory experiments have shown that repetitive application of moderate loads can induce neuropathic ulceration in rats (Hall and Brand, 1979). Although these facts imply that mechanical loading plays an important role in the formation, development, and

persistence of neuropathic ulcers, it remains unclear exactly how or where damage begins.

Many experts believe that neuropathic ulcers begin internally and progress to the skin surface through repetitive loading (Brand, 1978, Delbridge, et al., 1985, IWGDF, 2005). Suggested tissue damage mechanisms include overload of tissues (Thompson, 1988), repetitive application of moderate stress (Dinh and Veves, 2005), carpet-like stretching and bunching of the skin (Davis, 1993), and elevated intracellular calcium due to high strain rate loading (Landsman, et al., 1995). It is likely that ulceration is induced by combinations of many or all of the suggested damage mechanisms, which depend on the way that external stress is transmitted to the tissue layers within the foot.

In the absence of a method to measure internal foot stress and strain, the level of risk for ulceration due to mechanical loading is currently evaluated by measuring the forces acting on the plantar surface of the foot (Armstrong, et al., 1998, Bus and de Lange, 2005). It has also recently been suggested that skin-surface temperature of the foot may be another important predictor (Lavery, et al., 2007). Therapeutic footwear, the main tool for preventing foot ulceration, is designed with the primary goal of reducing peak plantar pressure. It is currently unclear how the clinical goal of lowering peak surface pressure relates to the goal of reducing potentially damaging internal stress. Data from other fields gives us insight in this regard: for example, numerical modeling of the buttocks has suggested that interface pressures alone are not sufficient to evaluate the benefits of a supporting surface (Oomens, et al., 2003). Thus, footwear interven-

tions that lower peak plantar pressures may or may not also reduce internal stresses.

Fluoroscopy, ultrasound, computed tomography (CT), and magnetic resonance imaging (MRI) all have the potential to provide information about the internal structure of the foot. When combined with a device capable of applying known loads to the limb during imaging, these techniques may be used to investigate the internal stress and strain distribution within the foot.

Fluoroscopy has been used with a plantar-pressure monitoring device to provide real-time imaging of dynamic foot deformation (Gefen, et al., 2000). Unfortunately, because of poor contrast between different types of soft tissue, studies have been limited to imaging the motion of bones within the soft tissue envelope. Fluoroscopy is also a transmission technique that creates 2-dimensional projections of 3-dimensional (3-D) structures. This difference makes it difficult to reconstruct deformations in closely spaced discrete structures, such as the tissue underneath the metatarsal heads (MTHs).

Ultrasound has been used alone to determine the thickness of structures, such as the forefoot fat pad, during standing (Gooding, et al., 1986, Gooding, et al., 1985) and walking (Cavanagh, 1999). It has also been used in combination with a force measurement device to characterize the mechanical properties of the human heel pad (Erdemir, et al., 2006). Ultrasound is relatively inexpensive and portable, but its utility is restricted by depth limitations, shadowing by bones, and relatively poor soft-tissue contrast.

A CT-compatible loading device has been developed to investigate deformations within prosthetic limbs (Madsen, et al., 2000) and in the diabetic foot (Smith, K. E., et al., 2000). Smith et al. applied a total vertical load of 50% of body weight with the foot fixed in 15° of plantar flexion to simulate the late stance phase of walking. No shear force was applied and, like fluoroscopy, CT provided poor contrast between individual soft tissue layers.

MRI is well suited for imaging internal strains because it provides exceptional soft-tissue contrast without exposing the subject to ionizing radiation. MRI has been successfully used to visualize the *in vivo* deformation of soft tissue in the buttocks where decubitus ulcers often form (Reger, et al., 1990). Elastography (Weaver, et al., 2005) and other MR deformation monitoring techniques (Gefen, et al., 2001) have been used to estimate the elastic response of foot tissue, but none of the MR techniques applied to date have explored the 3-D, nonlinear relationship between external force and internal stress or strain. The goal of this investigation was to develop a device capable of applying known normal and shear loads to the foot during the *in vivo* collection of MR images to fulfill the requirements for 3-D investigation of the internal deformations of the foot.

2.3 Methods

Ten healthy young adults, five female and five male, volunteered to participate in the study (Table 2.1). The research protocol was approved by the Institutional Review Board of the Cleveland Clinic, and all subjects signed informed consent documents prior to participation. Subjects were screened to

exclude foot deformity, prior foot fracture or surgery, and history of diabetes or vascular disease. Pregnant women and persons with metallic implants of any type were also excluded for MRI safety reasons. The presence of protective sensation was confirmed using a 10-g Semmes-Weinstein monofilament on the hallux, MTHs, and heel. Pedal and posterior tibial pulses were palpated to verify good vascular status. The right foot was arbitrarily chosen for testing on all subjects.

Table 2.1. Subject characteristics. Young healthy adults were selected for this first study using the new device to evaluate any discomfort experienced during loading.

Subject	Gender	Age (yrs)	Height (m)	Mass (kg)
1	Male	22	1.83	91.6
2	Male	21	1.68	61.0
3	Male	21	1.74	80.7
4	Male	22	1.73	76.2
5	Male	29	1.65	68.0
6	Female	20	1.65	76.2
7	Female	29	1.64	75.7
8	Female	18	1.63	61.2
9	Female	18	1.63	71.0
10	Female	21	1.63	76.0
Mean (± std dev):		**22 (±4)**	**1.68 (±0.07)**	**73.8 (±9.1)**

In order to apply realistic loading to subjects' feet within the MRI bore, forces acting on the right foot during normal walking were measured. Fifteen walking trials were collected, with subjects taking their first step onto a combined-measurement platform. This platform consisted of an Emed-X® pressure sensitive array (Novel, Inc., Minneapolis, MN) firmly attached to the top of a force plate

(Kistler Instrument Corp., Amherst, NY) (Figure 2.1). A digital camcorder was used to simultaneously capture the sagittal plane movement of the foot at 30 Hz during the first step. The walking plantar pressure distribution was collected with a spatial resolution of four sensors per square centimeter at a frequency of 100 Hz, and the 3-D ground reaction force (GRF) was collected at a frequency of 1000 Hz.

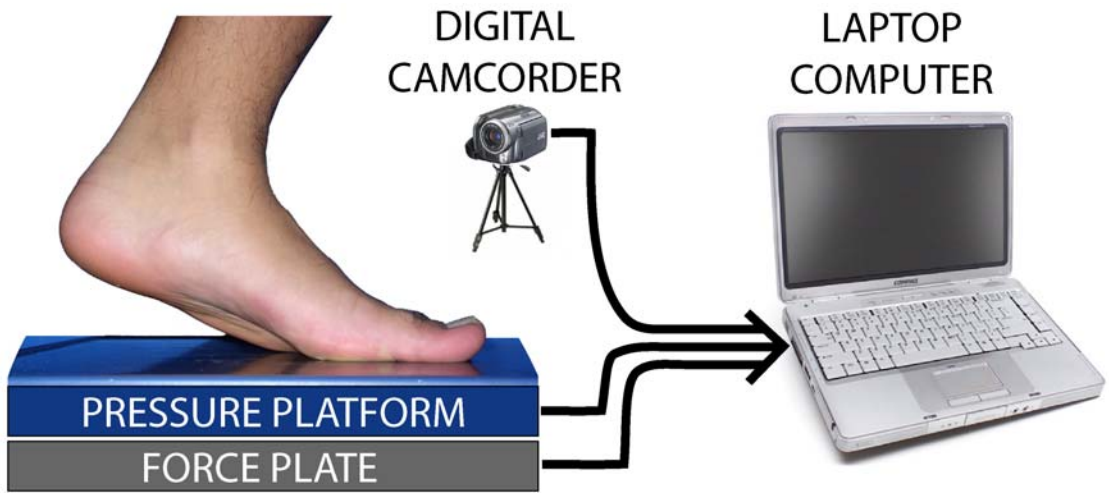

Figure 2.1. Experimental set-up for simultaneous collection of the walking ground reaction force (GRF), plantar pressure distribution, and sagittal pose. The information obtained from this experiment was used to apply realistic forces to the foot within the MR imager.

Only one instant from the gait cycle was simulated within the MRI bore. As the areas under the MTHs are common sites of neuropathic ulceration, the instant when MTH pressure reached a peak was chosen for simulation. Peak pressure was chosen rather than peak forefoot force because the former indicates the highest concentration of force over a small area of tissue. For each

trial, the GRF (3-D), plantar pressure distribution, and sagittal plane pose of the subject's foot were extracted at the instant of peak MTH pressure. Values and distributions were averaged over trials to obtain subject-specific loading schemes to be applied within the MRI bore (Table 2.2).

Table 2.2. Average loading conditions extracted from force platform and video measurements of barefoot walking trials. The instant when peak MTH pressure occurred is expressed as a percentage of the stance phase. The horizontal force angle was measured relative to the A-P axis with an angle of 0º indicating that the net horizontal force acted straight from second toe to heel and an angle of 90º indicating that the force acted straight from medial to lateral. Sagittal plane pose was described by the angle of inclination as measured to the base of the elevated heel.

Subject	Stance Phase (%)	Vertical Force (N)	Net Horizontal Force (N)	Horizontal Force Angle (Deg)	Inclination (Deg)
1	77.2	688.3	31.3	19	30.5
2	81.2	485.2	17.1	50	30.9
3	80.3	588.5	34.2	25	26.4
4	82.6	582.0	25.2	68	30.8
5	79.7	509.1	37.4	47	27.4
6	77.8	620.0	19.3	52	24.7
7	83.8	643.5	33.2	42	35.0
8	82.9	497.7	34.0	59	27.8
9	62.9	458.2	22.4	22	9.4
10	76.9	489.4	18.6	46	14.1
Mean (± std dev):	**78.5 (± 6.0)**	**556.2 (± 78.6)**	**27.3 (± 7.6)**	**43 (± 16)**	**26 (± 8)**

Relatively long MR scan times and uncomfortable foot position made voluntary application of constant loading within our small-bore MR imager extremely difficult. For example, even with visual force feedback, it would be difficult for subjects to maintain the prescribed vertical and horizontal forces for the duration of a 3.5-min scan with their foot in the maximally dorsiflexed position required by a small-bore extremity MR imager. Because of this experimental limitation, efforts were focused on the development of a device to apply loading to the passive foot.

The foot-loading device was constructed entirely out of polycarbonate, Delrin® (DuPont, Parkersburg, WV), and acrylic polymers to ensure MR compatibility and patient safety. The loading device was large enough to cover the forefoot and housed two small hydraulic pistons, one for applying a vertical force, and one for applying the net horizontal shear load (a vector addition of the anterior-posterior and medial-lateral shear components) (Figure 2.2). The piston housing insert could be rotated to apply the net horizontal load at any angle. The theoretically linear relationship between piston pressure and output force was verified by placing the pistons against a load cell, applying known pressures, and recording the force output (R^2 = 0.99 for both pistons). Hand pumps and pressure gauges located in the MR control room were used to adjust and monitor piston force during image collection.

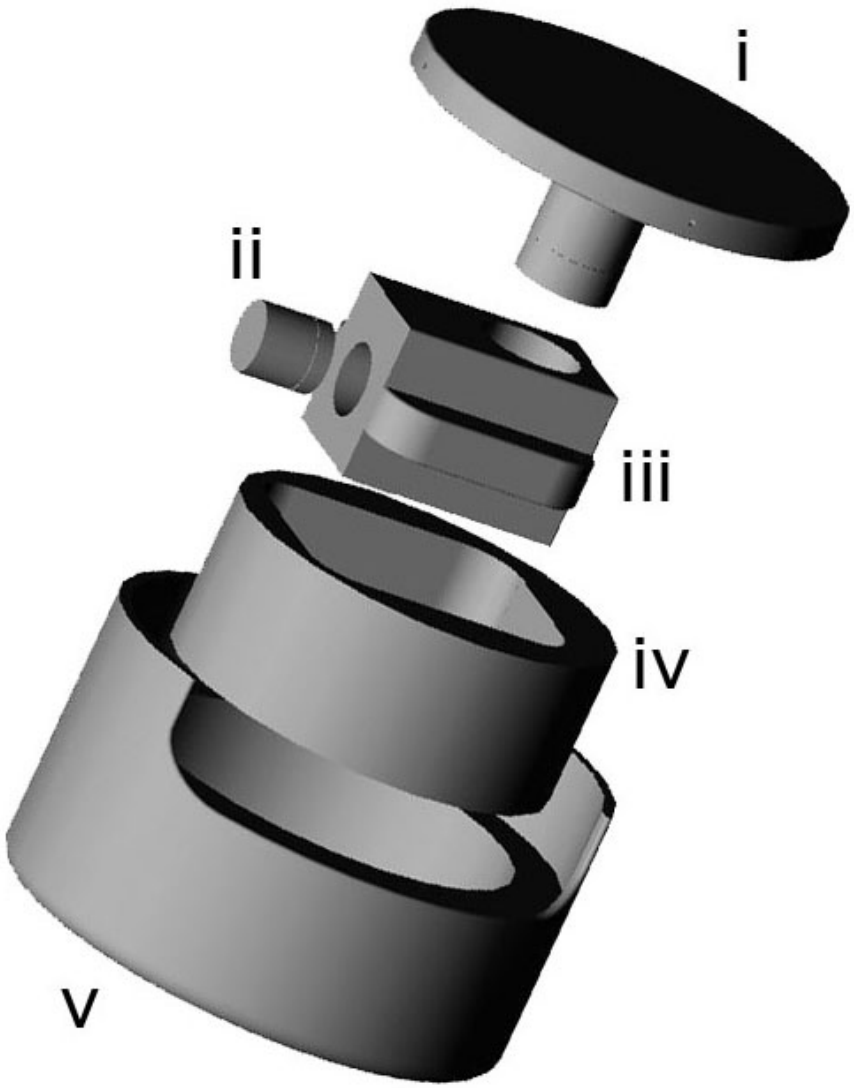

Figure 2.2. An exploded view of the foot-loading device assembly. The forefoot rests on a circular loading plate, which is connected to the vertical loading piston rod (i). A horizontal piston applies the net shear force (ii). Both pistons rest inside a piston housing (iii) that is free to slide horizontally inside of a rotating insert (iv). The rotating insert is fixed at the desired net shear-force angle relative to the outer housing (v) using a nylon set screw. The device is shown assembled in Figure 2.3.

Passive loading required the device to be firmly attached to the foot. Fiberglass casting material was used to secure the loading device to the foot and maintain the prescribed sagittal plane pose (Figure 2.3). Cast application began with a cotton stockinette that covered the foot and ankle everywhere except for the plantar surface of the forefoot, which was to come into contact with the loading plate. Only a single layer of cast padding was used over the stockinette so that the fiberglass was able to make intimate contact with the dorsum of the foot. This method allowed the force applied to the bottom of the foot to be carried by the dorsum with minimal soft-tissue deformation and discomfort.

Figure 2.3. The loading device was attached to the subjects' feet using fiberglass casting material. Here, the medial half of the cast has been removed to show the device beneath and the Pliance® pressure sensitive array fixed to the top of the loading plate.

The loading device applied the subject's GRF as measured in the walking experiments, but it was unclear whether or not this load would be distributed throughout the forefoot in a manner similar to walking. This question was explored by the collection of plantar pressure distribution within the loading device using a thin flexible Pliance® array (Novel, Inc., Minneapolis, MN) placed between the forefoot and the foot-loading plate prior to cast application (Figure 2.3). The array contained 256 capacitive pressure sensors with a spatial resolution of 5.2 sensors per square centimeter sampled at a rate of 87 Hz. The array was large enough to capture pressure beneath the main area of interest, the MTHs, but not pressures under the toes. Expected simulation of barefoot walking pressures required the sensor to be calibrated over the range of 0-1000 kPa.

Use of the pressure measurement equipment was not possible within the MR bore, so pressure measurements under known loads were taken before the subjects entered the imaging suite, with the assumption that the loading was repeatable. This assumption was verified in a single subject by re-measuring the pressure distribution after imaging (peak pressure before imaging = 104 kPa; peak pressure after imaging = 100 kPa). In-device plantar pressures and image sets were collected in the unloaded state and with 25%, 50%, 75%, and 100% of the GRF applied. Loading in 25% increments allowed us to observe not only the final strain, but also the nonlinear evolution of that strain.

MRI series were collected in the unloaded state and at each loading increment using an Orthone® 1 T clinical extremity scanning system (ONI Medical Systems, Inc., Wilmington, MA) (Figure 2.4). Each series consisted of a T_1-

weighted 3-D gradient echo (3DGE) sequence used to obtain 54 axial slices through the forefoot, each slice having a thickness of 2 mm with no inter-slice gap (ET: 1, TR: 20.0, TE:7.7, freq: 260, phase: 192, flip: 15º). Each sequence took approximately 3.5 min to complete. After each sequence the load was removed, and the subject was allowed to rest for at least 30 seconds.

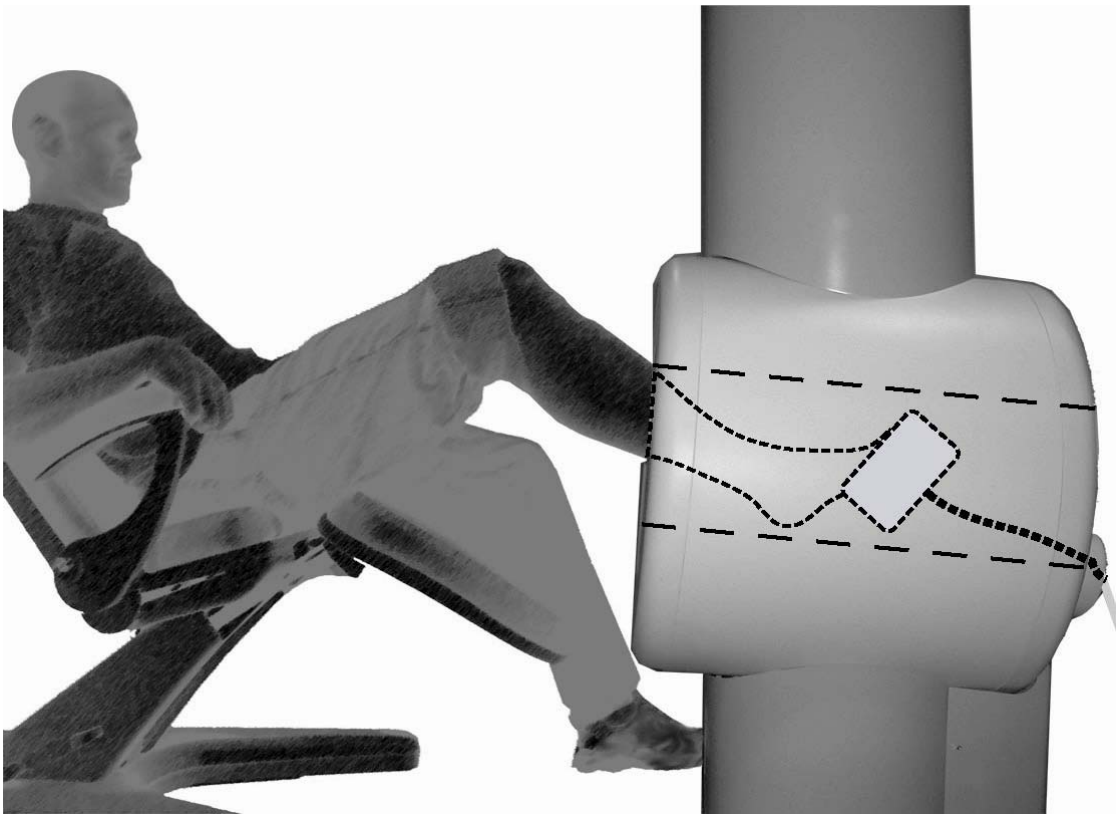

Figure 2.4. The small bore MRI used in this study. Hidden lines show the approximate size of the bore and the subject's foot attached to the loading device inside. Water tubing feeds the loading pistons from the back of the MRI bore. Piston force was monitored and adjusted from outside the imaging suite.

To provide a measurement of deformation, the plantar tissue thickness beneath the second MTH was measured at each loading level. The measurement was taken at the apparent minimum distance between the loading plate and the second MTH using a software line measurement tool (Figure 2.5). Loaded tissue thicknesses, t_i, were compared to the unloaded thickness, t_0, to calculate a relative compressive strain ε_i (Equation 2.1) at loading level *i*, where *i* is an element of the set [25% GRF, 50% GRF, 75% GRF, 100% GRF].

$$\varepsilon_i = 100 * \frac{(t_0 - t_i)}{t_0} \qquad \textbf{Equation 2.1}$$

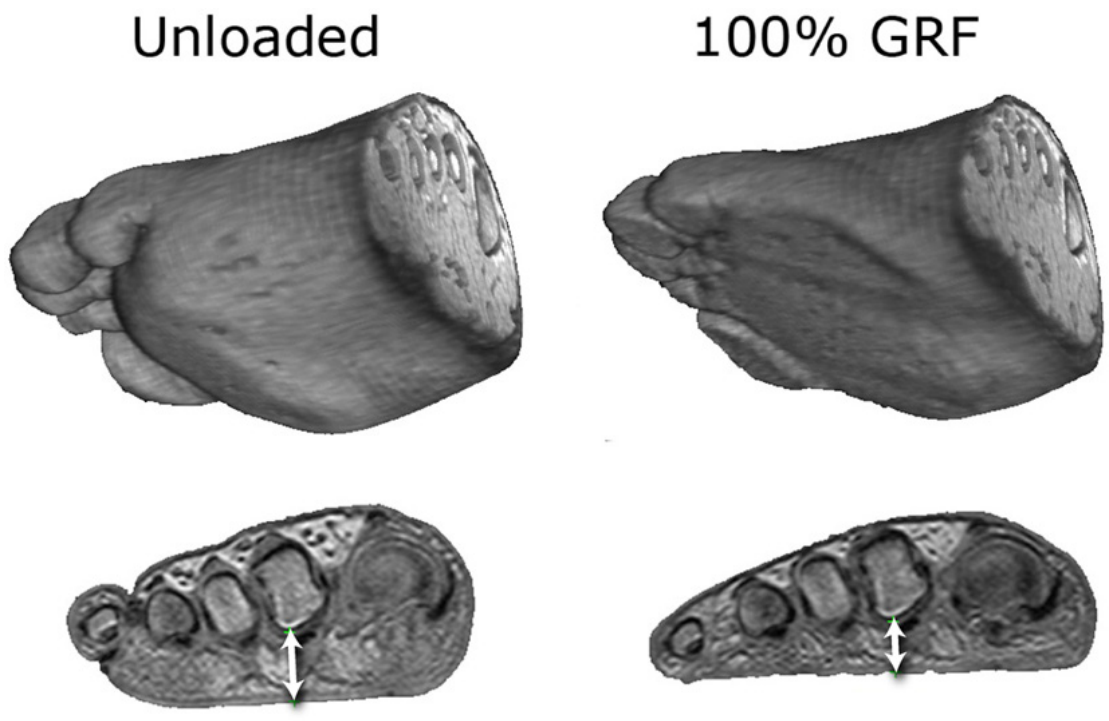

Figure 2.5. Solids (top) and slices through MTH2 (bottom) generated from MRI series collected from subject 10 in the unloaded and fully loaded states. The locations from which MTH2 plantar tissue thickness measurements were taken are marked with white arrows.

2.4 Results

The MRI loading device induced significant plantar soft tissue deformation in both the forefoot and toes (Figure 2.5). Incremental increases in the applied load resulted in diminishing increases in strain (Figure 2.6). For eight of 10 subjects, 70% of the final MTH2 plantar soft-tissue deformation had already occurred when only 25% of the total load had been applied. The trend was less apparent in subjects 3 and 7, who had significantly different foot structure in the vicinity of MTH2 where the second MTH was dorsally located with respect to both

Table 2.3. Peak plantar pressures during walking and during compression with the loading device. Peak pressures were generally lower in the loading device compared to barefoot walking. This is most likely due to differences between passive and active loading of the foot. Differences in the location of the peak MTH pressure may be due to altered frontal plane alignment (forefoot inversion/eversion) within the device.

Subject	Peak Walking MTH Pressure (kPa)	Walking Peak MTH Pressure Location	Peak In-Device MTH Pressure (kPa)	In-Device Peak MTH Pressure Location
1	461	MTH3	367	MTH1
2	608	MTH2	154	MTH2
3	396	MTH2	163	MTH1
4	478	MTH2	112	MTH1
5	353	MTH4	100	MTH4
6	589	MTH3	146	MTH3
7	592	MTH2	133	MTH2
8	566	MTH1	125	MTH1
9	439	MTH2	150	MTH1
10	438	MTH2	158	MTH1
Mean (± std dev):	**492 (± 91)**		**161 (± 75)**	

the first and third MTHs. The magnitude of MTH2 tissue strain varied considerably from subject to subject, possibly due to differences in foot structure, tissue material properties, and differences in subject-specific applied loads (Figure 2.6).

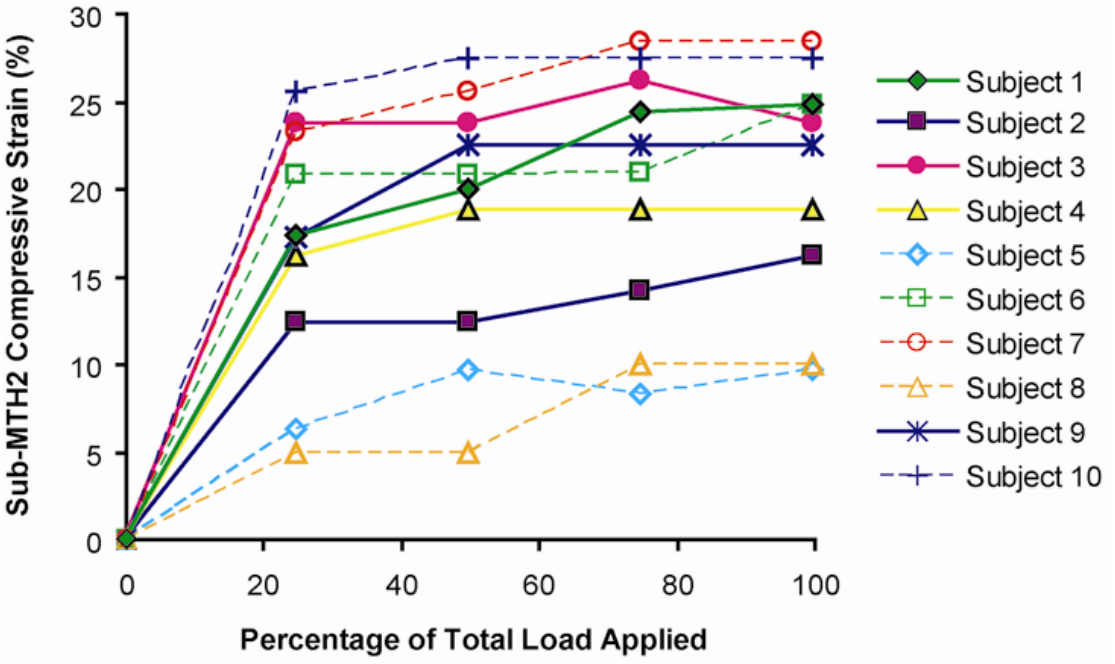

Figure 2.6. Vertical compressive strains computed from measurements of plantar tissue thickness beneath the second MTH (Figure 2.5). A large percentage of the strain observed at full load (100% GRF) is already present at much lower loads (25% GRF). There is significant inter-subject variation in the maximum strain, but not in the trend that strain accumulates quickly.

Compared to walking plantar pressure distributions, data collected in the loading device were less focal and exhibited lower peak pressures, even though the device was applying the same overall foot force as that measured during walking (Figure 2.7; Table 2.3). Peak MTH pressures within the loading device occurred under the same MTH as in the barefoot walking measurements for only

half of the subjects. Results from the other five subjects imply that the loading technique may artificially concentrate pressure under MTH1.

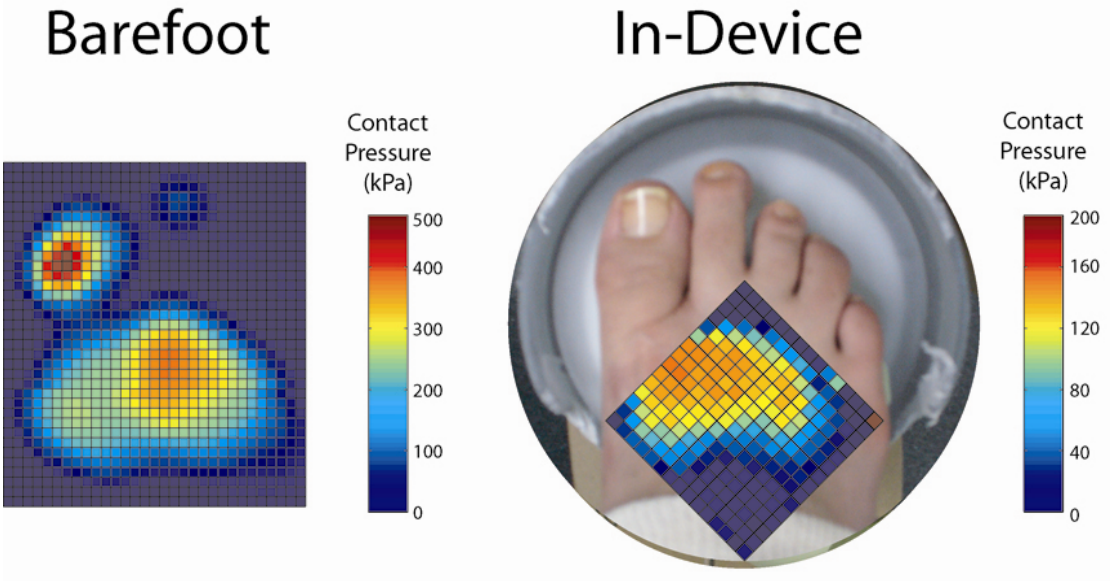

Figure 2.7. Exemplar plantar pressure distributions for subject 10 collected from barefoot walking and inside the loading device. Note the difference in color scales; the in-device pressures are less than half the magnitude of the barefoot walking pressures. These distributions are representative of the general trends - including lower peak pressures and fewer focal regions - within the loading device. The Pliance® measurement array was not large enough to capture in-device pressures beneath the toes.

2.5 Discussion and Conclusions

The foot-loading device successfully applied full walking GRFs to the foot during MR imaging. The volumetric image sets acquired are of sufficiently high resolution to examine individual tissue components in 3-D (Figure 2.5). However, differences between barefoot walking and in-device plantar pressure

distributions suggest that the MR loading technique used here is not an accurate simulation of barefoot walking. This is likely due to a combination of two factors; excessive loading of the toes and the passive nature of the foot during loading.

This study focused on tissue deformation beneath the MTHs, a common site of ulceration. However, the loading device applied the net GRF over both the MTH region and the toes. Unexpectedly low in-device peak MTH pressures could be due to an unrealistically large portion of the GRF being carried by the toes. Large deformations in toe tissues (Figure 2.5) imply that significant force was being carried by these structures, but the pressure measurement device used here was too small to capture information about toe loading. A larger pressure-sensitive array, such as a Pedar® insole sensor (Novel, Inc.), would be able to better evaluate the relative loading of the toes at the expense of decreased spatial resolution.

In barefoot walking, the GRF is transmitted to the body through the bones of the forefoot. Plantar soft tissue is compressed under the MTHs and the dorsal tissue remains relatively stress free. In this experiment, the force applied to the bottom of the foot was opposed by the dorsum, effectively compressing all tissues of the foot while leaving the metatarsal bones free to "float" within the soft-tissue envelope. The lack of active metatarso-phalangeal joint plantar flexion could explain decreases in the concentration and magnitude of peak pressure. It is also possible that the lack of active muscle forces may alter the material behavior of other tissues. For example, an active muscle is expected to behave differently in transverse compression than a passive muscle. Fortunate-

ly, the sub-MTH region of interest is primarily composed of passive tissues (tendon, ligament, joint capsule, fat pad, and skin) that are unlikely to undergo large changes in material properties with muscle activation.

Although the loading created within the MR imager does not appear to reproduce the interface pressures of gait, it does produce a valid force-displacement data set. These data are particularly well suited for the *in vivo* characterization of mechanical properties of foot tissues when used in conjunction with inverse finite element analysis (Erdemir, et al., 2006). The high soft-tissue contrast produced by MRI allows for the identification of individual tissues, limited only by the spatial resolution of the images. Image sets collected incrementally during loading provide not only peak strain information, but also information about the nonlinear evolution of strain needed for nonlinear material parameter determination. Peak pressures measured within the device were significantly lower than pressures taken during barefoot walking, but tissue strains reached a plateau (Figure 2.6), implying that all the important features of the material load-deformation curve can be reproduced from this data set.

The measurements of plantar tissue thickness beneath the second MTH presented here are a clinically interesting, preliminary measure of deformation. However, the data set does contain information about the internal strain distribution on a near continuum level and will allow 3-D strain maps of the entire forefoot (or any sub-region) to be generated. Current work is directed towards such a quantification of the internal 3-D stress and strain states using deformable image registration and finite element analysis.

Although not necessarily representative of gait, the contact pressure/internal loading relationships collected here provide important information. Once internal stress and strain maps have been created, it will be possible to compare peak plantar pressure to peak internal stress. If the location and magnitude of peak plantar pressure correlate well with the location and magnitude of peak internal stress, it will imply that the common clinical tool of plantar pressure measurement is a reasonable way to evaluate foot risk. If there is a poor correlation between surface and internal stresses, it will imply that new methods of risk evaluation may be needed.

Ideally, internal foot strain could be visualized in real time during stressful activity such as walking. In the present study, the time dependence of loading has been removed to allow for MRI and the problem has been reduced to a single quasi-static observation. Loading rate may play an important role in the formation and development of ulcers (Landsman, et al., 1995), however, high-resolution real-time 3-D MRI is not currently available. All material information extracted from investigation using the device described here will describe the fully relaxed (long time-history) behavior of the tissue.

Other possible uses for this technique include evaluation of changes in foot tissue material properties in pathological conditions and evaluation of the effects of cushioned insoles on internal stresses/strains. Some subjects reported discomfort at the highest loading levels, suggesting that full GRF loading might be dangerous in some of the at-risk target populations, such as patients with peripheral neuropathy whose ability to feel pain is compromised. Fortunately, it

appears that the majority of the soft-tissue deformation occurs at the more tolerable and safe 50% GRF loading (Figure 2.6).

2.6 Acknowledgements

This study was supported by NIH Grant 5R01 HD037433 and the Cleveland Clinic Research Programs Council. Marc Petre was supported by NIH Grant T32 EB04314.

CHAPTER 3

Foot Tissue Material Properties Determined from an MRI Deformation Experiment

Marc Petre, et al., to be submitted to *Journal of Biomechanical Engineering*.

3.1 Abstract

Finite element modeling of the foot has the potential to provide clinically useful information about the currently un-measurable distributions of internal stress and plantar shear. Such predictions require accurate descriptions of foot tissue material behavior, but *in-vivo* mechanical characterization of individual foot tissue layers is scarce in the literature. This investigation bridges this gap by developing a method for the *in-vivo* three-dimensional characterization of individual foot tissue layers.

Load-deformation data were collected using an MRI-compatible foot loading device. A novel, three-dimensional, layered-tissue finite element model of the forefoot was then generated and an inverse finite element material optimization procedure was implemented to match deformations in the foot model to experimentally observed deformations. During the optimization, the deformed locations of model nodes were used to generate predicted 3-dimensional image intensity maps of the deformed foot. Differences between predicted intensity maps and experimental image sets were calculated as a measure of error.

The optimization explored more than 250 different parameter sets and found two sets of first order Ogden material parameters that gave similar optimized errors. The final parameter set was chosen from the two solutions based on the lowest total error and support from previous results in the literature. With these material properties applied, the 3-dimensional finite element model was shown to correctly describe the deformation of skin, fat pad, and muscle under complex loading and is thus well suited for the prediction of internal stresses and/or surface shear distributions under more clinically interesting loading states, such as during gait.

3.2 Introduction

Parametric analyses using finite element (FE) models of the foot have been used to make important contributions to the understanding of interactions between the foot and its environment. For example, FE foot models have been used to investigate the effects of surgical decisions (Budhabhatti, et al., 2007, Cheung, J. T., et al., 2006) and insole geometry, material, and thickness (Erdemir, et al., 2005, Goske, et al., 2006) on plantar pressure distributions. Another desirable application of FE foot models is the prediction of quantities such as the distributions of plantar shear stress and internal stress for which no measurement technique currently exists. Accurate prediction of these quantities would provide valuable insight into the mechanical etiology of neuropathic foot ulcers, a complication estimated to affect 15% of all people with diabetes at some point during their life (Reiber, 2001).

In order to predict the distribution of internal stress, FE models must incorporate realistic geometry, boundary conditions, material properties, and correct constitutive modeling. Unfortunately, realistic descriptions of foot tissue material behavior are difficult to obtain because the *in vivo* characterization of individual tissue layers, such as skin, fat, and muscle, is uncommon. To avoid the need for realistic models of each foot tissue component, many FE models of the foot combine all plantar soft tissues into one lumped material model (Budhabhatti, et al., 2007, Chen, W. P., et al., 2003, Cheung, J. T. and Zhang, 2005, Erdemir, et al., 2005, Goske, et al., 2006, Jacob and Patil, 1999, Lemmon, et al., 1997).

The mechanical properties of these lumped tissues can be well characterized *in vivo* using non-invasive methods such as ultrasound indentation (Erdemir, et al., 2006). Although these models may correctly describe the deformation of the surface of the foot (and be useful for predicting surface pressure), they are unable to distribute internal loads according to the discrete structures of the foot and cannot be used to predict the distribution of internal stresses. A two-dimensional (2D) model of the heel pad including skin and plantar fat layers has been used to predict internal stresses patterns and investigate how they are modulated with footwear intervention (Spears, et al., 2007). 2D models of the forefoot incorporating discrete soft tissue structures have been generated (Actis, et al., 2006) and, in some cases, even used to predict the internal stress distribution of the foot (Gefen, 2003). However, these models

have not incorporated separate skin and plantar fat pad layers and use material models generated from *in vitro* testing of human or animal tissues.

In vitro studies have provided useful information about the mechanics of soft tissues including the plantar fat pad (Ledoux and Blevins, 2007, Miller-Young, et al., 2002), muscle (Bosboom, et al., 2001), skin (Oomens, et al., 2003), and tendon (Zobitz, et al., 2001). However, many of these studies are not directly applicable to the foot and *in-vitro* studies of mechanical properties are limited by questions about the effects of tissue degradation, sample boundary conditions, hydration, and temperature. Any *in-vivo* technique that can provide the same information in a non-invasive, foot-specific manner represents an attractive alternative to *in-vitro* experiments.

In-vivo material characterization requires a test in which tissue deformation is recorded under known loads as well as the means for determining material properties from the data. Several imaging techniques including magnetic resonance imaging (MRI), computed tomography (CT) (Smith, K. E., et al., 2000) and ultrasound (Cavanagh, 1999) have the potential to record in-vivo tissue deformation, but MRI is especially well suited to visualize the deformation of individual tissue layers in three-dimensions (3D) due to its high soft tissue contrast. MRI has been used in the past to determine linear material properties of foot tissues, either through indentation (Gefen, et al., 2001) or elastography (Cheung, Y. Y., et al., 2006, Weaver, et al., 2005), but no studies have characterized the highly non-linear nature of soft tissue or separated bulk response into the contributions of individual layers.

Inverse FE analysis, in which both the load and deformation boundary conditions are known and the material properties are to be determined, may be used in conjunction with image data to determine material properties (e.g. (Actis, et al., 2006, Erdemir, et al., 2006)). This method requires a detailed FE model of the foot containing all of the materials to be investigated. Unfortunately, it is not currently possible for FE models to include all materials of the foot due to restrictions in mesh generation and computational power. For example, proper inclusion of tendons requires not only refined mesh density in the vicinity of the tendons, but also frictionless contact between the tendon and its surrounding tissues.

It is, however, possible to build FE models that include the major tissue layers of interest. For example, the forefoot plantar fat pad plays an important role in distributing the loads of walking and has attracted interest for its possible role in pathological changes associated with diabetes (Bus, et al., 2004). Although interaction of the fat pad with neighboring tissues is more easily implemented in a FE model than the sliding motion of a tendon (since the plantar fat pad is well attached to skin below and muscle above), no such 3D FE foot model with layered tissues currently exists in the literature.

The goal of this investigation was to develop a method for the *in vivo* 3D characterization of subject-specific material properties of foot tissue layers including skin, fat pad, and muscle. This required the creation of a novel 3D FE model of the foot with multiple tissue layers and development of an inverse FE

analysis procedure to minimize the difference between experimental and model predicted deformations.

3.3 Methods

Three-dimensional MRI image sets of the right forefoot of a healthy male subject (21 yrs, 1.68 m, 61 kg) were collected in both the unloaded and loaded states using a previously described MRI-compatible foot-loading device (Petre, M., et al., submitted 2007). The subject signed an informed consent document approved by the Cleveland Clinic Institutional Review Board. The loading device deformed the foot by compressing it between a rigid fiberglass cast at the dorsum and a plastic plate at the plantar surface. Loads were applied to the forefoot by the plastic plate in four increments up to one half of the subject's body weight. Imaging was performed with an OrthOne® one tesla extremity MRI (ONI Medical Systems, Wilmington, MA). The T1-weighted axial image sets had an in-plane resolution of 0.27 mm, an out-of-plane resolution of 2 mm, and took 3.5 minutes to acquire. The posture and loading of the foot was similar to that which would occur during quiet standing on two feet with heels raised. The final data set consisted of 3D MRI image sets collected in the un-deformed condition and with 12.5% (75 N), 25% (150 N), 37.5% (225 N), and 50% (300 N) of the subject's body weight applied (Figure 3.1).

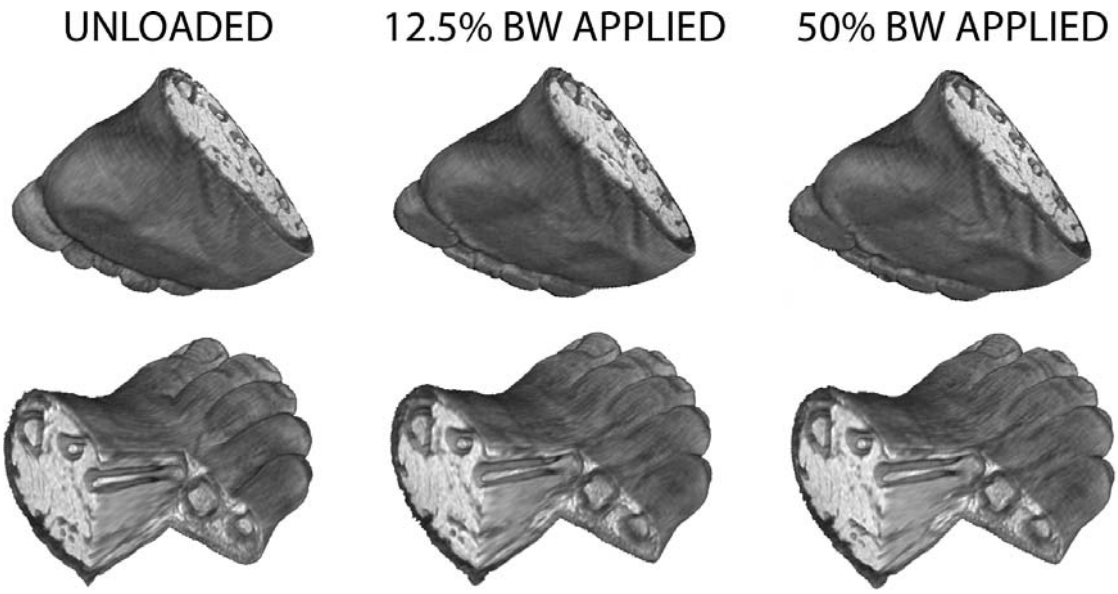

Figure 3.1. TOP: MRI image sets collected in the unloaded state and with 12.5% and 50% of the subject's body weight applied to the forefoot. BOTTOM: The 3D nature of the data allows for visualization and analysis of the tissue deformation along any plane. Note that most of the deformation has already occurred when only one quarter of the total load (12.5% BW) is applied.

A 3D, multi-material, FE model of the subject's forefoot was constructed from the unloaded MRI image set. The shapes of the skin, fat pad, metatarsal, and toe bones were manually extracted from each image in the un-deformed state using custom Matlab® (Mathworks, Inc., Bethesda, MA) segmentation software. 3D surfaces were generated through the collected points using Rhinoceros3D® (McNeel North America, Seattle, WA). All tissue not included in the plantar fat pad, bone, or skin regions was lumped as muscle, the most prevalent remaining constituent. TrueGrid® (XYZ Scientific Applications, Livermore, CA)

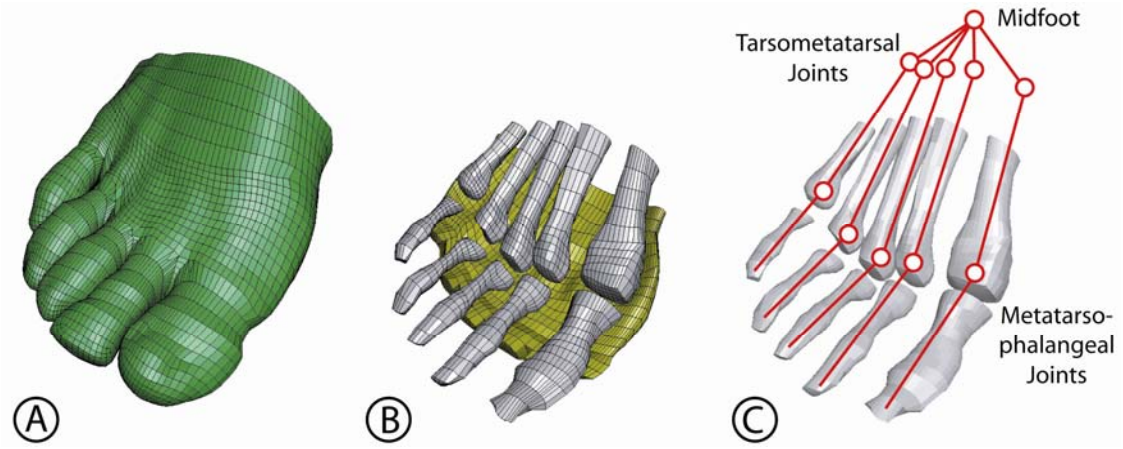

Figure 3.2. (A) The outer surface of the 3D finite element forefoot mesh. (B) The FE mesh with the toes, skin, and muscle removed to display the bones and plantar fat pad. Note that the phalanges of each toe were fused for this study. (C) Joint definitions used to describe model bone kinematics. Open circles represent the locations of joint centers of rotation. The midfoot node was fixed in space throughout simulation of the loading experiment (see Figure 3.3).

was used to generate a 3D hexahedral mesh conforming to the objects of interest (Figure 3.2). Toes were individually meshed, but did not contain tissue layers. They were included to carry load during the simulation and eliminate the need for an assumed boundary condition at the toe-foot interface had they been omitted. The focus of this investigation is the sub-metatarsal head region, a common site of neuropathic ulceration.

The mesh contained 26,324 linear, 8 node elements with a hybrid pressure-displacement formulation that accounted for the nearly incompressible nature of soft tissue by applying a constraint on element volume change (ABAQUS, 2006). The mesh density used for this study was selected based on previous experience

with conceptually similar 3D foot models (Budhabhatti, et al., 2005, 2007). A mesh convergence test was not performed since although increasing the number of nodes would increase the number of data points available for comparison, it would not otherwise affect the optimization process.

To decrease the model degrees of freedom, the phalanges of each toe were fused during simulations. Previous work (Actis, et al., 2006) has suggested that fusion of the interphalangeal joints has little effect on model results. The sesamoid bones were also considered to be fused to the head of the first metatarsal. This assumption is realistic when toe flexion/extension angles, and hence sesamoid motions, are small (Petre, M., et al., 2006). Metatarsophalangeal joints (MTPJ) were defined as connectors with centers of rotation at the approximate centers of the metatarsal heads (Figure 3.2C). Tarsometatarsal joints (TMTJ) had their centers of rotation at the approximate centers of the metatarsal bases. The bases of all metatarsals were attached to a reference point in the midfoot.

The midfoot reference node remained fixed in space throughout the simulation to represent a stationary patient in the MRI. With the foot and lower leg in a passive, relaxed state, the experimental bone pose resulted from a combination of surrounding material compression and passive resistance of ligaments, joint capsules, and other connective tissue. Since these connective structures were not modeled here, the bone pose was prescribed as a known internal boundary condition acting on the tissues. Both plantar/dorsiflexion and ad/abduction (splay) were determined for each metatarsal and fused phalange group at each

load from MRI image sets by overlaying segmented bones in the un-deformed and deformed conditions.

The forefoot mesh was positioned adjacent to, and compressed between, a surface representing the rigid cast and a surface representing the moving, rigid plate to simulate the MRI loading experiment (Figure 3.3) (Petre, M., et al., submitted 2007). The 114.3 mm (4.5") diameter rigid plate was created from design drawings of the MRI loading device. The cast was created by offsetting the dorsal surface of the foot by 1 mm and applying a smoothing algorithm in Rhino3D to mimic the lightly padded fiberglass cast used in the experiment. The

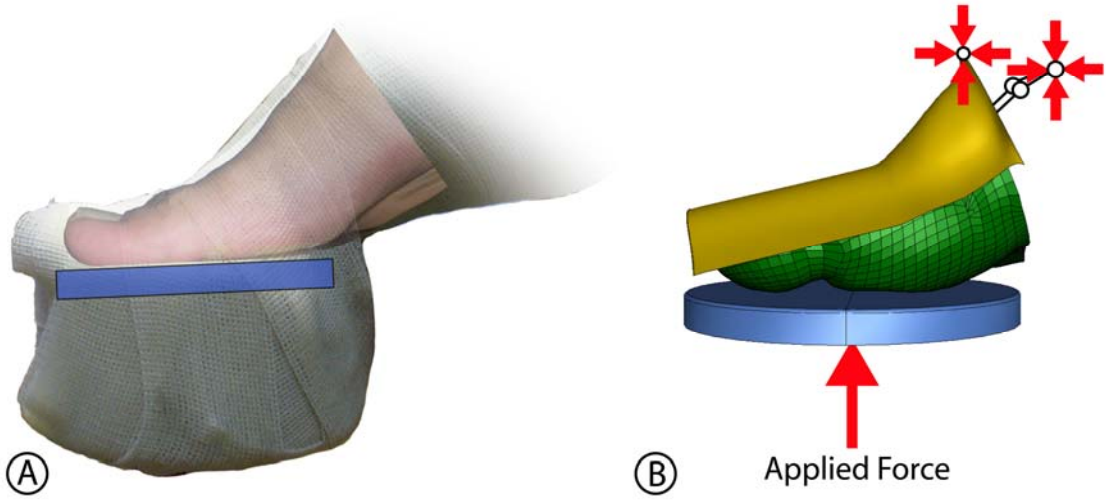

Figure 3.3. (A) The foot-loading device used during collection of MRI deformation data. For a more thorough description, see Petre et al. (submitted 2007). (B) FE simulation of the MRI loading experiment incorporating the 3D, layered tissue FE mesh. The midfoot and cast were fixed during the simulation and forces were applied to the rigid plate, as in the MRI experiment.

cast toe box was flattened to simulate the stretching of cast material across the top of the loading device. Contact between the foot and the cast was assumed to be frictionless to simulate the effect of an elastic stockinette sleeve and contact between the foot and the plate, where the stockinette was cut away, was given a static coefficient of friction μ = 0.5. During the simulation, the rigid plate was pressed against the bottom of the foot in four loading increments, equal to those used in the MRI deformation experiment, up to 300 N (one half body weight). Foot motion was restricted by the rigid cast at the dorsum and, through bone kinematics, by the fixed midfoot. Nodes on the proximal surface of the foot, where the model was sectioned from the rest of the foot, were not constrained.

All bones were considered rigid based on their high stiffness relative to soft tissues. Actis et al. (2006) have shown that above a stiffness of 7,300 MPa the material properties of bone contribute very little to foot model behavior. The nonlinear, finite strain behavior of lumped toe soft tissue, skin, fat pad, and muscle were described as first order Ogden hyperelastic materials (Ogden, 1984). The Ogden material model describes the strain energy potential, *W*, in terms of powers of the principal deviatoric material stretches (λ_i = 1 + ε_i, where ε_i is the principal deviatoric strain from the left Cauchy-Green strain tensor):

$$W = \frac{\mu}{\alpha^2}\left(\lambda_1^{\alpha} + \lambda_2^{\alpha} + \lambda_3^{\alpha} - 3\right) + \frac{1}{D}\left(J - 1\right)^2 \qquad \textbf{Equation 3.1}$$

where *J* is the volume ratio and μ (in units of stress), α (unitless), and *D* (units of 1/stress) are parameters used to tune the model to describe particular materials. Stresses are obtained by taking partial derivatives of the strain energy potential

with respect to deformation (e.g. $\sigma_1 = \partial W/\partial\lambda_1$). Material parameters are purely phenomenological in nature, but do carry some physical meaning with the μ parameter controlling initial material stiffness, α controlling the strain hardening behavior, and *D* controlling material compressibility. *D* is related to the Poisson's ratio, ν, through the shear modulus at the start of deformation (initial shear modulus), μ_0 (Equation 3.2).

$$D = \frac{2\mu_0(1+\nu)}{3(1-2\nu)} \qquad \textbf{Equation 3.2}$$

The Ogden material model satisfies the principle of objectivity and, for modeling simplicity, assumes material isotropy which has been recently demonstrated for the heel pad (Miller-Young, et al., 2002), but is unlikely for muscle and skin.

An inverse finite element optimization technique was used to determine the most appropriate material parameters to describe the subject's forefoot skin, fat pad, and muscle (Figure 3.4). Material compressibility was fixed during the optimization with *D* = 6.993 ($\nu \cong 0.475$) to represent the nearly incompressible nature of the soft tissue. Three materials with two Ogden material parameters each led to a set of six parameters to be optimized: μ_{skin}, α_{skin}, μ_{fatpad}, α_{fatpad}, μ_{muscle}, α_{muscle}. The inverse finite element technique began by running the FE simulation with an initial guess at material parameters. It was then necessary to quantify the error between model predicted deformation and the experimental deformation using output from the FE model and the experimental MRI image sets.

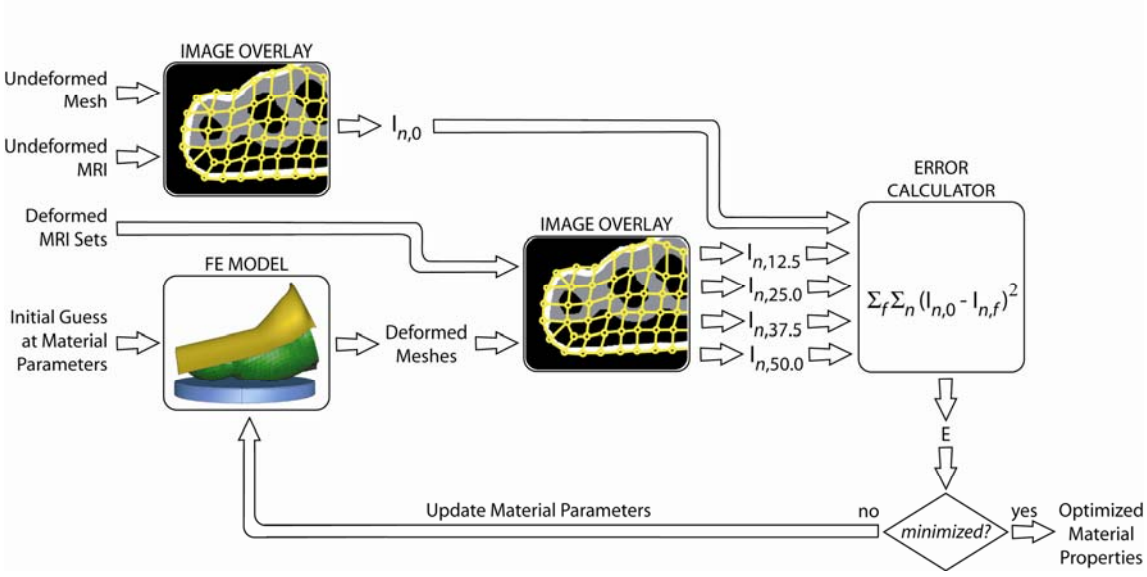

Figure 3.4. The inverse finite element technique used to determine material parameters. Inputs to the technique (at the left) are deformed and un-deformed MRI image sets, an un-deformed FE mesh, and an initial guess at material parameters. The mesh overlay process, used to determine the pixel value at each node, is further described in Figure 3.5. The error calculator and its inputs are described in the text surrounding Equation 3.3. Briefly, each vector, $I_{n,f}$ contains the corresponding image intensities for each of the *n* nodes at loading level *f*. Error is calculated by comparing predicted intensities at each of the loading levels to the intensities in the unloaded state, $I_{n,0}$.

Each node of the finite element mesh represented a material point in the foot. This material point maintained its gray scale value derived from the magnetic resonance response under deformation such that the pixel intensity at each material point remained the same between the un-deformed and deformed conditions. If the FE model correctly described the material deformation, then

the node correctly tracked its material point and the deformed image intensity at the deformed node location matched the original image intensity at the un-deformed node location. For example, a node that corresponded to a black cortical bone pixel in the un-deformed state should also correspond to a black pixel in the deformed state.

Based on this information, the nodes of the FE model were assigned pixel intensity values from the un-deformed MRI image set (Figure 3.5). As the model deformed during simulation of the experiment, the nodes carried their assigned image intensity with them, distorting the relative locations of their assigned pixel values. The new pixel intensity field created by the deformation represented a model predicted deformed image set which could be compared to the experimentally measured deformed image set.

The appropriateness of each material parameter set was quantified by calculating the objective function, defined as the total error between the intensity maps of model predicted and experimental image sets (Equation 3.3).

$$E = \sum_{f=1}^{4} \sum_{n=1}^{m} (I_{n,0} - I_{n,f})^2 \qquad \textbf{Equation 3.3}$$

E is the square error between model predicted and experimental deformation, $I_{n,0}$ is the un-deformed image intensity at node *n* with zero load applied (un-deformed condition) and $I_{n,f}$ is the intensity at node *n*'s deformed coordinates in the image set with load *f* applied. The total error was a summation of errors at each of the four simulated experimental loads ($f \in$ [12.5%, 25%, 37.5%, 50% body weight]). The inclusion of intermediate loads, rather than just the maximal

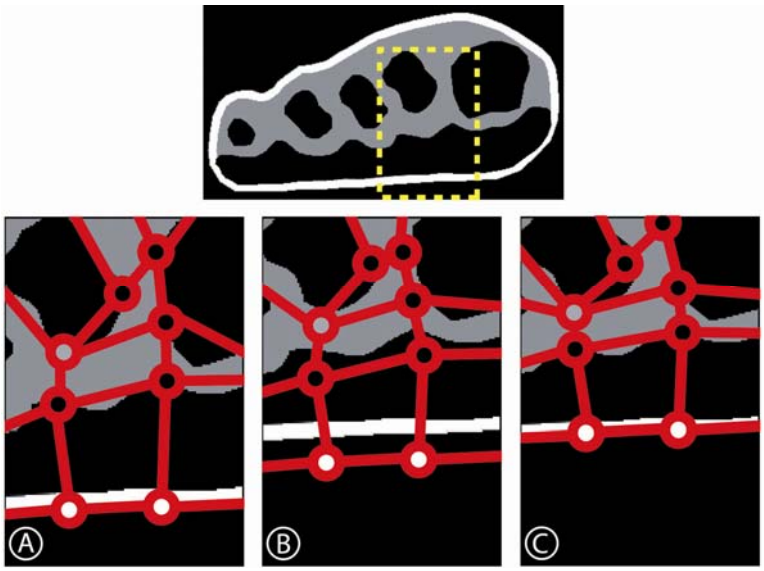

Figure 3.5. A schematic description of the mesh overlay process in the region of interest shown at the top. (A) Each node of the un-deformed FE mesh is assigned a pixel intensity value corresponding to its location in the un-deformed MRI image set. This pixel value is fixed to the node as it undergoes deformation during simulation of the experiment. The deformed mesh can be used to generate a (relatively coarse) model predicted deformed image that can be compared to the experimental MRI images on a node by node basis. (B) If the current material parameters are, for example, stiffer than the real material, then the mesh will not deform as much as the tissue and the node intensity values will fail to correlate with the deformed MRI image set. (C) If the material properties governing node motion correctly match the tissue, then the deformed mesh will correlate well with the deformed image set. The process illustrated here in 2D with 8 nodes was actually applied in 3D allowing for out-of-plane deformations of more than 17,000 nodes induced by nearly incompressible materials.

load, allowed for better determination of the non-linear history of the deformation. No toe nodes were considered in the optimization, but all other nodes ($m \cong$ 17,450 nodes) were included in error calculations. Nodes were temporarily excluded from the error calculations if their coordinates fell outside of the imaged region. This occurred at the proximal cut surface of the model were the soft tissue bulged beyond the plane of the most proximal MRI image and resulted in transient exclusion of up to 250 nodes (1.4% of all nodes) from this area of low interest.Material parameters were updated using a custom gradient-based optimization algorithm. After determining the value of the objective function at the current material parameter set, numerical gradients in parameter space were calculated for each of the six material parameters (requiring an additional 6 FE solutions). The optimization then took controlled steps along the gradient in the direction of steepest descent using a golden section based line search (Belegundu and Chandrupatla, 1999). If the optimization reached an apparent minimum, the near-region of the solution was explored by minimizing the parameters one at a time (rather than simultaneously).

The initial material parameters were adapted from data collected on *in-vivo* ultrasound indention of 80 human heels (40 diabetic, 40 non-diabetic) (Erdemir, et al., 2006). Although these data were from testing of bulk material properties, it is expected that the discrete materials investigated here are likely to have similar values. The unconstrained optimization was started from the "stiff" (μ = 19.04 kPa, α = 10.92), mean (μ = 14.3 kPa, α = 7.3), and "soft" (μ = 5.3 kPa, α = 7.48) observed heel pad behavior to assure that the final solution was a global mini-

mum rather than a local minimum. The “soft”, and “stiff” parameter sets were chosen based on overall evaluation of the stress/strain behavior of all heel pad specimens. At each starting point, the same material properties were given to all three optimized materials. Lumped toe tissue was not optimized and had fixed properties of the mean lumped heel pad behavior (μ = 14.3 kPa, α = 7.3).

Although the objects of interest (fat pad, skin, bone, and muscle) were clearly visible in the original T1 weighted MRI images, there was considerable variation in image intensity within objects and, particularly in the plantar fat pad, not always enough contrast with surrounding objects (Figure 3.6A). This resulted in low sensitivity of the objective function to changes in material parameters. Median filtering of the images removed some of the excessive fine detail, but the boundaries of the fat pad were further obscured. The solution used here was to perform the optimization using images re-colored based on object boundaries (Figure 3.6B). Boundaries for re-coloring were generated using the segmenta-

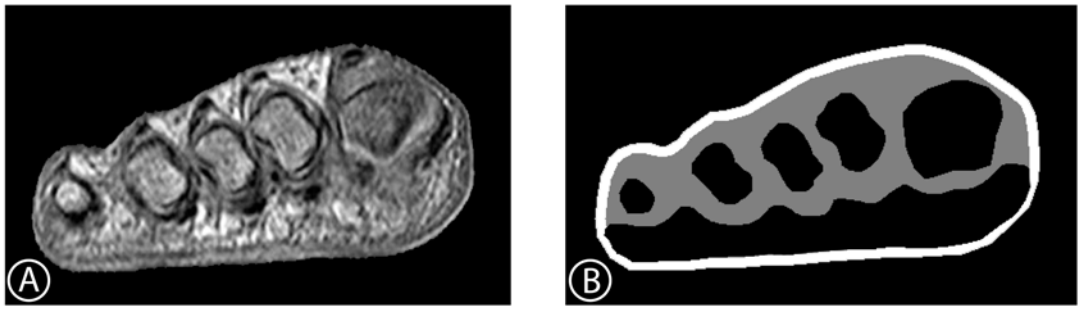

Figure 3.6. An example slice from the un-deformed MRI image set before (A) and after (B) re-coloring to increase the sensitivity of the objective function to changes in material parameters.

tion curves that were used for finite element mesh generation. The re-colored image sets provided high-contrast between objects of interest, uniformity within objects of interest, and, as a result, greatly enhanced objective function sensitivity.

3.4 Results

During the optimization process, more than 250 finite element solutions with different material properties were obtained. The average model solution time was five hours on a computer with two, dual-core, Xeon® processors running 64-bit Red Hat Enterprise Linux with 6 GB of RAM. Relatively small improvements in error from different starting points to the optimized points implied that the starting points represented good initial guesses. Non-zero final errors implied that there were systematic modeling errors that could not be resolved by changing the material parameters. In general, the optimization was more sensitive to α parameters than to μ parameters.

The optimization started from the soft bulk heel pad properties began in an area of diminished convergence characteristics caused by excessive strains in the soft tissue. Small changes in material parameters around this point often resulted in simulations that would not reach to a final solution. Even with perturbation of individual parameters, the optimization failed to progress far from the starting point and only decreased the error function by about 3%. Although exploration of the parameter space at the lower end of the stiffness spectrum was less hindered by model convergence issues, this region was not expected to

yield the best parameter set due to low model stability and relatively large errors in predicting the experimental data.

The optimization that was started at the stiff heel pad parameter set was able to decrease the error function from 4.31x 10^8 to 3.62 x 10^8 (16% improvement) and found a solution of μ_{skin} = 13.1 kPa, α_{skin} = 22.02, μ_{fatpad} = 11.5 kPa, α_{fatpad} = 15.45, μ_{muscle} = 62.7 kPa, and α_{muscle} = 31.52. The optimization that was started at the mean heel pad properties decreased the total error from 4.63 x 10^8 to 3.59 x 10^8 (22% improvement) and returned what is believed to be the global minimum at μ_{skin} = 232.5 kPa, α_{skin} = 21.64, μ_{fatpad} = 0.73 kPa, α_{fatpad} = 17.97, μ_{muscle} = 167.6 kPa, and α_{muscle} = 25.65. Given the wide variation between parameters and small variation between final errors, both of these solutions were further analyzed.

Visually, the model forefoot deformation matched the experimental forefoot deformation well with both sets of optimized parameters applied. However, comparison of the predicted compressive stress-strain behavior of the two solutions illustrated significant differences in material behavior between the two parameter sets (Figure 3.7). There were only minor differences between the two predictions of muscle compressive behavior, however, the skin and plantar fat pad behaviors displayed distinct differences between parameter sets. When the optimization was started from the firm material parameters, the end result predicted a relatively soft skin and a firm plantar fat. When the optimization was started from the mean parameter set, the skin was predicted to be relatively firm and the plantar fat as relatively soft.

Model-predicted stresses within the muscle were similar for both parameter sets (Figure 3.8). However, as expected from the predicted compressive stress-strain behavior, there were significant differences in the distributions of stress in the fat pad and plantar skin region. Specifically, the softer skin (Figure 3.8, right panels) developed more hydrostatic pressure and less deviatoric stress under the same loading.

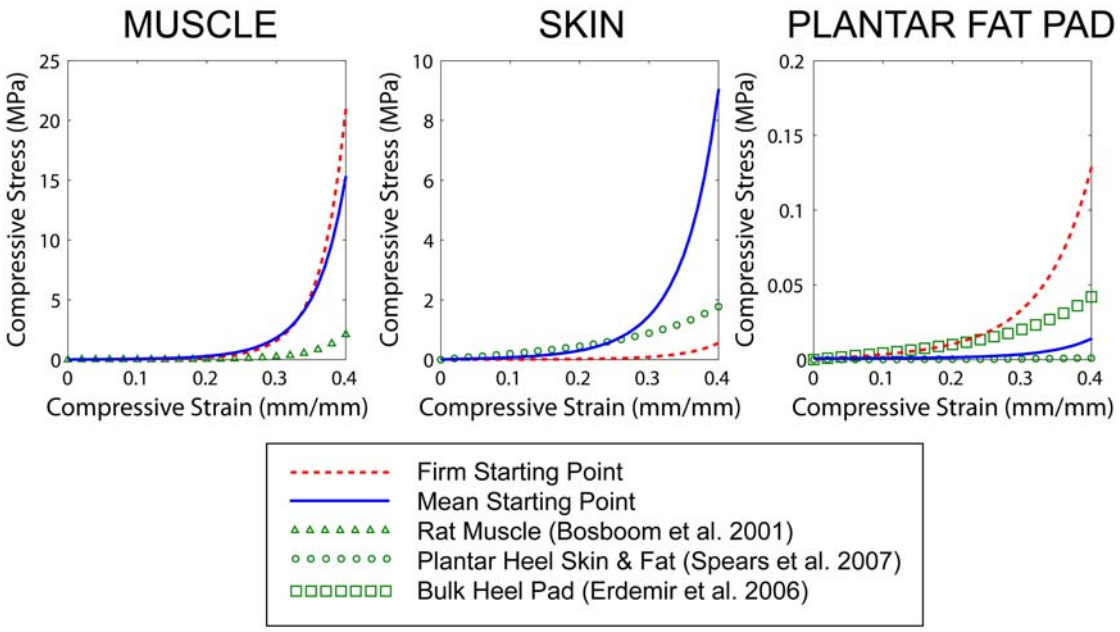

Figure 3.7. Predicted compressive stress-strain diagrams for the optimized materials at the solutions reached from the firm and mean starting points. Predicted data from the literature is also shown for muscle, skin, bulk heel pad, and plantar heel fat pad.

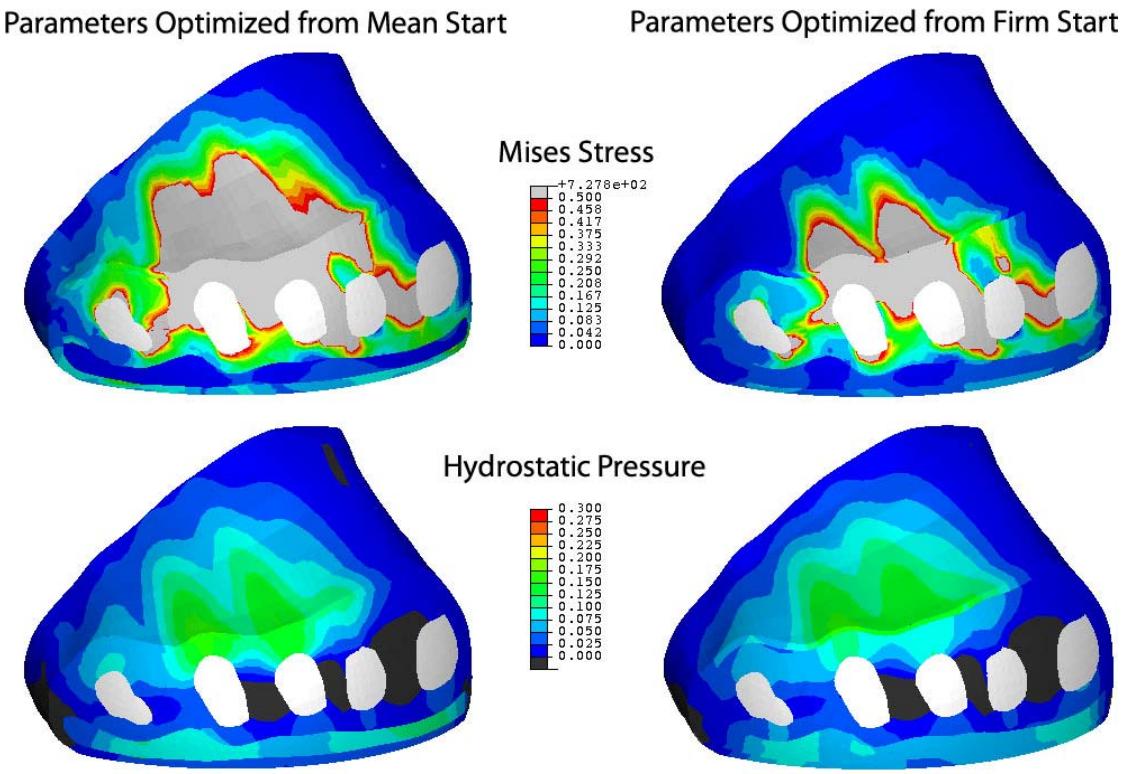

Figure 3.8. The forefoot model has been sectioned at the approximate level of the metatarsal heads to show the predicted distribution of internal stresses. von Mises stress (top), and hydrostatic pressure (bottom) are shown using the material parameters obtained from the mean starting point (left) and the stiff starting point (right). Large stresses are present at the dorsum in both cases as the foot is being compressed passively against a rigid dorsal cast as in the MRI load-deformation experiment.

3.5 Discussion and Conclusions

The existence of two solutions with similar degrees of fit, but dissimilar predicted behavior implies that the same experimental strains may be achieved using very different material parameters through interactions between material layers. Significant differences in internal stress distributions in the plantar aspect of the forefoot emphasize the importance of choosing the appropriate material parameters (Figure 3.8). Fortunately, selection between the two solutions was simplified by the fact that the parameter set with lower total error (from the optimization started at mean parameters) was also in better agreement with modeling expectations and previous results from the literature.

Both parameter sets predicted muscle behavior that is stiffer than previously reported values based on in-vivo compression testing of rat tibialis anterior (Bosboom, et al., 2001). This may be due to the fact that the material referred to as muscle in this study is a combination of all materials not identified as skin, plantar fat pad, or bone. This includes dorsal subcutaneous fat, fascia, and relatively stiff joint capsules, and ligaments.

Both parameter sets also predict skin behavior that is stiffer than previously reported values extracted from compression testing of pig back skin (Figure 3.7) (Oomens, et al., 2003). Differences could be due to variations in skin content in different regions of the body, specifically, stratum corneum has a modulus on the order of 100 MPa (Yuan and Verma, 2006) and this layer is significantly thickened on the plantar surface of the foot. Optimized parameters from a study of plantar heel skin matched the current data well up to strains of about 0.25

(Figure 3.7) (Spears, et al., 2007). Data used to generate these heel skin parameters may not have included high enough strains to predict the sharp strain hardening reported in this study.

The results of previous bulk testing of human plantar heel tissue are shown along with the current predicted behaviors in Figure 3.7 (Erdemir, et al., 2006). It is expected that this bulk behavior is the sum of a soft fat and a firm skin contribution and, therefore, it is encouraging that the preferred parameter set predicts slightly softer compressive behavior than the bulk. This prediction is also in better agreement with *in vitro* studies of isolated heel (Miller-Young, et al., 2002) and forefoot plantar fat (Ledoux and Blevins, 2007).

It should be noted that the optimization protocol used here explored the parameter regions suggested by other studies and found that, for the current subject, they were less suitable (higher total error) than the optimized parameter set. It should also be noted that the majority of previous testing was uni-axial in nature while the current parameters take into account test information from a variety of deformation modes as the compression of the foot induces tension in the skin, shearing at the bulging edges, and compression in the center. This may lead to differences in the material parameters that should reflect an improved ability to predict complex loading states.

The existence of local minima (encountered when optimizing from the firm and soft heel pad properties) is not unexpected. In addition to summing errors at different loading levels, the net error in image intensities represents a summation of (1) errors in the model's prediction of various deformation modes (2) errors in

the model's prediction of different materials. There may not be one set of Ogden material parameters that is optimal for describing all deformation modes (see (Petre, M. T., et al., 2006) for an example of this phenomenon). If this is the case, then local minima could represent parameter sets better suited for describing certain types of deformations (e.g. compression) than others (e.g. shear). In certain cases, it may be possible for the general behavior of the forefoot to be dominated by one material. For example, when optimizing from the stiffest heel pad properties, the skin took on very stiff material properties that may have influenced load transmission to the interior tissues. This high stiffness may have resulted in decreased error in the node regions associated with skin, but increased in error in the regions associated with fat pad and muscle. This investigation attempted to deal with these known issues and find the global minimum by starting the gradient based optimization from a variety of parameter sets and thoroughly exploring the parameter space (>250 different parameter sets evaluated).

The RMS error diminished during optimization, but did not approach zero. Differences between model predicted deformation and the experimental deformation may come from two sources: improper material parameters and errors in modeling assumptions. The optimization attempts to find the best material properties, given the likely existence of systematic errors in modeling assumptions which prevent the error from vanishing. These modeling errors may include (1) simplification of geometry (2) lumping of tissues and (3) inadequacy of the chosen material model.

The Ogden material model has been shown to fit soft tissue mechanical behavior well (i.e. low RMS error) and with relatively good efficiency (i.e. only two parameters). It has been reported to be more accurate than competing models in fitting experimental results when data from multiple deformation modes are available (Wu, et al., 2003). One disadvantage to the Ogden model is that it cannot be expanded to include material anisotropy, which is likely to be important for skin and muscle. Other material models may be able to fit the MRI deformation data equally well and/or with the inclusion of material anisotropy. This area requires further investigation.

The technique described in this investigation is unlike other inverse FE analyses in that the experimental strains are not known for comparison with the model predictions. Instead, matching of experimental strains is implied by agreement between model predicted and experimental image sets. This method eliminates the need to track strains in three dimensions but requires a good initial guess to be effective. An alternative technique would be to use hyperelastic non-rigid image registration to calculate experimental strains from the MRI image data (e.g. (Veress, et al., 2005)). Although hyperelastic registration is a promising method of tracking 3D strains in MRI foot images, software to perform this type of analysis is not currently available commercially or otherwise.

Subject-specific material properties were successfully determined from *in-vivo* MRI load-deformation data. Using data of this type has several distinct advantages for material parameter determination. First, the testing is truly *in-vivo* and is not subject to any questions of tissue hydration, temperature, viability,

sample edge boundary conditions, or animal model extrapolation to humans. Second, the ability to examine individual tissue layers in 3 dimensions with intact connections to neighboring layers is maintained. Third, although only a compressive load was applied, the irregular, non-linear geometry resulted in a combination of compressive, tensile, shear, and volumetric strains in the tissue. As a result, parameter determination included information about material response to a variety of deformation modes likely to be encountered during gait simulations. For a similar Ogden-based, elastomeric foam material model, the inclusion of multi-axial test data during parameter determination was shown to be important for predicting deformations in complex loading simulations (Petre, M. T., et al., 2006).

The inclusion of skin, fat, and muscle tissue layers in a 3D finite element foot model represents a significant increase in complexity over the current state of the art. The model used in this investigation explored the current limits of the ABAQUS® Standard FE solver by including non-linear geometry, non-linear materials, confined compression of nearly-incompressible tissue, and contact with friction. As computational power increases and FE solver efficiency and capabilities expand, it will be possible to increase the complexity of the model by including cartilage, tendons, ligaments, joint capsules, and/or any other structure of interest that is visible in the high-resolution image sets (see Figure 3.6A).

Completion of the over 250 simulations required for the optimization consumed almost 3 weeks of wall-clock time on a well-equipped personal computer. Although this process resulted in only one set of material parameters, these

parameters significantly increase the predictive power of the 3D finite element forefoot model. The model may now be used with increased confidence to predict clinically interesting, and previously inaccessible, quantities such as plantar shear and internal stress distributions during gait.

3.6 Acknowledgements

This study was supported by NIH Grant # 5R01 HD037433, the Cleveland Clinic Research Programs Council, and Marc Petre was supported by NIH Grant # T32 AR50959. The advice of Vassilis Panoskaltsis, PhD is gratefully acknowledged.

CHAPTER 4

Investigating the Relationship between Plantar Pressure and Internal Stress

Marc Petre, et al., to be submitted to *Journal of Biomechanics*.

4.1 Abstract

This article describes the use of two and three-dimensional finite element models of the forefoot to investigate the relationship between plantar contact pressure and measures of the internal stress or strain states in the plantar skin and fat pad regions of the forefoot. The effect of reducing plantar contact pressure on internal variables was also investigated by simulating the same motion both barefoot and on a pressure relieving foam mat.

Bones acted as stress risers, concentrating von Mises stresses at the top of the plantar fat pad beneath the 3rd metatarsal head. The fat pad acted as a distributor of this load, decreasing its magnitude by a factor of ten and spreading it over a larger region of the plantar skin, probably through conversion of the focal stresses to more distributed hydrostatic pressure. von Mises stresses at the skin surface were localized under the 2nd metatarsal head and correlated well with the location of peak plantar pressure. Insertion of a soft foam mat between the foot and floor resulted in a 66% decrease in peak plantar pressure but only a 2% decrease in peak internal stresses at the dorsal surface of the fat pad. Although

fat pad stresses remained high, skin von Mises stresses in the region around the peak plantar pressure were significantly reduced (78.5% decrease).

Although this study is a limited modeling investigation of only one foot, the results provide, for the first time, insight into stress distribution in the plantar tissues using a model where the properties of the tissues are well characterized. The findings imply that the location of high magnitude deep tissue stresses may not be identical to the location of peak plantar pressure. A soft, thick foam mat was able to reduce both surface and internal skin stresses. The implications of this information for the genesis of plantar ulceration in diabetic patients and the development of therapeutic footwear should be further investigated by solving the model with other interventions that reduce plantar pressure such as total contact insoles, midsole plugs, and metatarsal pads.

4.2 Introduction

Diseases that result in the loss of protective sensation in the lower extremities place patients at high risk for foot complications including neuropathic ulceration. If foot ulcers remain unnoticed or untreated, damage may progress or the wound may become infected. The persistence of complicated wounds is a major cause of foot amputation with 84% of all amputations in patients with diabetes preceded by an ulcer (Pecoraro, et al., 1990). Diabetes increases the risk of foot amputation by a factor of ten (ADA, 2002) and foot ulceration and amputation have been shown to significantly decrease the quality of life (Ribu, et al., 2007) and to increase healthcare costs (Matricali, et al., 2006).

Ulcer formation is dependent on a variety of factors including control of blood sugar, vascular status, motor, sensory, and autonomic nervous function, patient compliance, activity level, and mechanical loading (Dinh and Veves, 2005, Reiber, 2001). The last of these, mechanical loading, represents an accessible target for effective, non-invasive intervention. For this reason, clinicians would like to be able to identify subjects at high risk due to mechanical loading and provide them with interventions that reduce that risk, such as therapeutic footwear.

Although many experts believe that ulcers begin internally and progress to the skin surface through repetitive loading (Brand, 1978, Delbridge, et al., 1985, IWGDF, 2005), there is currently no way to clinically assess the internal stress-strain state of the foot. As a result, foot risk due to mechanical loading is currently evaluated by measuring the distribution of forces acting on the plantar surface of the foot (Armstrong, et al., 1998, Bus and de Lange, 2005, Perry, et al., 2002). The most common tool, plantar pressure measurement, assesses the vertical component of applied force and is only roughly 65% specific and 70% sensitive for foot ulceration (Armstrong, et al., 1998).

Plantar pressure measurements have been used to evaluate footwear interventions (Mueller, et al., 2006), hosiery (Garrow, et al., 2005), and ulcer healing strategies (Petre, M., et al., 2005) based on the assumption that redistributing foot forces to reduce the peak plantar pressure will improve outcomes. This approach represents the current best practice for treatment, but studies designed to show the efficacy of pressure lowering footwear interventions have

been equivocal at best (Maciejewski, et al., 2004). Some feet remain difficult to keep ulcer free, and some feet with high plantar pressures never ulcerate.

Assessment and treatment strategies may be improved by gaining a better understanding of how the clinical goal of lowering peak surface pressure relates to the reduction of potentially damaging internal stress and strain. For example, numerical modeling of the buttocks – another site at risk for ulceration - suggested that the relationship between contact stress and internal stress is not straight-forward and that interface pressures alone are not sufficient to evaluate the benefits of a supporting surface (Oomens, et al., 2003). Many 2-dimensional (2D) (Actis, et al., 2006, Gefen, 2003, Goske, et al., 2006, Lemmon, et al., 1997, Spears, et al., 2007, Yarnitzky, et al., 2006) and 3-dimensional (3D) (Budhabhatti, et al., 2005, Budhabhatti, et al., 2007, Chen, W. P., et al., 2001, Cheung, J. T., et al., 2005, Petre, M., et al., submitted 2007) finite element (FE) models of the full or partial foot exist, but these models have generally been developed to predict contact pressures using lumped plantar soft tissue properties.

In order to correctly predict the distribution of loading and strain across the different tissues of the foot, models designed to predict internal stress must avoid combining skin, fat, and other layers into one lumped tissue model in the area to be investigated. For example, Spears et al. (2007) found that a 2D frontal plane heel pad model with separate skin and fat layers was better suited for plantar pressure prediction than a model with lumped tissue. Gefen (2003) constructed 2D sagittal plane FE models of the human foot to investigate the internal stress distribution. His models incorporated plantar fat pad, ligaments, and plantar

fascia and predicted elevated internal stresses suggesting that ulceration may be initiated beneath the skin surface. Chen used a 2D model of the heel incorporating multiple skin and fat layers to show that stresses at the skin/fat interface are greatly affected by skin stiffness and applied shear stress (Chen, Y., 2003). Unfortunately, these 2D models are unable to provide information about the importance of out-of-plane stresses and/or deformations that occur due to the nearly incompressible nature of soft tissue. Extending the models from 2 to 3 dimensions adds complexity in terms of finite element mesh generation. To our knowledge, our previous work represents the only 3D layered tissue finite element model of the foot currently in the literature (Petre, M., et al., submitted 2007).

FE models predicting internal stress must also use realistic descriptions of material behavior. Ideally, tissue components would be individually characterized *in-vivo*, preferably in the subject being modeled. However, such characterization of the foot tissues is limited and only recently have the material properties of different foot tissue layers been characterized in live subjects (Petre, M., et al., submitted 2007, Spears, et al., 2007).

This article investigates the relationship between contact pressure and internal stress and strain using 2D and 3D FE forefoot models incorporating subject-specific layered tissue geometry, material properties, and loading. It focuses on the instant of foot contact during gait when peak pressures reach a maximum in a common site of neuropathic ulceration - the metatarsal head region of the forefoot. In addition to simulating barefoot contact, contact with a

cushioning insole material inserted under the foot is also considered to examine how the clinical goal of lowering peak contact pressure affects internal stress and strain.

4.3 Methods

This study was performed using a previously described subject-specific FE model of the right forefoot of a healthy male subject (21 yrs, 1.68 m, 61 kg) (Petre, M., et al., submitted 2007). The finite element mesh was refined from 26,000 linear hexahedral elements, as previously described, to 40,000 elements with the intention of better predicting the distribution of internal variables. There is currently no information in the literature about the maximum allowable element size for internal stress prediction. The 3D model contained separate sections representing skin, plantar fat pad, muscle, metatarsal bones, fused phalange bones, and lumped toe soft tissue. In the sub-metatarsal head region of the mesh, element size was approximately 1.8 mm on a side. All bones were considered rigid (no deformation allowed) and all other materials were given isotropic, first order Ogden hyperelastic material properties (Table 4.1)(Ogden, 1984). All toe soft tissue was lumped into one material model assumed to have the mean lumped tissue behavior determined from in-vivo indentation testing of the plantar heel tissue from 80 feet (Erdemir, et al., 2006). The Ogden parameters for all other materials were determined using an inverse finite element analysis technique that matched model deformations to those observed in an in-vivo MRI load-deformation experiment of the same subject (Petre, M., et al., submitted 2007).

Table 4.1. First order Ogden hyperelastic material properties given to the model tissues. Properties for skin, plantar fat pad, and muscle were determined from an *in vivo* MRI loading experiment. Lumped toe soft tissue properties were determined from *in vivo* ultrasound indentation of 80 heels. A value of 6.993 for D corresponds to a nearly-incompressible Poisson's ratio of 4.75.

Material	μ (kPa)	α	D
skin	232.5	21.64	6.993
plantar fat pad	0.73	17.97	6.993
muscle	167.6	25.65	6.993
lumped toe soft tissue	14.3	7.3	6.993

Metatarsophalangeal joint motion was described using connectors with one rotational degree of freedom allowing each set of fused phalanges to dorsi/plantarflex about the approximate center of its corresponding metatarsal head (Figure 4.1A). Tarsometatarsal joints were also given one rotational degree of freedom, allowing each metatarsal to dorsi/plantarflex about the approximate center of its base. The bases of all metatarsals were connected to a single point representing the midfoot. Joint capsules, tendons, and cartilage were not modeled.

The subject's three-dimensional walking ground reaction force (GRF) and plantar pressure distribution were simultaneously recorded using an EMED-X® pressure measurement system (Novel, Inc., Minneapolis, MN) mounted on top of a force plate (Kistler, Amherst, NY). A first-step protocol, commonly used in diabetic foot clinics was applied (Bus and de Lange, 2005). Pressure distribu-

tions were collected at 100 Hz with a spatial resolution of 4 sensors/cm^2 and force measurements were collected at 1000 Hz. The 3D ground reaction force was extracted at the instant of peak metatarsal head (MTH) pressure. The instant of peak MTH pressure, rather than peak forefoot force, was chosen for quasi-static modeling because it represents the instant in time with the highest concentration of force over a small area of tissue. The extracted GRF (485 N vertical, 13 N anterior/posterior, and 11 N medial/lateral) was applied to the midfoot of the model, pressing the forefoot against a rigid plate (Figure 4.1A).

The model predicted plantar contact pressure distributions are known to be

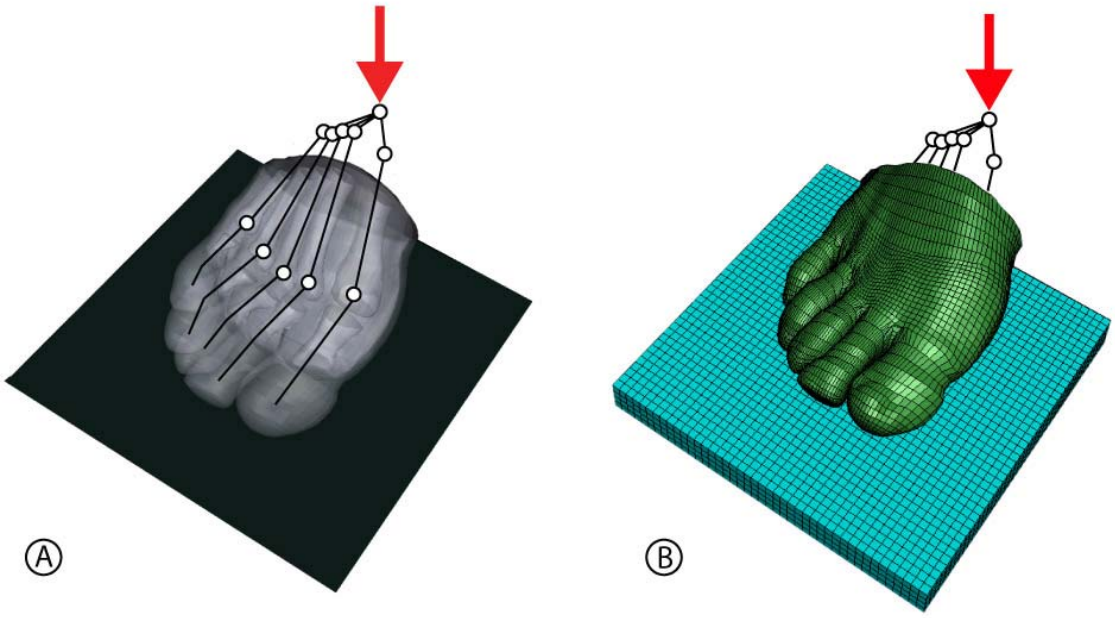

Figure 4.1. (A) The barefoot, forefoot finite element model showing joint locations and midfoot application of the measured GRF. (B) The FE model with a 12.7 mm thick foam mat inserted between the forefoot and the rigid ground to reduce the peak plantar contact pressure.

sensitive to both foot alignment to the floor and internal bone configuration (Budhabhatti, et al., 2005). For example, if the second metatarsal head is plantarflexed with the applied GRF held constant, the plantar contact pressure beneath the second metatarsal head will increase and contact pressures in other areas of the forefoot will decrease. The internal stress or strain distributions are expected to be similarly sensitive to changes in bone configuration, so it was important for this study that model bone configuration matched the subject's bone configuration at the simulated instant of gait.

The forefoot mesh was generated from MRI images collected with the foot in a relaxed position. The configuration of the bones in this state was expected to be different than the configuration of the bones at the instant of peak forefoot pressure due to the combined action of the applied GRF, passive tissues (ligaments, joint capsules, fascia), and active tissues (intrinsic and extrinsic muscles). In the absence of a complex model that can accurately describe the actions of all of these effectors, the bone configuration at the instant of peak metatarsal head pressure was determined using a bone configuration optimization technique (Budhabhatti, et al., 2007). With the applied midfoot load held constant, 10 degrees of freedom (plantar/dorsiflexion of 5 metatarsals and 5 toes) were iteratively adjusted until the difference between model predicted and experimental peak plantar pressures was minimized. Peak pressures were compared in 10 masked regions of interest representing the 5 metatarsal heads and 5 toes (Figure 4.2). The procedure produced a set of optimal joint angles and, as a by-product, the joint moments required to maintain those angles.

During the bone configuration optimization procedure, the interaction between the foot and plate was assumed to be frictionless to decrease solution time and thus only the vertical component of the subject's GRF was applied. For the

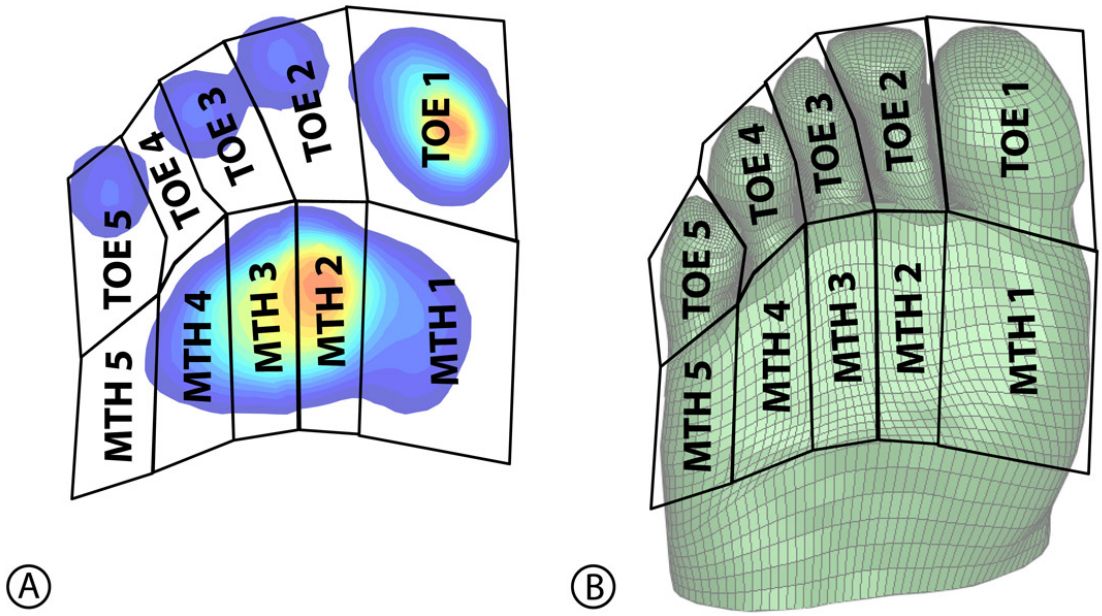

Figure 4.2. Masked regions used for optimization of bone configuration. (A) Masked experimental data at the instant of peak plantar metatarsal head pressure (B) Masked model surface node sets.

final simulation in the optimized configuration, penalty contact with a static coefficient of friction of 0.5 was defined between the foot and the floor and both vertical and horizontal loading were applied.

As the mechanism of soft tissue damage associated with ulceration is not known, it is difficult to select one internal stress or strain variable as the sole indicator of risk. For example, the extracellular matrix could be damaged by excessive distortional stress. Cells themselves may also be damaged by exces-

sive distortional stress, but they may have the additional ability to respond to lower levels of distortional stress, strain (e.g. high strain rates result in increased intracellular calcium (Landsman, et al., 1995)), and even non-distortional stress (e.g. hydrostatic pressure leads to increased mRNA production in chondrocytes (Smith, R. L., et al., 1996)). For this reason, variables representing both strain-based and stress-based damage criteria were extracted from the optimized model for comparison to plantar contact pressure.

Where possible, invariants of stress and strain were used as scalar descriptors of the tensor valued fields. Non-distortional stress, or hydrostatic internal pressure, was extracted as 1/3 of the first invariant of the stress tensor. Distortional, or shear stress, was extracted as the second invariant of the stress deviator (also known as von Mises stress). The maximum principal stress was extracted as a measure of the magnitude of combined (distortional and non-distortional) stress acting at each material point. Maximum principal strain was used as an indicator of possible strain-induced failure.

The relationship between contact pressure and internal stress and strain was further investigated by inserting a 12.7 mm (0.5") thick foam mat beneath the forefoot model (Figure 4.1B). The mat was given material properties of Poron® Cushioning (Rogers Corporation, Rogers, CT), a common insole material used to decrease peak plantar contact pressure. The foam mat was modeled as a highly compressible, hyperelastic material using the ABAQUS® implemented hyperfoam material model (ABAQUS, 2006). 3rd order Poron hyperfoam material parameters were μ_1 = 0.147 MPa, α_1 = 4.613, β_1 = -0.029, μ_2 = 0.233 MPa, α_2 = 4.916,

β_2 = -0.056, μ_3 = 0.260 MPa, α_3 = 4.528, and β_3 = -0.30 (Petre, M. T., et al., 2006).The foam mat simulation was completed under the same GRF load and optimized joint configuration as the barefoot simulation. Peak plantar contact pressures and measures of internal stress and strain were extracted from the foam contact model for comparison to the barefoot values.

To investigate the sensitivity of internal variable predictions to possible errors in material property definitions, the parameters of each material layer were perturbed. The perturbation involved 10% increases in both μ and α for the given material. The barefoot model was solved with perturbed fat, perturbed muscle, perturbed skin, and with all three materials perturbed simultaneously. Internal variable values were extracted as previously discussed.

Due to difficulty generating multi-tissue 3D forefoot meshes, it was not feasible to create models with altered mesh density to investigate the effects of the finite element mesh on model predictions in the sub-metatarsal head region. Instead, an easily modifiable 2D plane-strain model of the 2nd ray of the forefoot was generated. 2D model geometry was based on a sagittal section through the 3D finite element model (Figure 4.3). Material properties for fat pad, skin, muscle, and lumped toes were identical to the 3D model, except that dorsal skin was not included in the 2D model because without a physical connection to the plantar skin, it has little influence on predictions in the sub-metatarsal head region. The portion of the GRF that should be carried by a 1mm thick slice of the second ray is unknown, so 2D model simulations were carried out under displacement control, with the metatarsal bone being depressed down into a rigid

floor (Figure 4.3). For this reason, results from the 2D model cannot be compared to results from the 3D model but are instead meant to show relative differences caused by changing the density of the finite element mesh. To investigate the effect of mesh density on model predictions, 2D meshes of 1,160, 3,633, and 15,066 rectangular, first order elements were generated.

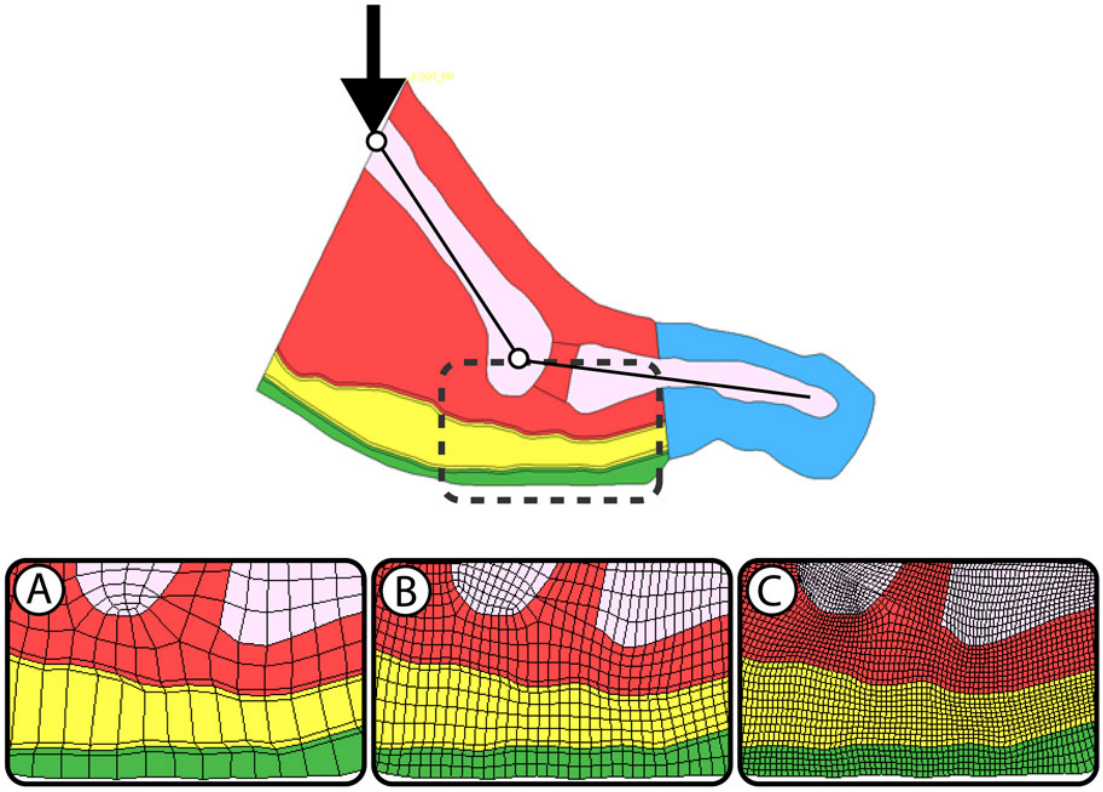

Figure 4.3. The 2D model of the subject's 2nd ray incorporating bones, plantar skin and fat pad, and a lumped muscle section. This model was used to determine the effects of mesh refinement on prediction of internal variables. The bottom frames show the contact area and region of interest for the (A) 1,160 (B) 3,633 and (C) 15,066 element versions of the model.

Table 4.2. Experimental and model predicted peak plantar pressures within the ten masked regions of the forefoot (Figure 4.2). The location of the largest error (440 kPa) in the initial model prediction, metatarsal 4, was also the location of the largest final error (182 kPa) in the optimized model prediction. Corresponding plantar pressure distributions are shown in Figure 4.4.

	Peak Contact Pressure within Mask (kPa)		
Mask Region	**Experimental**	**Initial Model Predicted**	**Optimized Model Predicted**
Metatarsal 1	340	207	344
Metatarsal 2	570	190	593
Metatarsal 3	475	354	314
Metatarsal 4	300	740	118
Metatarsal 5	55	279	128
Toe 1 (Hallux)	620	86	588
Toe 2	105	28	63
Toe 3	100	23	20
Toe 4	80	120	58
Toe 5	25	57	45
	RMS Error:	268	87

4.4 Results

Prior to optimization of bone configuration, the RMS error in model predictions of plantar pressure was 268 kPa with the model predicting a 4th metatarsal dominant pattern (Table 4.2). After optimizing the bone configuration of the 3D model, the RMS error decreased to 87 kPa and the predicted plantar pressure distribution contained the major landmarks of the experimentally measured distribution at the instant of peak metatarsal head pressure (Figure 4.4). The

predicted peak metatarsal head contact pressure was 593 kPa and was localized under the 2nd metatarsal head. The predicted distributions often appear more focal in nature than the experimental distribution, probably due to differences in effective pressure sensor size. Experimental pressures were collected with a spatial resolution of 4 sensors/cm^2 and the 3D mesh used here created an effective sensor size of about 25 sensors/cm^2. Small fluctuations in the model-predicted plantar pressures can be seen in Figure 4.4.

The barefoot peak von Mises and maximum principal stresses in the plantar skin were well-aligned with the location of peak plantar pressure under the 2nd ray of the forefoot (Figure 4.5A-B, left). Interestingly, the peak von Mises and

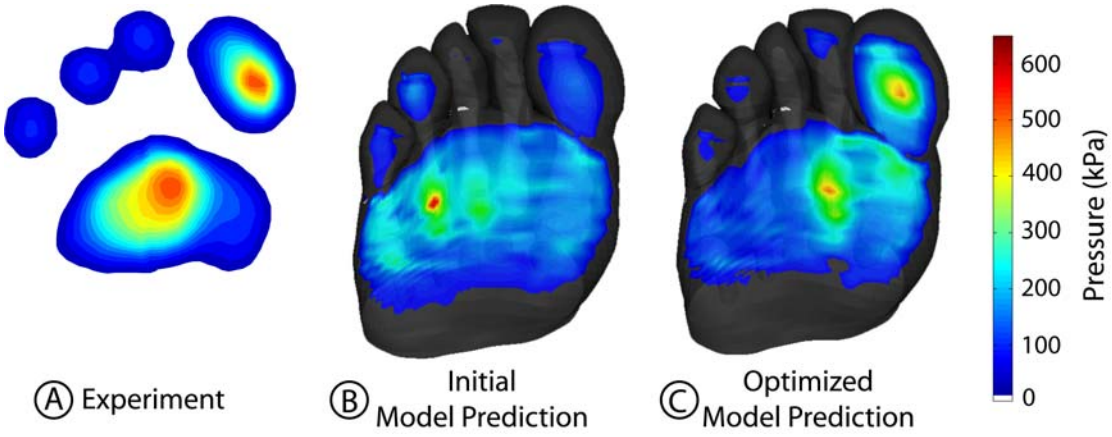

Figure 4.4. (A) The experimental plantar pressure distribution at the instant of peak metatarsal pressure. (B) The plantar contact pressure distribution predicted by the 3D model without optimization of joint configuration. (C) The model predicted distribution after optimization of bone configuration. Note that peak pressures in the optimized pressure distribution are similar in magnitude and location. Values for each masked region are provided in Table 4.2.

maximum principal stresses at the top of the fat pad were higher in magnitude, more focal, and more laterally located (sub-3rd metatarsal) than the skin stresses (Figure 4.5A-B, right). Hydrostatic pressure was much more prominent in the fat pad than in the plantar skin (Figure 4.5C). The peak principal nominal strain was co-located within the maximum principal stress on top of the fat pad.

Possible uncertainty in material parameters appears to effect magnitudes of internal variables (in extreme cases inducing large changes in predicted stresses), but not trends in relative load sharing or location of internal stresses (Table 4.3). The locations of internal stress and strain measures were also relatively unaffected by changes in 2D model mesh density (Table 4.4). Magnitudes, on the other hand, were highest in the fine mesh, followed be the intermediate mesh, and finally the coarse mesh. Values of both stress and strain stabilized between the intermediate and fine meshes. This implies that for the prediction of internal stresses and strains, the minimum necessary element size is somewhere on the order of 0.8 mm on a side. Decreasing element size beyond this value does not appear to be justified for the prediction of internal stresses.

When a piece of cushioning insole foam was introduced between the 3D forefoot model and the rigid floor, the model predicted peak plantar contact pressure fell from 588 kPa to 196 kPa. This magnitude of reduction is commonly seen in comparisons of barefoot and shod walking. In contrast to this decrease in peak surface stress, peak internal stresses located on the dorsal surface of the fat pad below the 3rd metatarsal only decreased by about 2% (Table 4.5). Closer

to the plantar surface, von Mises stresses in the skin were significantly reduced in the area of peak plantar pressure from 559 kPa to 120 kPa (78.5% decrease).

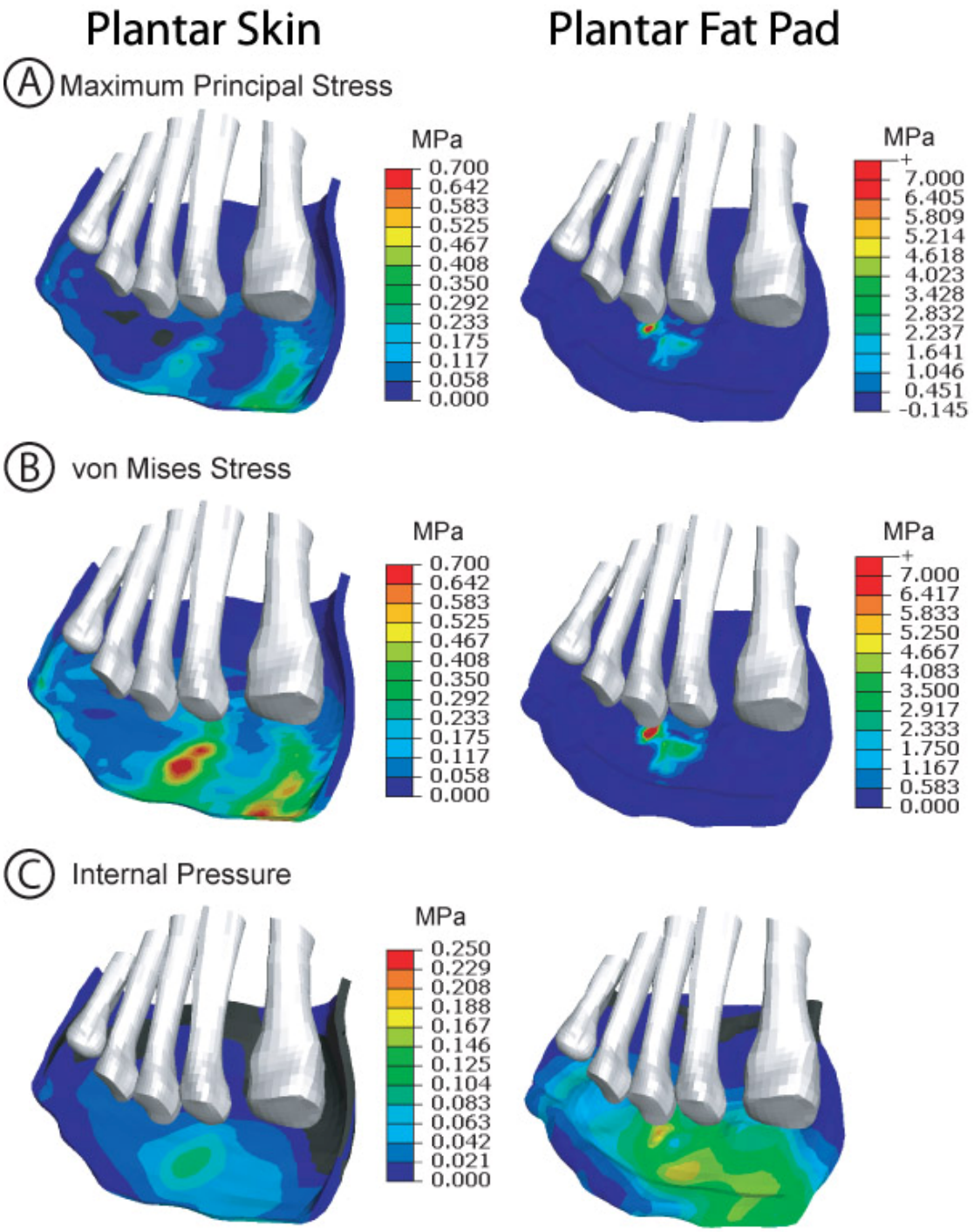

Figure 4.5. (see caption on next page)

Figure 4.5. (see figure on previous page) Toes, phalanges, muscle and dorsal skin have been removed to display the locations of peak internal stress variables for the plantar skin (LEFT) and fat pad (RIGHT). The corresponding plantar pressure distribution is shown in Figure 4.4C and the location of peak plantar pressure is identical to the location of peak von Mises stress in the skin. Maximum principal (A) and von Mises stress (B) appear to provide the same types of information about the internal stress state. Both of these variables are extremely high on the upper surface of the fat pad and have peaks located under the 3rd metatarsal head – a different location than the peak plantar contact pressure. This high stress concentration from the bones is dispersed across the fat pad such that at the upper surface of the skin, its magnitude has been decreased by a factor of 10. The mechanism by which this is accomplished appears to be conversion of focal deviatoric stress to more uniformly distributed hydrostatic pressure in the fat pad (C).

Table 4.3: Changes in internal variables in the plantar fat pad and skin when material properties were perturbed (10% increase in μ and α). Small errors in material parameters appear to affect the magnitudes of internal stresses and strains but not the trends in locations. Model outputs are least sensitive to changes in materials with the smallest relative volumes (skin and fat). MTH = metatarsal head.

Variable		Perturbed Material			
		Skin	**Fat Pad**	**Muscle**	**All**
Peak Metatarsal Plantar Pressure (kPa)	Value	618	612	836	919
	Location	Sub-MTH2	Sub-MTH2	Sub-MTH2	Sub-MTH2
Peak Maximal Principal Stress (MPa)	Value	1.16	1.42	2.60	3.38
	Location	Dorsal Fat Pad, Sub-MTH3	Dorsal Fat Pad, Sub-MTH3	Dorsal Fat Pad, Sub-MTH3	Dorsal Fat Pad, Sub-MTH3
Peak von Mises Stress (MPa)	Value	1.83	2.23	4.03	5.26
	Location	Dorsal Fat Pad, Sub-MTH3	Dorsal Fat Pad, Sub-MTH3	Dorsal Fat Pad, Sub-MTH3	Dorsal Fat Pad, Sub-MTH3
Peak Hydrostatic Pressure (kPa)	Value	199	191	206	200
	Location	Mid-Fat Pad, Sub-MTH2	Mid-Fat Pad, Sub-MTH2	Dorsal Fat Pad, Sub-MTH3	Dorsal Fat Pad, Sub-MTH3
Peak Nominal Strain (mm/mm)	Value	0.65	0.60	0.79	0.73
	Location	Dorsal Fat Pad, Sub-MTH3	Dorsal Fat Pad, Sub-MTH3	Dorsal Fat Pad, Sub-MTH3	Dorsal Fat Pad, Sub-MTH3

Table 4.4. Internal variable predictions made by the 2D model at the varying mesh densities shown in Figure 4.3. The force induced by applied displacement was nearly identical for all mesh densities. Sides of a representative element in the sub-metatarsal head region were measured to provide a reference for the degree of mesh refinement. For comparison, the 3D forefoot mesh contained 40,000 elements with an average element side length of about 1.8 mm, placing it between the coarse and intermediate 2D meshes. Anatomical locations of peak occurrence were consistent for all mesh densities and variables.

		Coarse Density	Interme-diate Density	Fine Density
	Number of Elements	1,160	3,633	15,066
	Approx-imate Element Side Length (mm)	2.08	0.86	0.49
Peak Plantar Pressure (kPa)	**Value**	384	413	419
	Location	Sub-2nd Phalange Base		
Peak von Mises Stress (MPa)	**Value**	0.7211	0.969	0.936
	Location	Muscle at Base of 2nd Phalange		
Peak Hydros-tatic Pressure (MPa)	**Value**	0.1962	0.2015	0.2097
	Location	Fat Pad under Base of 2nd Pha-lange		
Peak In-Plane Maximum Principal Stress (MPa)	**Value**	0.272	0.401	0.378
	Location	Muscle at Base of 2nd Phalange		
Peak In-Plane Nominal Strain (mm/mm)	**Value**	0.472	0.457	0.448
	Location	Fat Pad at Edges of Plantar Con-tact Region		
Force (N)	**Value**	9	9.04	9.07

Table 4.5: Changes in internal variables in the plantar fat pad and skin when peak plantar pressure is reduced by cushioning the foot with an insole material. % change refers to the difference from the default (barefoot) model. MTH = metatarsal head

Variable		3D Bare-foot Model	3D Foam Carpet Model
Peak Metatarsal Plantar Pressure (kPa)	Value	588	196
	Location	sub-MTH2	Sub-MTH2
	% Change		66%
Peak Maximal Principal Stress (MPa)	Value	1.15	1.13
	Location	Top of fat pad, sub-MTH3	Top of fat pad, sub-MTH3
	% Change		2%
Peak von Mises Stress (MPa)	Value	1.82	1.78
	Location	Top of fat pad, sub-MTH3	Top of fat pad, sub-MTH3
	% Change		2%
Peak Hydrostatic Pressure (kPa)	Value	199	195
	Location	Top of fat pad, sub-MTH3	Top of fat pad, sub-MTH3
	% Change		2%
Peak Nominal Strain (mm/mm)	Value	0.652	0.653
	Location	Top of fat pad, sub-MTH3	Top of fat pad, sub-MTH3
	% Change		No Change

4.5 Discussion and Conclusions

The 3D model presented here exhibited a number of features that enhanced its realism and the likelihood that it would provide good predictions of internal stress in the plantar skin and fat pad. These included: 1) accurate soft tissue geometry which was extracted from un-deformed MRI image sets 2) loading boundary conditions (GRF and plantar pressure distribution) that were good representations of experimental data collected from the modeled foot and 3) skin and plantar fat pad material properties that were determined using an *in vivo* method that characterized them under similar combined loading conditions. Three-dimensional model predictions in the toes, areas directly surrounding the joints, and muscle tissue may not be accurate due to lumping of multiple tissues into one material model and the exclusion of important load bearing structures such as the joint capsules and deep transverse ligaments.

Prediction of the experimental plantar pressure distribution was greatly enhanced by optimization of bone configuration (Table 4.2). This is an important finding and it suggests that models which do not represent all important structures of the foot must be tuned from their generated state in order to represent instants of gait when bone posture is different than it was during model creation. This is not a surprising finding since the foot is an extremely mobile structure.

The bones appeared to act as stress risers, leading to high von Mises stress on the dorsal surface of the fat pad (Figure 4.5B). The fat pad acted as an effective distributor of this load, decreasing it by an order of magnitude before it reached the top surface of the skin (Figure 4.5B, left). The mechanism by which

the fat pad distributed the load may have been conversion of focal von Mises stresses to dispersed hydrostatic pressure (Figure 4.5, bottom, right), which was shown to be prominent in plantar fat pads here and elsewhere (Spears, et al., 2007).

The model solution obtained on a foam cushioning mat simulated barefoot walking on soft carpet rather than on simulated therapeutic footwear interventions. Nonetheless, it resulted in decreased peak plantar pressures and was a valid exploration for determining if the clinical goal of lowering peak plantar pressure results in a consistent reduction in internal stress and strain. The model suggested that lowering peak surface pressures does not necessarily change the peak internal von Mises stress which continues to occur on the dorsal surface of the fat pad as in Figure 4.5B (Table 4.5). Stresses in the skin however, were reduced by 78.5% implying that the foam mat may have therapeutic action through the reduction of stresses in the skin and near the skin-fat interface, but not deeper within the tissues. This trend may not hold true for all individuals or for more aggressive pressure reducing strategies such as firm metatarsal bars. Additional studies are needed to determine the relationship between plantar pressure and internal stress with more realistic footwear interventions such as total contact insoles. These footwear simulations may need to apply optimized joint moments rather than optimized joint angles because, when presented with a compliant contact surface, it is more likely that the foot will adapt by altering its configuration (with fixed loading) than by altering its loading (with fixed configura-

tion). This could not be accomplished in the current study due to solver tions in applying load control to joint connectors.

The peak stress magnitudes reported in this study are difficult to compare to other published results because important modeling decisions vary from the methods described here or are not reported in the literature. For example, previous 2D models have predicted peak internal plantar soft tissue von Mises stresses of about 150 kPa during standing (Gefen, 2003). This value is an order of magnitude lower than the peaks reported here, but Gefen did not include individual tissue layers in his model or provide a characteristic element size and it was not clear whether the 2D models used a plane-strain or plane-stress assumption.

Studies of the effects of element size on internal stress predictions were made possible using an easily adaptable 2D model of the 2nd ray. The 2D model predictions appeared to stabilize when the element size was on the order of 0.8 mm per side (Table 4, Figure 6). This goal mesh density is likely to be sensitive to subject-specific bone geometry and the size of the smallest foot structure modeled. While these 2D models can provide general information that is useful for the development of 3D finite element models, they do not have the ability to inform considerations of out-of-plane stresses or sharing of loads between rays of the foot. The 3D forefoot used in this investigation was generated without the benefit of a suggested minimum element size. With an approximate element size of 1.8 mm per side, the 3D model may still be in the region of mesh sensitivity. Fortunately, it appears that even low density meshes are capable of predicting

the correct location of focal stresses (Table 4.4) and any errors in predicted magnitudes will be systematic so that the relative change between barefoot and cushioned simulations should not be affected.

General features of the predicted plantar pressure distributions were in good agreement with the experiments, but the contours of the predicted pressure distributions (and other surface variables) contained unexpected ripples (Figure 4.4). These non-smooth distributions appeared in both frictionless and high friction (μ = 0.5) models, models using penalty and Lagrange multiplier contact definitions, and models with fully incompressible and nearly incompressible materials. They were also present in the results from models with and without horizontal loading applied. The features were also present, and somewhat more pronounced, in models with higher mesh densities (Figure 4.6). A smooth plantar pressure distribution can be obtained by assigning all tissue layers the same material properties (Figure 4.7), implying that the ripples are related to the use of layered materials. They may be an artifact related to the extreme transi tions in stiffness present between the fat pad and surrounding tissues. If this is the case, surface irregularities may be eliminated through a more physiological approach to modeling the skin-fat interface including a region of transition tissue with material properties between those of the skin and those of the fat. The effects of these surface irregularities on the ability of the model to make internal predictions are not presently known.

In conclusion, 2D and 3D layered finite element models are useful for the prediction of the internal stress and strain state of the foot provided they are

appropriately generated. This work implied that for prediction of internal variables, the ideal element size is around 0.8 mm per side. It appears that smooth material transitions may be necessary to avoid artifacts when stacking layers with significantly different material properties. A soft foam mat was shown to reduce internal skin stresses, but not internal fat pad stresses. Without additional knowledge about the biological component of foot tissue damage (i.e. what causes cell death or tissue damage), it is difficult to extend this internal stress information to predictions about the formation of ulcers. Although internal stresses have traditionally been investigated in the barefoot condition (Gefen, 2003), future studies should expand on evaluation of the efficacy of therapeutic footwear interventions.

4.6 Acknowledgements

This study was supported by NIH Grant # 5R01 HD037433, the Cleveland Clinic Research Programs Council, and Marc Petre was supported by NIH Grant # T32 AR50959.

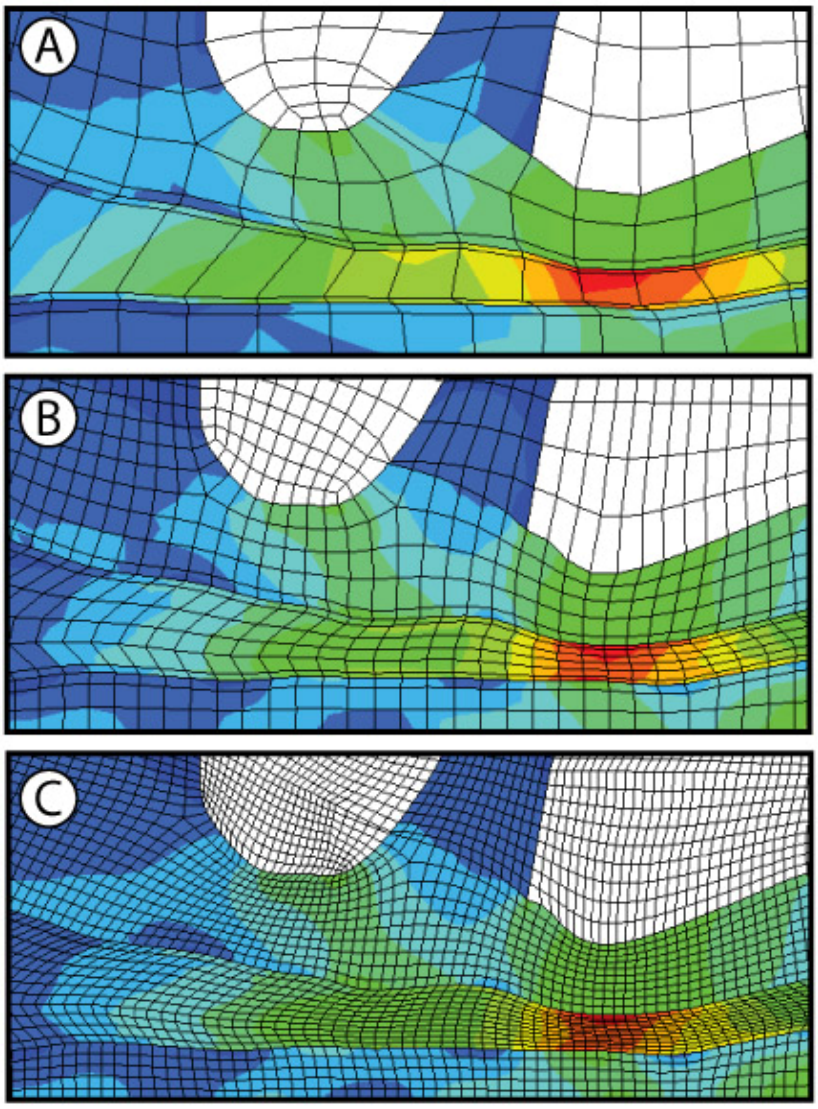

Figure 4.6: A detail of the plantar contact region of the 2D model showing irregularities in the internal pressure distribution near material interfaces. These irregularities are believed to contribute to the non-continuous plantar pressure distributions seen in Figure 4.4. These discontinuities appear to be independent of mesh density and, in fact, become better defined as the average element side length is decreased from (A) 2.08 to (B) 0.86 to (C) 0.49 mm.

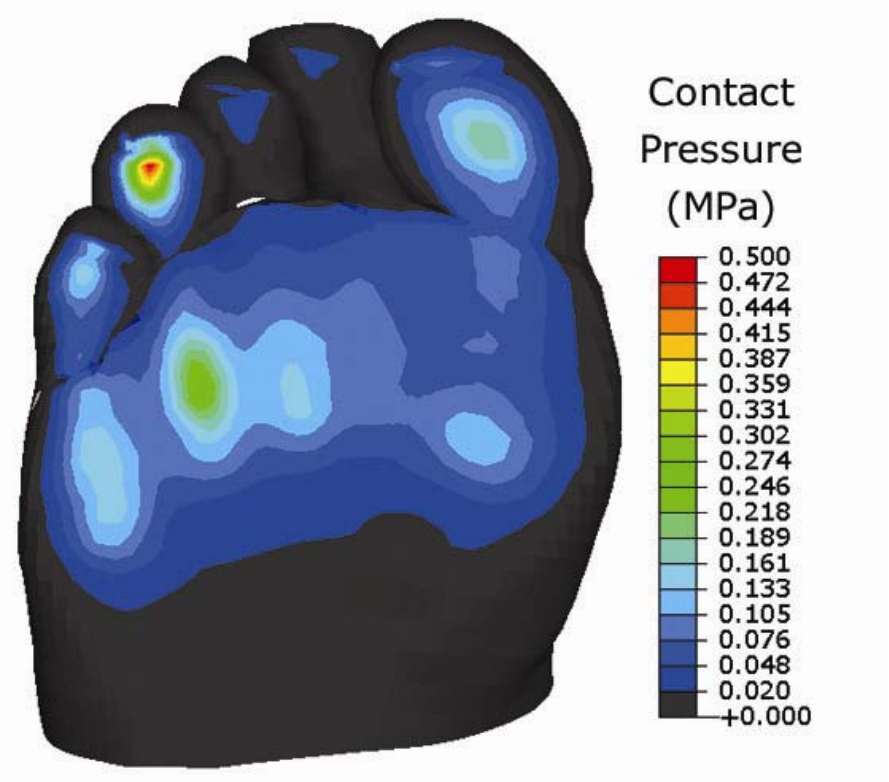

Figure 4.7. When all tissues of the model shown in Figure 4.4B are given the same lumped material parameters (μ=14.3 kPa, α=7.3), the resulting plantar pressure distribution is smooth. This implies that the appearance of distributions in Figure 4.4 is due to layering of dissimilar materials.

CHAPTER 5

Summary and Conclusions

5.1 Summary

MRI images of the foot collected in both the undeformed and deformed states provide a detailed and unique view of *in vivo* 3D deformations in foot soft tissues. The data set of image series from 10 feet produced in Chapter 2 has the potential to provide insight into the mechanical behavior of forefoot tissues and was used in this study for the determination of material properties for skin, plantar fat pad, and muscle.

An inverse finite element optimization technique was developed to determine Ogden hyperelastic material parameters for foot soft tissues from the *in vivo* MRI deformation experiment. Although the foot-loading experiment suggested that the majority of foot strain had already accumulated at 25% loading, information from higher loading levels may be equally important in the characterization of materials. For example, the skin material properties determined in this study predict a high strain stiffening behavior that similar studies at lower loading levels did not (see Figure 3.7) (Spears, et al., 2007).

The resulting fat and skin material parameters agree with some recently published results from the heel of the foot (Spears, et al., 2007) at strains below 0.3 mm/mm, but predict a higher degree of strain stiffening. High stiffness predicted by the skin material properties may indicate that the behavior they predict is more representative of the skin at the plantar surface of the foot than at

the dorsum. The material parameters representing passive muscle are likely to be overly stiff due to the inclusion of ligaments and joint capsules in the section referred to as muscle during material parameter determination. These material properties, in combination with multiple-tissue-component finite element models of the foot, may be used to predict internal stress distributions. Due to the limitations of these material parameters, internal predictions should focus on the plantar skin and fat pad regions of the forefoot, which may be important for the etiology of plantar neuropathic ulcers.

Three-dimensional finite element model predictions of internal stress support the view of the metatarsal heads as stress concentrators. The fat pad appears to distribute high concentrations of stress on its dorsal surface over larger areas of its plantar surface through distributed increases in internal hydrostatic pressure. The peak von Mises stress observed at the dorsal surface of the fat pad was in a different location (below metatarsal 3) than the peak plantar contact pressure (below metatarsal 2). This result reinforces the idea that loading from a metatarsal head may induce stresses in neighboring rays of the foot and emphasizes the importance of modeling the foot in three dimensions.

Insertion of a soft foam mat under the foot resulted in a significant decrease in the plantar contact pressure, but did not significantly alter the magnitude of the peak internal von Mises stress which was still located beneath the 3rd metatarsal head on the dorsal surface of the fat pad. Skin stresses were significantly reduced by the foam mat implying that the therapeutic mechanism of plantar

pressure relief might be limited to the tissues in the near surface region of the foot.

A thick, soft foam intervention is unlikely to be implemented in therapeutic footwear and more realistic interventions should be considered. Differences in the locations of peak internal and peak external stresses imply that more aggressive footwear interventions prescribed based on surface measurements may have unintentional effects on the internal stress distributions. For example, a soft midsole plug placed under the 2nd metatarsal head of the modeled subject may reduce the peak plantar pressure, but may increase the already elevated peak internal stress between the top of the fat pad and the 3rd metatarsal head.

5.2 Original Contributions

This collection of studies contains original contributions to the areas of *in vivo* mechanical testing of soft tissues of the human foot, determination of nonlinear material parameters, 3D finite element modeling of the foot, and clinical assessment of foot risk due to mechanical loading. The MRI foot-loading technique described in Chapter 2 and Appendix A provides the ability to apply high, GRF equivalent, loads including shear forces which were not possible in previous *in vivo* MRI (Gefen, et al., 2001) and CT (Smith, K. E., et al., 2000) foot loading experiments. This added capability and the high soft tissue contrast of MRI result in the generation of more data (combined loading states, high resolution deformation of individual tissues) for determination of material parameters.

Methods for tracking 3D strains between undeformed and deformed image sets exist in the form of MRI tagging (e.g. (Axel, et al., 2005)) and image registra-

tion techniques (e.g. (Veress, et al., 2005)). However, MRI tagging requires numerous repetitions of the loading cycle and only produces strain data at every third image pixel. Hyperelastic image registration shows great promise in this area, but commercial software is currently unavailable. Strains may be tracked manually by identifying corresponding material points in the undeformed and deformed image sets, but this process is labor intensive, subject to user error and difficult to implement in 3D. The material parameter optimization described in Chapter 3 eliminates the need for a known strain field by directly comparing model predicted and experimental images sets and is the first of its kind to simultaneously determine the material characteristics of 3 separate layers. Resulting tissue properties for skin and plantar forefoot fat pad are the first to be determined from 3D, *in vivo* mechanical testing.

The 3D FE model of the forefoot used for optimization of material parameters in Chapter 3 and prediction of internal variables in Chapter 4 is the first 3D biological model in the literature to incorporate realistic geometry in multiple tissue layers. It represents a significant increase in model complexity and ability to make predictions about internal stresses and their relationship to surface stresses. The 2D, multi-tissue, plane-strain model generated from the second ray of the 3D model has been used to investigate the effects of element size on model predictions. This information will provide a point of reference for future modeling studies that researchers should consider before embarking on the time and resource consuming task of 3D model generation.

Although the approach of using FE models to investigate internal stresses and strains is not new, it has not previously been completed in 3D with well-defined material properties for skin and fat tissue layers. In addition, the applicability of this approach has been extended by adding a pressure reducing foam mat to the model to provide insight into how the clinical goal of lowering peak plantar pressure affects internal stress and strain.

5.3 Limitations

As with many modeling studies, this investigation was limited to detailed analysis of the foot of only one, healthy young subject. It is unknown how the results of this study will translate to other healthy subjects or other subjects, such as those with diabetes, with foot pathology. Although care must be taken in generalizing the results, the novel observations of this study may serve as encouragement for additional thought and experimentation.

The passive foot loading described in Chapter 2 correlates poorly with the active loading that occurs during gait. Action of active tissues (intrinsic and extrinsic foot muscles) during imaging appears to be necessary to directly image gait-like strains in the soft tissues. Due to relatively long image acquisition times and high sensitivity to subject movement it is unlikely that this type of data can be collected using MR imaging.

Extended MRI imaging times also limit the data that can be produced for determination of viscoelastic material properties. Using the plantar fat pad as an example, given an instantaneously applied (and maintained) displacement, the measured force will rapidly decrease over the first 1 second of the test and then

continue to slowly decay over a period of about 1minute (Miller-Young, et al., 2002). The high resolution MRI images used in this study require approximately 3.5 seconds per slice, making this rapid response behavior impossible to capture. High speed MR imaging techniques are becoming available but generally collect only 2D data, require state-of-the-art hardware, and often sacrifice signal-to-noise ratio for speed (Elgort and Duerk, 2005, Reeder and Faranesh, 2000).

The major limitation of the material characterization and modeling portion of this work is that, although this model represents a significant step in modeling of discrete structures within the foot, it fails to uniquely represent all of the tissues including ligaments, tendons, and joint capsules. This limitation is illustrated by the overly stiff predicted behavior (see Figure 3.7) of what was referred to here as passive "muscle" but really represents a grouping of various tissue types. This limitation may lead to errors in the prediction of internal stresses in regions where tissues have been lumped, but should not affect the prediction of stresses in areas of the foot, such as plantar skin and fat pad, where materials are relatively uniform.

It should be noted that this is not a limitation of data collected as described in Chapter 2. These high-resolution images provide enough detail and soft tissue contrast to identify, segment, and model most structures of the forefoot. The limitation on level of detail in the FE model is related to current limitations in mesh generation techniques, processing power, and finite element solver capabilities. As processing power and solver capabilities improve, the addition of

more detail to finite element models of the foot will be possible and the techniques discussed in this work are expected to remain applicable.

Manual segmentation of foot structures may have introduced error in the definition of object boundaries. This error was minimized by including the ability to zoom in on a region of interest within the segmentation software, but definition of some object boundaries, for example the fat/muscle boundary, were often subject to user bias. The resulting segmentation curves represented a sample of the real object boundary information. This sample was further down-sampled during the mesh generation process. The end result of this repeated sampling was the possibility that object boundaries in the layered FE mesh did not agree with object boundaries in the MR images.

Errors in object boundary definitions may affect the optimization of material parameters by causing misalignment between the FE mesh and MR image sets. The use of images re-colored according to object boundaries obtained from segmentation eliminates one source of error between the FE mesh geometry and the MR image geometry. The remaining source of error, mesh sampling of geometry, may lead to difficulty in decreasing optimization error to zero.

For example, consider a node defined to be bone in the FE mesh, but lying outside of the region defined to be bone in the MR image set. In the undeformed state, this node will be assigned the image intensity of muscle rather than bone. As the mesh deforms, the motion of the node will be controlled by the rigid bone properties assigned in the model, but the motion of the MR image material point that the node corresponded to in the undeformed state will be controlled by

muscle material properties in the experiment. Depending on the behavior of surrounding nodes and the amount of deformation, the node and its associated material point may or may not line up in the deformed state. Errors of this type are more likely to occur in the nodes that define the boundary layer of an object. As most nodes of an object are internal nodes, it is assumed that these internal nodes will still drive the optimization to the best solution and errors at surface nodes will contribute to a non-zero final error.

Sampling of geometry may also contribute to errors in the prediction of internal stresses and strains. For example, simplified bone geometry may lead to unrealistic concentration of stress beneath the metatarsal heads. Although not expected to be present, large discrepancies in object thickness may alter the manner in which loads are shared between tissue layers.

The layered-tissue finite element model predicted plantar pressure distributions were unexpectedly non-smooth (Figure 4.4). The cause of these fluctuations in surface pressure is currently unknown, but does not appear to be related to mesh density, contact definition, or friction. It is suspected that the irregularities are related to the sharp transitions in material properties between the fat pad and neighboring tissues. This sharp transition is unlikely to be physiologically correct as transitions between the plantar foot tissues are generally gradual in nature. Mechanical properties at the skin/fat interface have been shown to be altered in some pathological conditions, such as long term diabetes (Chen, Y., 2003). Resolution of this issue may require the inclusion of transition layers which bridge the material properties of one layer to the next.

5.4 Future Work

Only the data from one of the subjects involved in this study was developed into a finite element model for further analysis. Similar work should be carried out using the data of the other 9 subjects to determine whether or not the observations from the current subject will hold-up in a larger (albeit still healthy and young) group of individuals. MRI image series have already been collected and segmented for these nine subjects so the remaining tasks include finite element model generation, material property determination, and simulation of the instant of peak metatarsal pressure.

Past attempts to define differences in the mechanical properties of soft tissues between diabetic and non-diabetic populations have often been underwhelming due to large inter-subject variation in both populations (e.g. (Erdemir, et al., 2006)). This may be due in part to the lumped material analysis techniques, such as ultrasound heel pad indentation, commonly used. For example, if skin stiffens due to long duration exposure to hyperglycemia, but muscle softens as a result of fat infiltration, then these effects may offset each other when the bulk mechanical properties are tested. Extension of this research to pathological patient populations might provide additional insight because material properties can be determined in a layer specific manner.

The model described here requires further refinement in terms of mesh density, number of tissue components, and material definitions. Mesh refinements may come in the form of localized increases in mesh density or implementation of automated re-meshing of highly deformed areas. After the

skin and fat pad, the next most important structures for prediction of internal stresses may be the joint capsules and deep transverse ligaments of the forefoot. Meshing and application of kinematic constraints for these structures represents a significant challenge. Material models may be extended to include rate effects (viscoelasticity) as characterized by multiple investigators (Ledoux and Blevins, 2007, Miller-Young, et al., 2002), and/or material anisotropy, which is expected to be especially important in the skin and muscle.

Although the techniques described here are too time- and resource-consuming to have direct clinical utility (e.g. prediction of a patient's internal stress state), they may, in the future, be useful for providing clinicians with general guidelines for therapeutic footwear design. More aggressive off-loading devices such as metatarsal pads and bars function by forcing the transfer of load from one region of the foot to another. It is currently unknown how these drastic changes in loading are reflected in terms of the internal stress and strain. While contact pressure measurement will probably remain the gold standard for indicating risk, investigation of internal stresses might be used to choose between two approaches, such as metatarsal pads and midsole plugs, which are equally efficacious in terms of pressure reduction.

Models incorporating materials determined from *in vivo* MRI deformation data may have an improved ability to predict contact shear distributions as a result of the inclusion of multi-axial test data during parameter determination. This type of prediction is desirable and questionable for the same reason – there is no commonly available device for measuring the distribution of shear forces

between the foot and shoe. Measurements of barefoot shear distributions have been collected using specialized devices (e.g. (Perry, et al., 2002)) and may be used to validate in shoe predictions.

Any predictions made by this type of finite element model must be evaluated in the context of tissue damage. Unfortunately, the connection between mechanical loading and cell death and/or tissue destruction is poorly understood. *In vitro* characterization of cellular responses to stress and strain would be of great use in evaluating modeling results, and conversely, results from the models used in this investigation may be used to determine the loading environment that should be simulated *in vitro*.

Appendix A: Foot Loading Device

A.1 Design

A.1.1 Loading Device Assembly

The device pictured in Figure 2.2 was designed to passively load the fore-foot with GRF-like loads. Force was applied by two water actuated pistons aligned perpendicular to each other to apply vertical and net horizontal loading. The pistons are embedded into a sliding housing that allowed the vertical piston (and attached loading plate) to translate sideways along a fixed direction under the action of the horizontal piston. The horizontal line of action could be fixed at any angle to reproduce the net horizontal GRF by rotating the track in which the piston housing slides and using a nylon set screw to lock it in place. The rotating insert was contained inside of a thick polycarbonate shell that provided durability. A lip on the polycarbonate shell prevented the casting material used to attach the device to the foot from blocking vertical or horizontal translation of the loading plate.

In a hydraulic system, piston force is directly proportional to the system pressure with a constant of proportionality equal to the cross-sectional area of the piston. This theoretical relationship was verified by placing the two loading pistons against a force transducer and applying a series of known system pressures (Figure A.1). Contact with the rigidly fixed force transducer was made at a stroke length of about 3 mm and force was allowed to develop at this fixed piston extension. The resulting data fell on a line with slope equal to the piston area in

each case (Figure A.2). Simulating the GRF of a 136 kg (300 lb man) (1.2 times body weight) would require system pressure in the vertical piston of about 3.45 MPa (500 psi). Pressures of this magnitude are likely to overwhelm the piston seals but could be otherwise handled by the hydraulic system (see below).

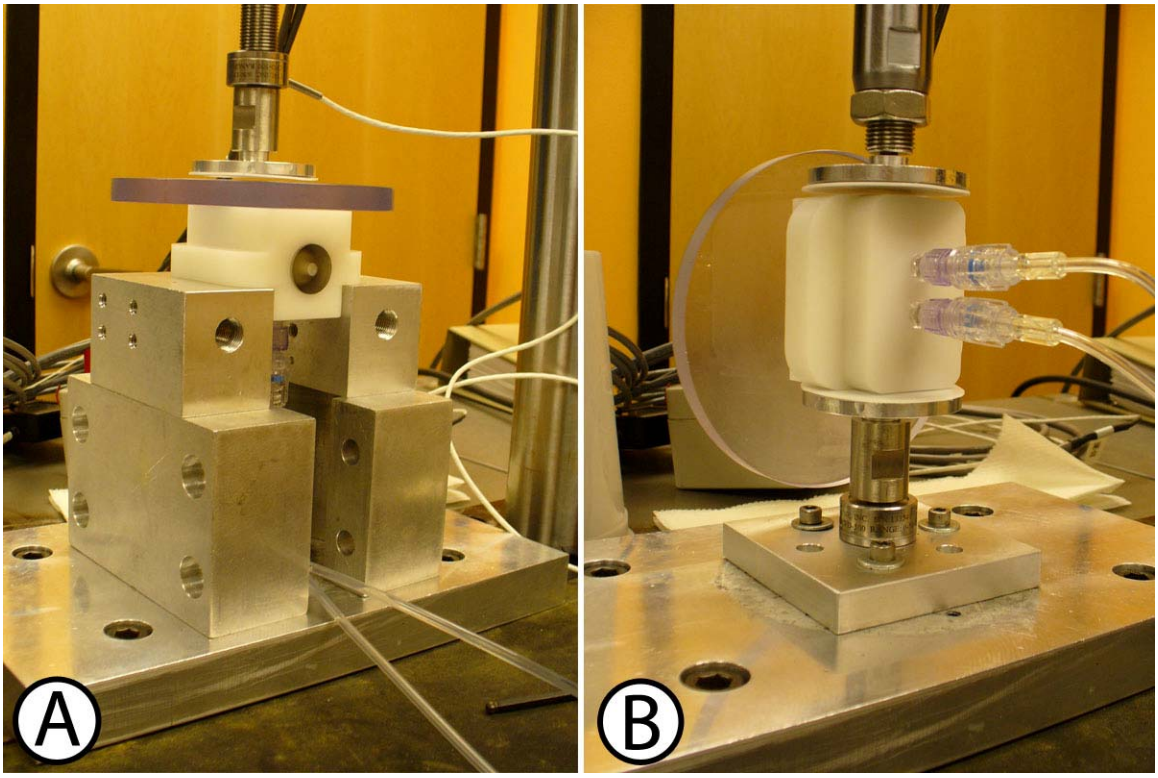

Figure A.1. Experimental configurations for verifying the calibrations of the (A) vertical and (B) horizontal loading pistons. The vertical piston rod was attached to the loading plate that made contact with the foot (A). Piston supply lines are seen entering the piston housing from the bottom of the device in (B).

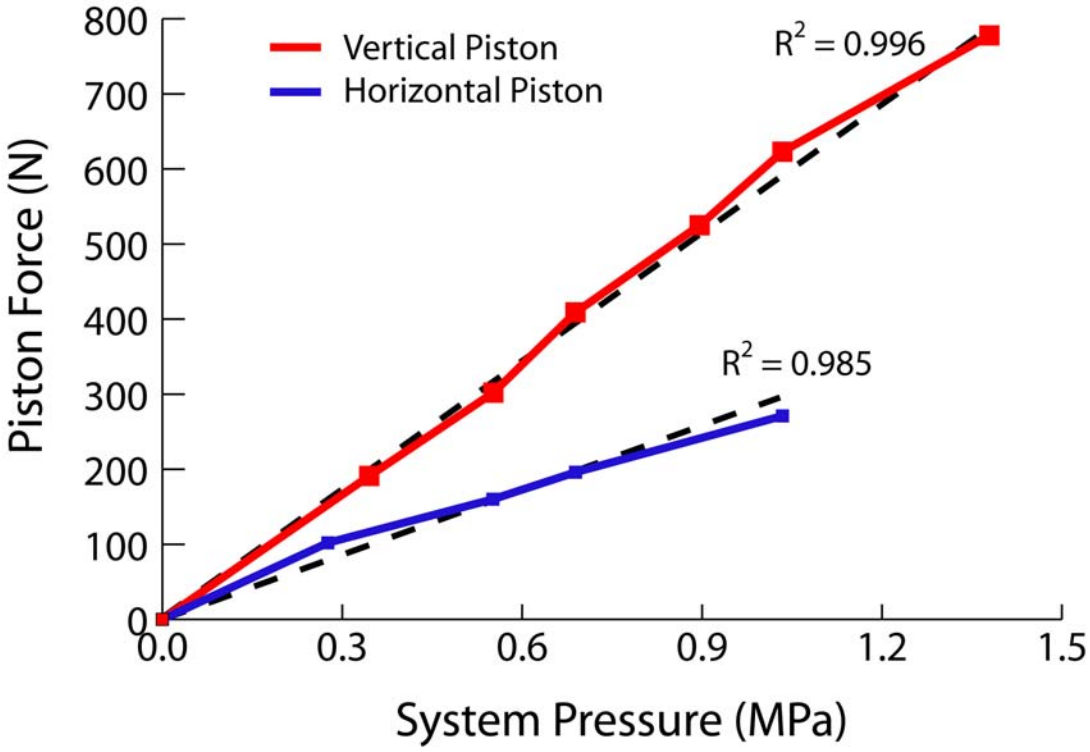

Figure A.2. Calibration lines for the vertical and horizontal loading pistons. The slopes of the lines are the respective piston areas (vertical ≅ 506.7 mm^2, horizontal ≅ 285 mm^2).

A.1.2 Foot Attachment

Passive loading of the plantar surface of the foot required that the dorsum of the foot be fixed in place relative to the loading device. The initial design used wide nylon webbing straps to hold the device to the foot, but the straps pinched the dorsum of the foot at high loads. Foam padding was added to distribute the load over more dorsal surface, but the attachment was still uncomfortable. The final solution was to maximize conforming contact area with the dorsum of the foot by applying a customized fiberglass cast (see Figure 2.3). In addition to the

forefoot, casting of the ankle further distributed the load and ensured that the proper sagittal plane pose would be maintained during the experiment.

A.1.3 Hydraulic System

Hydraulic system pressure was controlled using a hand pump and series of manual valves (Figure A.3). The hand pump was fed by an ordinary sink and

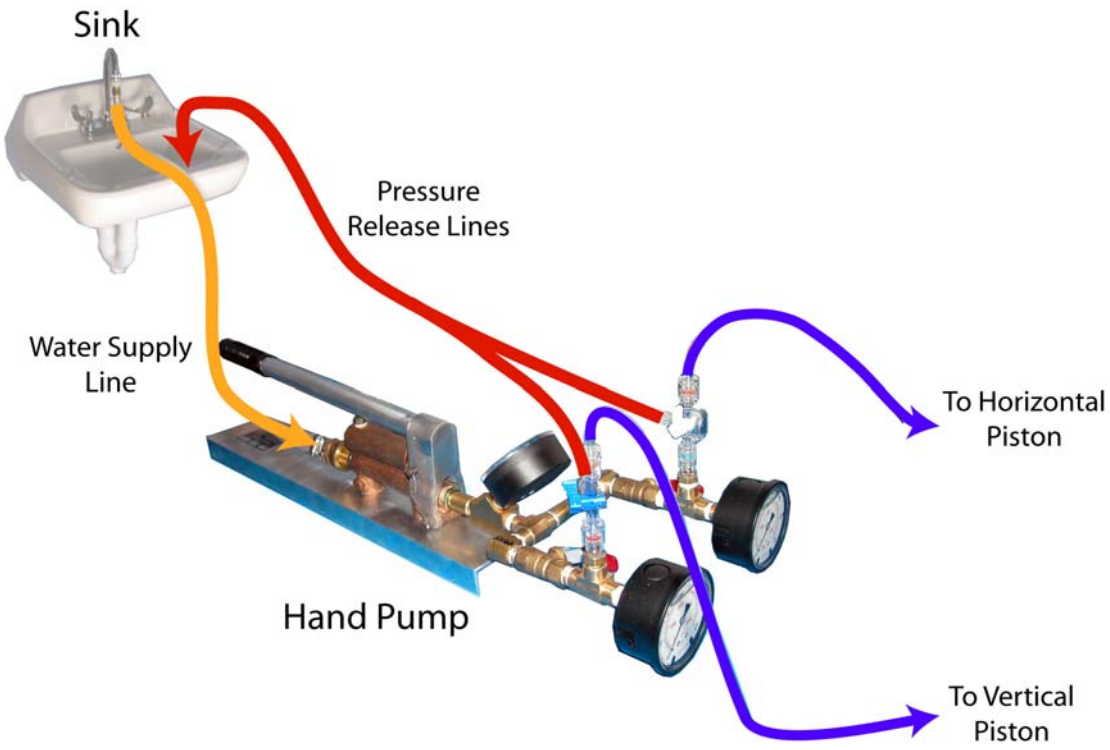

Figure A.3. The hand pump and system of valves used to control system pressure in the two loading device pistons. Pressure for each piston can be independently controlled.

required an input pressure of about 10 psi to fill the pump chamber (a requirement easily met by building water pressure). Piston supply lines were constructed out of special high pressure surgical tubing with a rating of 1,200 psi connected with high pressure fittings rated at 1,000 psi. The supply lines, which

ran from the hand pump located in the MRI observation room, through the RF shielding isolation ports, and into the imaging suite (Figure A.4), were purged of air by running water through the lines for 1 minute. The lines were then capped

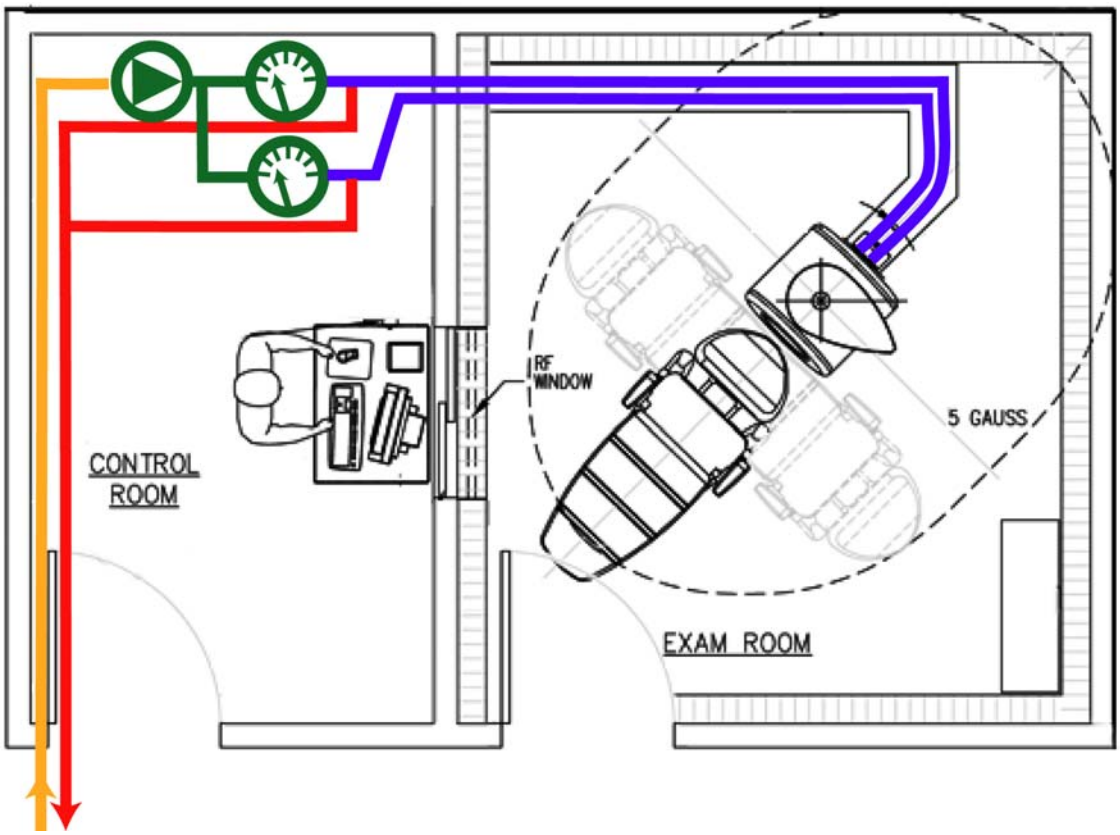

Figure A.4. A schematic diagram of the hydraulic system in relationship to the MRI suite.

and a system pressure of 100 psi was applied to check for leaks. The system was able to maintain 100 psi in this state over a period of ten minutes.

A.2 Application

A.2.1 Device Attachment

Based on the patient's measured walking anterior-posterior and medial-lateral GRFs, the insert in the loading device was rotated to apply the net shear force at the appropriate angle. The insert was locked at this angle using a small nylon set screw in the outer housing. A thin, flexible Pliance® (Novel, Inc., Minneapolis, MN) pressure sensitive array was attached to the top of the loading device using double sided tape. A photograph of the sensor location was taken from above to be used later for alignment. A water-filled syringe was attached to vertical piston input and the piston was displaced approximately 3 mm prior to casting to the subject's foot. Removal of this displacement after casting assured that the foot was fully unloaded inside the cast when the vertical piston was fully retracted.

During casting, the subject was seated in an adjustable exam chair with their legs over the edge. The chair was raised until the subject's foot was hanging, unloaded just above the plate of the loading device. Chair height was adjusted with the forefoot resting on the loading device until the measured sagittal foot pose at the instant of peak MTH plantar pressure was achieved (Figure A.5A). A photograph of the foot location on the device was taken above for later alignment with pressure data.

Casting began with a thin stockinette applied to the subject's foot and lower leg. The portion of the stockinette under the metatarsal heads was removed so that the bare foot made direct contact with the loading plate (Figure A.5B). One layer of cast padding was added to the ankle, midfoot and across the dorsum of

the foot. The cast padding was kept smooth and thin over the dorsum of the foot to eliminate stress concentrations under loading (Figure A.5C). Two layers of 3" wide fiberglass tape (3M Healthcare, St. Paul, MN) was applied over the device, foot, and ankle in a figure-8 pattern (Figure A.5D). The cast was stretched at the dorsum above the toes to make more room for toe movement and eliminate excessive pressure on the tops of the toes (Figure A.5E). Care was taken to maintain access to the input ports for the loading pistons located on the bottom of the device (Figure A.5F). The cast was allowed to dry for 20 minutes prior to removing the pre-applied displacement of the vertical piston and moving the subject to the MRI imaging suite in a wheelchair.

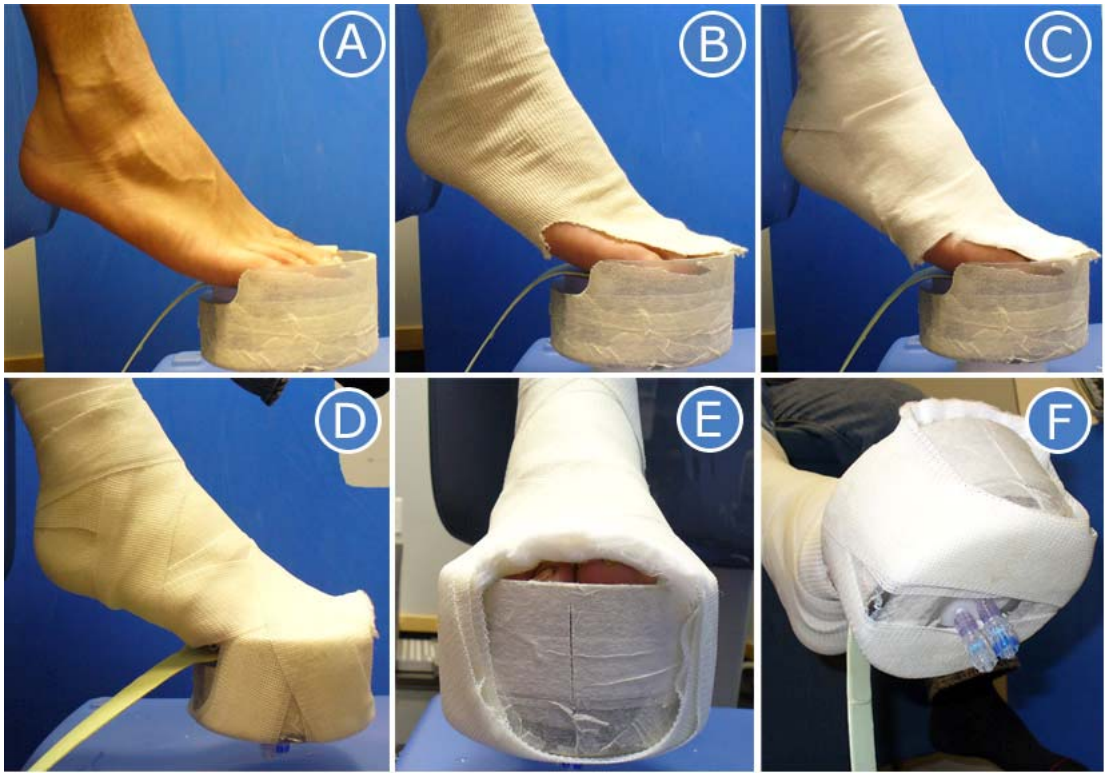

Figure A.5. A step-by-step guide to the loading device attachment process.

A.2.2 In-Device Pressure Measurement

The capacitive sensing technology of the Pliance® pressure mat was not compatible with the rapidly alternating fields during MRI imaging, so in-device plantar pressure measurement was performed just outside of the imaging suite prior to imaging. With the subject seated in a resting position, the pressure measurements were taken in the unloaded state and under the same loads to be applied within the MRI. Pressure was recorded for a period of one minute at each loading level. Pressure monitoring hardware was disconnected from the sensor prior to entering the MRI suite, but the sensor remained in place beneath the subject's foot during imaging.

A.2.3 Loaded Imaging

The subject was assisted from the wheelchair (which remained outside of the imaging suite) to the patient seat in front of the MRI bore and the supply lines were attached to the loading device taking care to connect the vertical piston supply line to the vertical piston input and the horizontal supply line to the horizontal piston input.

A set of low resolution sagittal and axial entry images were collected to ensure that the subject was appropriately positioned in the MRI bore to capture the entire forefoot in the image series. Once appropriately positioned, foam padding was packed around the casted foot and device to fix it in place for all subsequent image series. Unloaded and loaded image sets were then collected with at least 30 seconds of rest between imaging series. One pump was used to control both pistons, so combined loading had to be applied in stages; ½ vertical load, ½

shear load, remainder of vertical load, remainder of shear load. At the end of each imaging series, piston pressure was released by draining fluid back into the sink. To insure that the pistons returned all of the way to their fully retracted state, a syringe was attached to the end of the pressure release tubing and drawn back.

After the last image series the supply lines to the loading device were disconnected and capped. The patient was helped back to the wheelchair and taken to the exam room where the cast was carefully removed using a reciprocating cast saw.

Appendix B: Optimization of Material Parameters

B.1 Description

The optimization of material parameters discussed in Chapter 3 required repeated finite element model updates and solutions and repeated evaluation of MRI image data. This was accomplished using custom Matlab functions which interacted with the finite element solver, creating, submitting, and extracting results from ABAQUS jobs using python scripts. MR image data were converted into a three-dimensional array of pixel values and read into Matlab for error calculations.

The general procedure is described schematically in Figure 3.4 and outlined in section B.2. The actual Matlab functions used for optimization are provided in section B.3. Python scripts are provided in section B.4.

B.2 Optimization Outline

1) INPUT INITIAL GUESS AT PARAMETERS
2) CALCULATE ERROR AT CURRENT POINT
3) CALCULATE NUMERICAL GRADIENT AT CURRENT POINT
    a. Independently perturb each variable (6 ERROR CALCULATIONS)
4) MINIMIZE ALONG GRADIENT
5) CHECK EXIT CRITERIA
6) RETURN TO 2)

At each error calculation:

A. CALL ABAQUS

a. UPDATE MATERIAL PARAMETERS & SUBMIT JOB

i. Python Script: update_mat.py

b. READ RESULTS & PRINT DEFORMED NODAL COORDINATES

i. Python Script: read_nodes.py

B. GET IMAGE INTENSITIES AT CURRENT COORDINATES

C. COMPARE TO INTENSITIES AT ORIGINAL COORDINATES

D. CALCULATE ERROR

B.3 Matlab Code

```
function [par,R,exitflag] = MRI_FEM_opt()
% ------------------------------------------------------------------------
% *note: this script is separated into matlab cells which are best
% viewed using the matlab m-file editor (release 14 or above).
%
% MRI_FEM_opt contains all subfunctions needed to perform the material
% parameter optimization described in:
%
% Petre, MT. "Investigating the Internal Stress/Strain State of the
% Foot Using Magnetic Resonance Imaging and Finite Element Analysis."
% PhD Dissertation, CWRU August 2007.
%
% The final three subfunctions (gmin,smstep,goldenls) may be extracted
% and used for general gradient-based optimizations with a user
% provided objective function.
% ------------------------------------------------------------------------
% INPUT ARGUMENTS
subject = 2;
levels = [25, 50, 75, 100];   % loading levels to be used in error calc

% LOAD IMAGE DATA AS GLOBAL
global im_info;
im_info = load([num2str(subject) '_MRI.mat']);

% DEFINE PARAMETERS
% par = [mu_muscle alpha_muscle mu_skin alpha_skin mu_fatpad al-
pha_fatpad]
par0 = [0.1032 25.13 0.2325 12.24 0.0023 15.43];  % initial guess
method = 'GOLDEN'; %use golden section line search

% CALL OPTIMIZATION FUNCTION
[par,R,exitflag] = gmin(@serial_obj,par0,method,subject,levels);
%------------------------------------------------------------------------

%% OBJECTIVE FUNCTION ----------------------------------------------
```

```
function [error] = serial_obj(par,options,subject,levels)
% This objective function takes in a parameter set:
% [mu_muscle alpha_muscle mu_skin alpha_skin mu_fat alpha_fat]
% and calculates an error between the MRI deformation and the model
% predicted deformation.
%
% DIRECT DEPENDENCIES:
%       e_calc
%       sta_check
% INPUTS:
%       par: the current set of parameters
%       subject: the subject number
%       levels: which levels the error should be calculated for.
%           full set of available levels: [25 50 75 100]
% OUTPUTS:
%       error: scalar error at the current set of parameters
% -------------------------------------------------------------------
% ROUND PARAMETERS TO ABAQUS PRECISION
par = (round(par.*[1e7 1e4 1e7 1e4 1e7 1e4])./[1e7 1e4 1e7 1e4 1e7...
     1e4];

% CHECK IF RESULTS ALREADY EXIST FOR THIS PARAMETER SET
% load previous results
data = dlmread('24k_results.csv');
opar = data(:,1:6);
oerror = data(:,7);
% search for current parameters in list of successful jobs
error = [];
for r = 1:size(opar,1)
    if strcmp(num2str(par),num2str(opar(r,:)));
        % use known error rather than re-running job
        error = oerror(r);
        break
    end
end

% BEGIN ERROR CALCULATION
if ~isempty(error)
    % use known error if it was found above
else
    % remove old job files (if they exist)
    delete('2_load_24k.*');
    % create new input file
    system(['abaqus CAE noGUI=update_mat.py -- ' num2str(par)]);
    % run abaqus job (try with mpi)
    system(['abaqus job=' num2str(subject) '_load_24k interactive...
            mp_mode=mpi cpus=2']);
    % extract node movement from odb
    system(['abaqus CAE noGUI=read_nodes.py']);

    while 1
        % check to see if job was successful
        flag = sta_check('2_load_24k.sta');
        if flag == 0
            % job was successful, calculate error
            error = e_calc(subject,levels);
```

```
            break
        elseif flag == 1
            % job crashed - skip e_calc and assign a large error
            error = 1e10;
            % retain message file to see why model crashed
            a = clock;
            time = ['date' num2str(a(2)) '-' num2str(a(3)) 'time'...
                  num2str(a(4)) num2str(a(5))];
            copyfile('2_load_24k.msg',[time '.msg']);
            copyfile('2_load_24k.sta',[time '.sta']);
            break
        elseif flag == 2
            % unexpected job termination
            % remove old job files (except input file)
            copy('2_load_24k.inp','temp.inp');
            delete('2_load_24k.*');
            copy('temp.inp','2_load_24k.inp');
            % re-run the job
            if ~exist('tried')
                % try to run again with MPI
                system(['abaqus job=' num2str(subject) '_load_24k'...
                    ' interactive mp_mode=mpi cpus=2']);
                tried = 1;
            elseif tried == 1
                % try to run with threads instead of MPI
                system(['abaqus job=' num2str(subject) '_load_24k'...
                    ' interactive mp_mode=threads cpus=2']);
                tried = 2;
            elseif tried == 2
                % give up
                break
            end
            % extract node movement from odb
            system(['abaqus CAE noGUI=read_nodes.py']);
            error = e_calc(subject,levels);
        end
    end
    if strcmp(options.bounds,'yes')==1
        % apply boundary constraints (add penalty)
        for cp = 1:length(par)
            if par(cp) < options.lb(cp)
                %add penalty to error
                error = error + (options.lb(cp)-par(cp))* ...
                  options.lbpen(cp);
            end
            if par(cp) > options.ub(cp)
                %add penalty to error
                error = error + (par(cp)-options.ub(cp))* ...
                  options.ubpen(cp);
            end
        end
    end
    % add result to list of solutions (csv file)
    dlmwrite('24k_results.csv',[par error],'-append',...
        'precision','%8.7f');
end
```

```
% write result to text file (parameter values at ABAQUS precision)
myfid = fopen(['sub_' num2str(subject) '_evals.txt'],'a+');
fprintf(myfid,'%8.7f %6.4f %8.7f %6.4f %8.7f %6.4f :
%9.2f\n',par,error);
fclose(myfid);
%--------------------------------------------------------------------

%% STA CHECK ---------------------------------------------------------
function [flag] = sta_check(file);
% This function reads the final few characters of ABAQUS status files
% and returns a flag stating whether the job:
%     1) completed successfully
%     2) crashed, or 3) terminated unexpectedly
%
% INPUTS:
%   file: name of sta file
%
% OUTPUTS:
%   flag: job termination information:
%           flag = 0 if job completed successfully
%           flag = 1 if job crashed
%           flag = 2 if job terminated unexpectedly (with no error
%                 message)
%--------------------------------------------------------------------
fid = fopen(file);
% read the last few characters in the file
fseek(fid,0,'eof');
c = [];
for a = 1:200
    c = [c fscanf(fid,'%c',1)];
    fseek(fid,-2,'cof');
end
sta = fliplr(c);
% read sta message
if findstr(sta,'HAS COMPLETED SUCCESSFULLY')
    % successful job completion
    flag = 0;
elseif findstr(sta,'HAS NOT BEEN COMPLETED')
    % job crashed
    flag = 1;
else
    % job terminated unexpectedly
    flag = 2;
end
fclose(fid);
%--------------------------------------------------------------------

%% ERROR CALCULATION -------------------------------------------------
function [e] = e_calc(subject,levels)
% Calculate errors at each requested level based on node location text
% files and subject images (previously loaded as global).
%
% INPUTS:
%   file: name of a file containing nodal coordinates
%
% OUTPUTS:
```

```
%   N: the nodal coordinates in format: node#,x_coord,y_coord,z_coord
%
% DIRECT DEPENDENCIES:
%   read_nodes
%   im_compare
%--------------------------------------------------------------------------
e = 0;
c0 = read_nodes(['sub_' num2str(subject) '.npf']);
if isempty(find(levels == 25)) == 0
    c25 = read_nodes(['Load_25_sub_' num2str(subject) '.npf']);
    e25 = im_compare(c0,c25,25,subject);
    e = e + e25;
end
if isempty(find(levels == 50)) == 0
    c50 = read_nodes(['Load_50_sub_' num2str(subject) '.npf']);
    e50 = im_compare(c0,c50,50,subject);
    e = e + e50;
end
if isempty(find(levels == 75)) == 0
    c75 = read_nodes(['Load_75_sub_' num2str(subject) '.npf']);
    e75 = im_compare(c0,c75,75,subject);
    e = e + e75;
end
if isempty(find(levels == 100)) == 0
    c100 = read_nodes(['Load_100_sub_' num2str(subject) '.npf']);
    e100 = im_compare(c0,c100,100,subject);
    e = e + e100;
end
%--------------------------------------------------------------------------

%% READ_NODES ------------------------------------------------------------
function N = read_nodes(file)
% Read node coordinate information from ABAQSU output text file
%
% INPUTS:
%   file: name of a file containing nodal coordinates
%
% OUTPUTS:
%   N: the nodal coordinates in format: node#,x_coord,y_coord,z_coord
%--------------------------------------------------------------------------
fid = fopen(file);
i = 0;
while 1
    % break if end of file
    dmy = fgetl(fid);
    if dmy == -1
        break
        % look for coordinate header
    elseif isempty(strfind(dmy,'Step: ')) == 0
        step = strrep(dmy,'   Step: ','');
        for h = 1:11
            fgetl(fid);
        end
        % read coordinates
        i = 0;
        dmy = str2num(fgetl(fid));
        while 1
```

```
            if ~isempty(dmy)
                i = i + 1;
                N(i,:) = dmy(1:4);
                dmy = str2num(fgetl(fid));
            else
                break
            end
        end
    end
end
fclose(fid);

%% IM_COMPARE ----------------------------------------------------------
function [e] = im_compare(initial,final,level,subject)
% calculate the difference in nodal image intensity before and after
% deformation.
%
% INPUTS:
%   initial: a list of nodal coordinates in the undeformed condition
%   final: a list of nodal coordinates in the deformed condition
%   level: the deformation level being investigated (25, 50, 75 or 100)
%   subject: the subject number
%
% OUTPUTS:
%   e: the RMS nodal error as calculated below
%-------------------------------------------------------------------------
% scale node coordinates from mm to pixels
global im_info;
scale = 1/0.2734; % pixels/mm
thick = 1/2; % slice/mm
initial = [initial(:,2:3)*scale initial(:,4)*thick];
final = [final(:,2:3)*scale final(:,4)*thick];
% find initial intensity values
init = interp3(im_info.I.I0,initial(:,1),initial(:,2),initial(:,3));
% find intensity values at the current position at the current levels
eval(['cur = interp3(im_info.I.I' num2str(level)
',final(:,1),final(:,2),final(:,3));']);
% remove NaN (out of image range) nodes from calculation
rem_i = find(isnan(init)==1);
rem_c = find(isnan(cur)==1);
rem = unique(sort([rem_i;rem_c]));
init(rem) = []; cur(rem) = [];
% calculate nodal error
err = (init-cur).^2;
e = sum(err);
%-------------------------------------------------------------------------

%% FUNCTIONS BELOW THIS POINT CAN BE USED FOR ANY OPTIMIZATION
% *note: Small changes may be necessary
%*************************************************************************
%*************************************************************************

%% - GMIN CUSTOM OPTIMIZATION FUNCTION ---------------------------------
function [par,r,exitflag] = gmin(obj_fun,par_0,method,subject,levels)
% Gradient-based optimization with capability to calculate numerical
% gradients.  Line search proceeds along the direction of steepest
```

```
% descent using the method defined by input 'method': either a golden
% section line search, of by taking small incremental steps along the
% gradient. The objective function to be minimized must be specified by
% the user.  It must take in a vector of parameters and return a scalar
% error.
%
% INPUTS:
%       obj_fun: a string with the name of a valid m-file
%       par_0:  the intitial parameters (one dimensional array)
%       method: line search method, either:
%               'GOLDEN' to use the 'goldenls' golden section line
%                                       search (highly efficient)
%               'SMALL STEPS' to use the 'smstep' small, controlled
%                 steps along the gradient (slow, but very stable)
% OUTPUTS:
%       par: the optimal parameters
%       r: the residual error
%       exitflag: the reason for exiting the optimization
% ------------------------------------------------------------------
% OPTIMIZATION OPTIONS
options.maxiter = 100;          % maximum number of iterations
options.maxfunevals = 1000;     % maximum number of function evalua-
                                                              tions
options.minchange = 0.00001;    % minimum change in objective function
                                % as a fraction of total error)
options.ind_par = 'no';      % yes to search each variable indivi-
                                                              dually
options.numgrad = 'no'; % yes if gradient provided by objective func-
                                                              tion
options.gradinc = [0.0001 0.1 0.0001 0.1 0.0001 0.1]; % increment for
                                                              gradient
                                % (only if options.numgrad = 'no').
                                % Should be the same length as par
options.bounds = 'no';          % yes turns on the bounds penalty
options.lb = [0.001 1 0.001 1 0.001 1]; % lower bound (as a penalty
                                                            function)
options.ub = [0.050 15 0.050 15 0.050 15]; % upper bound (as a penalty
                                                            function)
options.lbpen = [1e11 1e8 1e11 1e8 1e11 1e8]; % penalty mutipliers for
                                        violating lower bounds
options.ubpen = [1e10 1e7 1e10 1e7 1e10 1e7]; % penalty mutipliers for
                                        violating upper bounds


% INITIALIZE OPTIMIZATION
% create file to write iteration information
fidi = fopen('opt_iterations.txt','w');
fprintf(fidi,'Output from gmin   Date: %s\n',date);
fprintf(fidi,'Using line search method: %s\n \n',method);
fprintf(fidi,'iter | funevals |    error    |    parameters\n');
fprintf(fidi,'-------------------------------------------------->\n');
fclose(fidi);
% initialize variables
par = par_0;
iter = 0;
funeval = 0;
change = options.minchange + 1;
r = 1e20;                       % give a large starting error
```

```
last = 0;                       % for searching along individual
                                % parameters
% START OPTIMIZATION
while 1
    % call objective function at the current point
    try
        if strcmp(options.numgrad,'yes')==1
            % get gradient from objective function
            [error, gradient] = feval(obj_fun,par,…
                  options,subject,levels);
            % ------------------------------------------------------
            if iter == 0
                % print initial iteration information to text file
                fid = fopen('opt_iterations.txt','a+');
                fprintf(fid,' %2.0f    %3.0f    %5.2f   %s\n',iter,...
                    1,error,num2str(par));
                fclose(fid);
                r = error;
                % copy initial odb for visualization
                copyfile('2_load_24k.odb','starting.odb');
            end
            % ------------------------------------------------------
        elseif strcmp(options.ind_par,'yes')==1
            % get current error & calculate gradient of one parameter
            error = feval(obj_fun,par,options,subject,levels);
            % ------------------------------------------------------
            if iter == 0
                % print initial iteration information to text file
                fid = fopen('opt_iterations.txt','a+');
                fprintf(fid,' %2.0f  %3.0f  %5.2f %s\n',iter,...
                    1,error,num2str(par));
                fclose(fid);
                r = error;
                % copy initial odb for visualization
                try
                    copyfile('2_load_24k.odb','starting.odb');
                catch
                end
            end
            % ------------------------------------------------------
            % Calculate gradient for one parameter
            gpar = par;
            gpar(last+1) = par(last+1) + options.gradinc(last+1);
            ge = feval(obj_fun,gpar,options,subject,levels);
            gradient = zeros(size(par));
            gradient(last+1) = (ge - error)/options.gradinc(last+1);
            % increment the last variable searched
            if last < length(par)
                last = last + 1;
            elseif last == length(par)
                last = 0;
            end
        else % USE STEEPEST DESCENT, CALCULATE OWN GRADIENT
            % get current error & calculate numerical gradients
            error = feval(obj_fun,par,options,subject,levels);
            % ------------------------------------------------------
            if iter == 0
```

```
                % print initial iteration information to text file
                fid = fopen('opt_iterations.txt','a+');
                fprintf(fid,' %2.0f      %3.0f %5.2 %s\n',iter,...
                    1,error,num2str(par));
                fclose(fid);
                r = error;
                % copy initial odb for visualization
                try
                    copyfile('2_load_24k.odb','starting.odb');
                catch
                end
            end
            % ------------------------------------------------------------
----
            for p = 1:length(par)
                gpar = par;
                gpar(p) = par(p) + options.gradinc(p);
                ge = feval(obj_fun,gpar,options,subject,levels);
                gradient(p) = (ge - error)/options.gradinc(p);
            end
        end
        % add function evaluations to the count
        funeval = funeval + 1 + size(par,1)*size(par,2);
    catch
        exitflag = 'user supplied objective function exited with an
error';
        break
    end

    % PERFORM LINE SEARCH ALONG THE GRADIENT
    if strcmp(method,'SMALL STEPS')
        % take small steps along gradient until error goes back up
        try
            [par,e,num_evals] = smstep(par,error,gradient,obj_fun,...
                options,subject,levels);
            funeval = funeval + num_evals;
        catch
            exitflag = 'error during small steps along gradient';
            break
        end
    elseif strcmp(method,'GOLDEN')
        % use golden section line search
        try
            [par,e,num_evals] = goldenls(par,error,gradient,obj_fun,...
                options,subject,levels);
            funeval = funeval + num_evals;
        catch
            exitflag = 'error during golden section line search';
            break
        end
    end

    % UPDATE OPTIMIZATION
    iter = iter + 1;
    change = abs((r - e)/r);
    r = e;
```

```
    % print iteration information to text file
    fid = fopen('opt_iterations.txt','a+');
    fprintf(fid,' %2.0f      %3.0f      %5.2f     %s\n',iter,...
        funeval,e,num2str(par));
    fclose(fid);

    % CHECK TERMINATION CRITERIA
    if iter >= options.maxiter
        exitflag = 'exceeded maximum number of iterations';
        break
    elseif funeval >= options.maxfunevals
        exitflag = 'exceeded maximum number of function evaluations';
        break
    elseif change <= options.minchange
        exitflag = 'change in error less than tolerance';
        break
    end
end
% ------------------------------------------------------------------------

%% - GOLDEN SECTION LINE SEARCH -----------------------------------------
function [new_par,error,num_evals] = godenls(par,error,gradient,...
      obj_fun,options,subject,levels);
% Along the direction of steepest descent (gradient), the optimization
% becomes one-dimensional: only the best step along the gradient must
% be found.  This line search attempts to bracket the minimum using
% three points and then use a quadratic fit through the three points to
% estimate the best new parameter combination.  Changes in step size
% are made according to the golden ratio, which has been shown to
% maximize the convergence rate.
%
% INPUTS:
%       par: the starting parameter values
%       error: error at starting parameter values
%       gradient: a vector giving the direction to move
%           (same length as par)
%       obj_fun: function handle for objective function
% OUPUTS:
%       new_par: best parameters along the searched line
%       error: error at best parameter set
%       num_evals: number of function evaluations used
% ------------------------------------------------------------------------
% LINE SEARCH OPTIONS
max_iter = 25;                  % maximum line search iterations
i_step = 1.0;                   % initial step along gradient

% if minimizing along one parameter, get different i_step from options
if strcmp(options.conj_grad,'yes') == 1
    cur = find(gradient);
    i_step = i_step*options.gradinc(cur);
end

% INITIALIZE LINE SEARCH
par_0 = par;
e_0 = error;
```

```
num_evals = 0;
ls_iter = 0;
gold = 0.618034;                % the golden ratio
% tag evaluations file
myfid = fopen(['sub_' num2str(subject) '_evals.txt'],'a+');
fprintf(myfid,'starting golden section line search...\n',par,error);
fclose(myfid);
% start keeping a list of solutions
sol_list = [0 e_0];             % [step taken, error]

% CALCULATE ERROR AT INITIAL STEP ALONG GRADIENT
step = i_step;
par = -step*(gradient/norm(gradient)) + par_0;
error = feval(obj_fun,par,options,subject,levels);
num_evals = num_evals + 1;
% add to list of solutions
sol_list = [sol_list;step error];

% COMPARE RESULT TO ORIGINAL POINT AND GET NEXT POINT
if error <= e_0                 % not at minimum yet
    % increase step
    step = step/gold;
    myfid = fopen(['sub_' num2str(subject) '_evals.txt'],'a+');
    fprintf(myfid,'increasing step size for 2nd point...new step =
%s\n',...
        num2str(step));
    fclose(myfid);
elseif error > e_0              % went past minimum
    % decrease step
    step = step*gold;
    myfid = fopen(['sub_' num2str(subject) '_evals.txt'],'a+');
    fprintf(myfid,'decreasing step size for 2nd point...new step =
%s\n',...
        num2str(step));
    fclose(myfid);
end
% calculate error at second point
par = -step*(gradient/norm(gradient)) + par_0;
error = feval(obj_fun,par,options,subject,levels);
num_evals = num_evals + 1;
% add to list of solutions
sol_list = [sol_list;step error];

% NOW HAVE 3 POINTS - DO THEY BRACKET A MINIMUM?
cur2 = sol_list(2:3,:);
while 1
    % order mid and end points by step size
    cur2 = sortrows(cur2,1); % cur2 = [mid_step mid_e;end_step end_e]
    if cur2(2,2) == 1e10
        % the model didn't really solve, decrease step size by half
        step = cur2(2,1)*(gold/2);
        replace = 2; % replace the end point
        myfid = fopen(['sub_' num2str(subject) '_evals.txt'],'a+');
        fprintf(myfid,'decreasing step size (no solution)...new step =
            %s\n',num2str(step));
        fclose(myfid);
```

```
elseif cur2(1,2) == 1e10
    % the model didn't really solve, decrease step size by half
    step = cur2(1,1)*(gold/2);
    replace = 1; % replace the mid point
    myfid = fopen(['sub_' num2str(subject) '_evals.txt'],'a+');
    fprintf(myfid,'decreasing step size (no solution)...new step =
        %s\n',num2str(step));
    fclose(myfid);
elseif cur2(1,2) < e_0 & cur2(1,2) < cur2(2,2);
    % successful bracket of minimum
    myfid = fopen(['sub_' num2str(subject) '_evals.txt'],'a+');
    fprintf(myfid,'minimum bracketed, fitting quadratic...\n');
    fclose(myfid);
    % build list of three points for quadratic min along grad
    quad_pts = [0 e_0;cur2];
    % fit quadratic
    p = polyfit(quad_pts(:,1),quad_pts(:,2),2);
    % find quadratic minimum
    k = polyder(p);
    q_step = roots(k);
    % evaluate at suggested minimum
    q_par = -q_step*(gradient/norm(gradient)) + par_0;
    q_error = feval(obj_fun,q_par,options,subject,levels);
    % add result to list of solutions
    sol_list = [sol_list;q_step q_error];
    break
elseif cur2(1,2) < e_0 & cur2(1,2) >= cur2(2,2);
    % increase step
    step = cur2(2,1)/gold;
    replace = 1; % replace the mid point
    myfid = fopen(['sub_' num2str(subject) '_evals.txt'],'a+');
    fprintf(myfid,'increasing the step...new step =
        %s\n',num2str(step));
    fclose(myfid);
else cur2(1,2) > e_0 & cur2(1,2) < cur2(2,2);
    % decrease step
    step = cur2(1,1)*gold;
    replace = 2; % replace the end point
    myfid = fopen(['sub_' num2str(subject) '_evals.txt'],'a+');
    fprintf(myfid,'decreasing step size...new step =
        %s\n',num2str(step));
    fclose(myfid);
end
% calculate error at new point
par = -step*(gradient/norm(gradient)) + par_0;
error = feval(obj_fun,par,options,subject,levels);
num_evals = num_evals + 1;
% add to list of solutions
sol_list = [sol_list;step error];
% update list of current 2 points (mid and end points)
cur2(replace,:) = [step error];
ls_iter = ls_iter + 1;
% determine whether or not to continue
if ls_iter >= max_iter
    %tag evaluations file
    myfid = fopen(['sub_' num2str(subject) '_evals.txt'],'a+');
    fprintf(myfid,'line search iterations exceeded...\n');
```

```
        fclose(myfid);
        break
    end
end

% SELECT THE BEST RESULT (this may not always be the quadratic fit
result)
[val,ind] = min(sol_list(:,2));
best_step = sol_list(ind,1);
new_par = -best_step*(gradient/norm(gradient)) + par_0;
error = val;
%tag evaluations file
myfid = fopen(['sub_' num2str(subject) '_evals.txt'],'a+');
fprintf(myfid,'exiting the line search...\n');
fclose(myfid);
%-----------------------------------------------------------------------

%% - SMALL STEPS ALONG GRADIENT -----------------------------------------
function [par,e,num_evals] = smstep(par,error,gradient,obj_fun,...
                options,subject,levels);

% This line search takes regular steps of size 'step' along the
% gradient until the error ceases to decrease.  This is not the most
% efficient method (in terms of number of function evaluations used),
% but is inherently stable because the next set of parameters is always
% predictable.  This is important when, for example, the objective
% function calls a finite element model that may not solve if the given
% parameter set is changed excessively.
%
% INPUTS:
%       par: the starting parameter values
%       error: error at starting parameter values
%       gradient: a vector giving the direction to move
%           (same length as par)
%       obj_fun: function handle for objective function
% OUPUTS:
%       par: best parameters found along the searched line
%       e: error at best parameter set
%       num_evals: number of function evaluations used
%-----------------------------------------------------------------------
% INITIALIZE LINE SEARCH
prev_par = par;
prev_e = error;
step = 0.5; % user defined step size along gradient
e = 0;
num_evals = 0;

% start taking small steps
while e < error
    par = -step.*(gradient/norm(gradient)) + prev_par;
    e = feval(obj_fun,par,options,subject,levels);
    num_evals = num_evals + 1;
    if e >= error
        e = prev_e;
        par = prev_par;
        break
```

```
    end
    prev_par = par;
    prev_e = e;
end
%-------------------------------------------------------------------------
```

B.4 Python Scripts

```
# UPDATE_MAT ----------------------------------------------------------
# Load python libraries...
from abaqus import *
from abaqusConstants import *
import visualization

# Python function to change material parameters
def update_mat(m1, a1, m2, a2, m3, a3):
# Model variables
    CAE_file = 'Subject_2.cae'
    model = '2_mesh_24k'
    job='2_load_24k'

## UPDATE MATERIAL PROPERTIES
    # Load CAE file
    openMdb(pathName=CAE_file)

    # Update parameters

mdb.models[model].materials['muscle'].hyperelastic.setValues(table=((m1
, a1, 6.993), ))


mdb.models[model].materials['skin'].hyperelastic.setValues(table=((m2,
a2, 6.993), ))


mdb.models[model].materials['fatpad'].hyperelastic.setValues(table=((m3
, a3, 6.993), ))

## WRITE INPUT FILES
    # Run model
    try:
        mdb.jobs[job].writeInput()
    except:
        print 'Exception: Creation of input deck was unsuccessful.'

# Default runs update_mat if this script is not called as a function
if __name__ == "__main__":
    m1 = eval(sys.argv[-6])
    a1 = eval(sys.argv[-5])
    m2 = eval(sys.argv[-4])
    a2 = eval(sys.argv[-3])
    m3 = eval(sys.argv[-2])
    a3 = eval(sys.argv[-1])
         update_mat(m1, a1, m2, a2, m3, a3)
```

```
# READ_NODES-----------------------------------------------------------
# Load python libraries...
from abaqus import *
from abaqusConstants import *
from odbAccess import *
import visualization
import os

CAE_file = 'Subject_2.cae'
model = '2_mesh_24k'
job='2_load_24k'
odb_file = job + '.odb'
node_file = 'sub_2.npf'

## DELETE OLD NODE OUTPUT FILES
try:
    os.remove('sub_2.npf')
    os.remove('Displace_sub_2.npf')
    os.remove('Load_25_sub_2.npf')
    os.remove('Load_50_sub_2.npf')
    os.remove('Load_75_sub_2.npf')
    os.remove('Load_100_sub_2.npf')
except:
    print 'Exception: Could not find/delete one or more node output
files.'

## PRINT MODEL OUTPUT
# Open output database
codb = session.openOdb(name=odb_file)
session.viewports['Viewport: 1'].setValues(displayedObject=codb)

# Read node coordinates from the output database & write to text file
session.fieldReportOptions.setValues(printTotal=OFF, printMinMax=OFF)

# initial coordinates
session.writeFieldReport(fileName=node_file, append=OFF,
    sortItem='Node Label', odb=codb, step=0, frame=0, outputPosi-
tion=NODAL,
    variable=(('COORD', NODAL, ((COMPONENT, 'COOR1'), (COMPONENT,
'COOR2'), (
    COMPONENT, 'COOR3'), )), ))

# coordinates at the end of each step
for s in range(len(codb.steps)):
    stepKey = codb.steps.keys()[s]
    step = codb.steps[stepKey]
    nf = len(step.frames)
    rpt_file = step.name + '_' + node_file
    try:
        session.writeFieldReport(fileName=rpt_file, append=ON,
            sortItem='Node Label', odb = codb, step = s, frame=nf-1,
outputPosition=NODAL,
            variable=(('COORD', NODAL, ((COMPONENT, 'COOR1'),
(COMPONENT, 'COOR2'),
            (COMPONENT, 'COOR3'), )), ))
    except:
        print 'no nodal coordinates available for step [s]'
```

References

ABAQUS, 2006. Contiuum Elements. ABAQUS v6.6 Analysis User's Manual. ABAQUS Inc., Providence, RI.

ABAQUS, 2006. Hyperelastic behavior in elastomeric foams. ABAQUS v6.6 Analysis User's Manual. ABAQUS Inc., Providence, RI.

Actis, R. L., Ventura, L. B., Smith, K. E., Commean, P. K., Lott, D. J., Pilgram, T. K., and Mueller, M. J., 2006. Numerical simulation of the plantar pressure distribution in the diabetic foot during the push-off stance. Medical & biological engineering & computing 44(8), pp. 653-663.

ADA, 2002. Diabetes Statistics. http://www.diabetes.org/diabetes-statistics.jsp.

Armstrong, D. G., Peters, E. J., Athanasiou, K. A., and Lavery, L. A., 1998. Is there a critical level of plantar foot pressure to identify patients at risk for neuropathic foot ulceration? J Foot Ankle Surg 37(4), pp. 303-307.

Axel, L., Montillo, A., and Kim, D., 2005. Tagged magnetic resonance imaging of the heart: a survey. Medical image analysis 9(4), pp. 376-393.

Belegundu, A. D., and Chandrupatla, T. R., 1999. Optimization concepts and applications in engineering. Prentice Hall, Upper Saddle River, N.J., pp. 67-69.

Bosboom, E. M., Hesselink, M. K., Oomens, C. W., Bouten, C. V., Drost, M. R., and Baaijens, F. P., 2001. Passive transverse mechanical properties of skeletal muscle under in vivo compression. Journal of biomechanics 34(10), pp. 1365-1368.

Brand, P. W., 1978. Pathomechanics of diabetic (neurotrophic) ulcer and its conservative management. In: J. J. Bergan, and J. S. T. Yao eds.), Gangrene and Severe Ischaemia of the Lower Extremities. Grune & Stratton, New York, pp. 185-189.

Budhabhatti, S., Erdemir, A., and Cavanagh, P. R., 2005. Influence of Foot Orientation and Bone Structure on Plantar Pressure Distribution. XXth Congress of the International Society of Biomechanics/29th Annual Meeting of the American Society of BiomechanicsCleveland, OH.

Budhabhatti, S., Erdemir, A., Petre, M., Sferra, J., Donley, B., and Cavanagh, P. R., 2007. Finite Element Modeling of the First Ray of the Foot: A Tool for the Design of Interventions. Journal of biomechanical engineering in press.

Bus, S. A., and de Lange, A., 2005. A comparison of the 1-step, 2-step, and 3-step protocols for obtaining barefoot plantar pressure data in the diabetic neuropathic foot. Clinical biomechanics (Bristol, Avon) 20(9), pp. 892-899.

Bus, S. A., Maas, M., Cavanagh, P. R., Michels, R. P., and Levi, M., 2004. Plantar fat-pad displacement in neuropathic diabetic patients with toe deformity: a magnetic resonance imaging study. Diabetes care 27(10), pp. 2376-2381.

Cavanagh, P. R., 1999. Plantar soft tissue thickness during ground contact in walking. Journal of biomechanics 32(6), pp. 623-628.

Chen, W. P., Ju, C. W., and Tang, F. T., 2003. Effects of total contact insoles on the plantar stress redistribution: a finite element analysis. Clinical biomechanics (Bristol, Avon) 18(6), pp. S17-24.

Chen, W. P., Tang, F. T., and Ju, C. W., 2001. Stress distribution of the foot during mid-stance to push-off in barefoot gait: a 3-D finite element analysis. Clinical biomechanics (Bristol, Avon) 16(7), pp. 614-620.

Chen, Y., 2003. The influence of diabetes on mechanical properties of skin. Doctoral, Cleveland State University, Cleveland.

Cheung, J. T., An, K. N., and Zhang, M., 2006. Consequences of partial and total plantar fascia release: a finite element study. Foot & ankle international / American Orthopaedic Foot and Ankle Society [and] Swiss Foot and Ankle Society 27(2), pp. 125-132.

Cheung, J. T., and Zhang, M., 2005. A 3-dimensional finite element model of the human foot and ankle for insole design. Archives of physical medicine and rehabilitation 86(2), pp. 353-358.

Cheung, J. T., Zhang, M., Leung, A. K., and Fan, Y. B., 2005. Three-dimensional finite element analysis of the foot during standing--a material sensitivity study. Journal of biomechanics 38(5), pp. 1045-1054.

Cheung, Y. Y., Doyley, M., Miller, T. B., Kennedy, F., Lynch, F., Jr., Wrobel, J. S., Paulson, K., and Weaver, J., 2006. Magnetic resonance elastography of the plantar fat pads: Preliminary study in diabetic patients and asymptomatic volunteers. Journal of computer assisted tomography 30(2), pp. 321-326.

Davis, B. L., 1993. Foot ulceration: hypotheses concerning shear and vertical forces acting on adjacent regions of skin. Medical hypotheses 40(1), pp. 44-47.

Delbridge, L., Ctercteko, G., Fowler, C., Reeve, T. S., and P., L. Q. L., 1985. The aetiology of diabetic neuropathic ulceration of the foot. Britsh Journal of Surgery 72(1), pp. 1-6.

Dinh, T. L., and Veves, A., 2005. A review of the mechanisms implicated in the pathogenesis of the diabetic foot. The international journal of lower extremity wounds 4(3), pp. 154-159.

Elgort, D. R., and Duerk, J. L., 2005. A review of technical advances in interventional magnetic resonance imaging. Academic radiology 12(9), pp. 1089-1099.

Erdemir, A., Saucerman, J. J., Lemmon, D., Loppnow, B., Turso, B., Ulbrecht, J. S., and Cavanagh, P. R., 2005. Local plantar pressure relief in therapeutic footwear: design guidelines from finite element models. Journal of biomechanics 38(9), pp. 1798-1806.

Erdemir, A., Viveiros, M. L., Ulbrecht, J. S., and Cavanagh, P. R., 2006. An inverse finite-element model of heel-pad indentation. Journal of biomechanics 39(7), pp. 1279-1286.

Garrow, A. P., van Schie, C. H., and Boulton, A. J., 2005. Efficacy of multilayered hosiery in reducing in-shoe plantar foot pressure in high-risk patients with diabetes. Diabetes care 28(8), pp. 2001-2006.

Gefen, A., 2003. Plantar soft tissue loading under the medial metatarsals in the standing diabetic foot. Medical engineering & physics 25(6), pp. 491-499.

Gefen, A., Megido-Ravid, M., Azariah, M., Itzchak, Y., and Arcan, M., 2001. Integration of plantar soft tissue stiffness measurements in routine MRI of the diabetic foot. Clinical biomechanics (Bristol, Avon) 16(10), pp. 921-925.

Gefen, A., Megido-Ravid, M., Itzchak, Y., and Arcan, M., 2000. Biomechanical analysis of the three-dimensional foot structure during gait: a basic tool for clinical applications. Journal of biomechanical engineering 122(6), pp. 630-639.

Gooding, G. A., Stess, R. M., Graf, P. M., Moss, K. M., Louie, K. S., and Grunfeld, C., 1986. Sonography of the sole of the foot. Evidence for loss of foot pad thickness in diabetes and its relationship to ulceration of the foot. Investigative radiology 21(1), pp. 45-48.

Gooding, G. A., Stress, R. M., Graf, P. M., and Grunfeld, C., 1985. Heel pad thickness: determination by high-resolution ultrasonography. J Ultrasound Med 4(4), pp. 173-174.

Goske, S., Erdemir, A., Petre, M., Budhabhatti, S., and Cavanagh, P. R., 2006. Reduction of plantar heel pressures: Insole design using finite element analysis. Journal of biomechanics 39(13), pp. 2363-2370.

Hall, O. C., and Brand, P. W., 1979. The etiology of the neuropathic plantar ulcer: a review of the literature and a presentation of current concepts. Journal of the American Podiatry Association 69(3), pp. 173-177.

IWGDF, 2005. Practical Guidelines - Pathophysiology. http://www.iwgdf.org/index.php?option=com_content&task=view&id=29&Itemid=57.

Jacob, S., and Patil, M. K., 1999. Stress analysis in three-dimensional foot models of normal and diabetic neuropathy. Front Med Biol Eng 9(3), pp. 211-227.

Landsman, A. S., Meaney, D. F., Cargill, R. S., 2nd, Macarak, E. J., and Thibault, L. E., 1995. 1995 William J. Stickel Gold Award. High strain rate tissue deformation. A theory on the mechanical etiology of diabetic foot ulcerations. Journal of the American Podiatric Medical Association 85(10), pp. 519-527.

Lavery, L. A., Higgins, K. R., Lanctot, D. R., Constantinides, G. P., Zamorano, R. G., Athanasiou, K. A., Armstrong, D. G., and Agrawal, C. M., 2007. Preventing diabetic foot ulcer recurrence in high-risk patients: use of temperature monitoring as a self-assessment tool. Diabetes care 30(1), pp. 14-20.

Ledoux, W. R., and Blevins, J. J., 2007. The compressive material properties of the plantar soft tissue. Journal of biomechanics ePud Ahead of Print(Apr 11).

Lemmon, D., Shiang, T. Y., Hashmi, A., Ulbrecht, J. S., and Cavanagh, P. R., 1997. The effect of insoles in therapeutic footwear--a finite element approach. Journal of biomechanics 30(6), pp. 615-620.

Maciejewski, M. L., Reiber, G. E., Smith, D. G., Wallace, C., Hayes, S., and Boyko, E. J., 2004. Effectiveness of diabetic therapeutic footwear in preventing reulceration. Diabetes care 27(7), pp. 1774-1782.

Madsen, M. T., Haller, J., Commean, P. K., and Vannier, M. W., 2000. A device for applying static loads to prosthetic limbs of transtibial amputees during spiral CT examination. Journal of rehabilitation research and development 37(4), pp. 383-387.

Matricali, G. A., Dereymaeker, G., Muls, E., Flour, M., and Mathieu, C., 2006. Economic aspects of diabetic foot care in a multidisciplinary setting: a review. Diabetes Metab Res Rev.

Miller-Young, J. E., Duncan, N. A., and Baroud, G., 2002. Material properties of the human calcaneal fat pad in compression: experiment and theory. Journal of biomechanics 35(12), pp. 1523-1531.

Mueller, M. J., Lott, D. J., Hastings, M. K., Commean, P. K., Smith, K. E., and Pilgram, T. K., 2006. Efficacy and mechanism of orthotic devices to unload metatarsal heads in people with diabetes and a history of plantar ulcers. Physical therapy 86(6), pp. 833-842.

Ogden, R. W., 1984. Non-Linear Elastic Deformations. Ellis Horwood Limited, Chinchester.

Oomens, C. W., Bressers, O. F., Bosboom, E. M., Bouten, C. V., and Blader, D. L., 2003. Can loaded interface characteristics influence strain distributions in

muscle adjacent to bony prominences? Computer methods in biomechanics and biomedical engineering 6(3), pp. 171-180.

Pecoraro, R. E., Reiber, G. E., and Burgess, E. M., 1990. Pathways to diabetic limb amputation. Basis for prevention. Diabetes care 13(5), pp. 513-521.

Perry, J. E., Hall, J. O., and Davis, B. L., 2002. Simultaneous measurement of plantar pressure and shear forces in diabetic individuals. Gait & posture 15(1), pp. 101-107.

Petre, M., Erdemir, A., and Cavanagh, P. R., submitted 2007. Determining Foot Tissue Material Properties from an MRI Deformation Experiment. Journal of biomechanics.

Petre, M., Erdemir, A., and Cavanagh, P. R., submitted 2007. An MRI-Compatible Foot-Loading Device for Assessment of Internal Strain. Journal of biomechanics.

Petre, M., Tokar, P., Kostar, D., and Cavanagh, P. R., 2005. Revisiting the total contact cast: maximizing off-loading by wound isolation. Diabetes care 28(4), pp. 929-930.

Petre, M., Wyllie, J., Sferra, J., Donley, B., Erdemir, A., Doehring, T., Considine, J., Thangudu, P., and Cavanagh, P. R., 2006. Normal sesamoid motion during first MTPJ dorsiflexion. American Academy of Orthopaedic Surgeons Annual MeetingChicago, IL.

Petre, M. T., Erdemir, A., and Cavanagh, P. R., 2006. Determination of elastomeric foam parameters for simulations of complex loading. Computer methods in biomechanics and biomedical engineering 9(4), pp. 231-242.

Reeder, S. B., and Faranesh, A. Z., 2000. Ultrafast pulse sequence techniques for cardiac magnetic resonance imaging. Top Magn Reson Imaging 11(6), pp. 312-330.

Reger, S. I., McGovern, T. F., and Chung, K. C., 1990. Biomechanics of Tissue Distortion and Stiffness by Magnetic Resonance Imaging. In: D. L. Badel (ed. Pressure Sores - Clinical Practice and Scientific Approach. Macmillan Press, London.

Reiber, G. E., 2001. Epidemiology of foot ulcers and amputations in the diabetic foot. In: J. H. Bowker, and M. A. Pfeifer eds.), The Diabetic Foot. Mosby, St Louis, MO, pp. 13-32.

Ribu, L., Hanestad, B. R., Moum, T., Birkeland, K., and Rustoen, T., 2007. A comparison of the health-related quality of life in patients with diabetic foot ulcers, with a diabetes group and a nondiabetes group from the general population. Qual Life Res 16(2), pp. 179-189.

Smith, K. E., Commean, P. K., Mueller, M. J., Robertson, D. D., Pilgram, T., and Johnson, J., 2000. Assessment of the diabetic foot using spiral computed tomography imaging and plantar pressure measurements: a technical report. Journal of rehabilitation research and development 37(1), pp. 31-40.

Smith, R. L., Rusk, S. F., Ellison, B. E., Wessells, P., Tsuchiya, K., Carter, D. R., Caler, W. E., Sandell, L. J., and Schurman, D. J., 1996. In vitro stimulation of articular chondrocyte mRNA and extracellular matrix synthesis by hydrostatic pressure. J Orthop Res 14(1), pp. 53-60.

Spears, I. R., Miller-Young, J. E., Sharma, J., Ker, R. F., and Smith, F. W., 2007. The potential influence of the heel counter on internal stress during static standing: A combined finite element and positional MRI investigation. Journal of biomechanics.

Thompson, D. E., 1988. The effects of mechanical stress on soft tissue. In: M. E. O. N. Levin, L W (ed. The Diabetic Foot. CV Mosby, St. Louis.

Ulbrecht, J. S., Cavanagh, P. R., and Caputo, G. M., 2004. Foot problems in diabetes: an overview. Clin Infect Dis 39 Suppl 2, pp. S73-82.

Veress, A. I., Gullberg, G. T., and Weiss, J. A., 2005. Measurement of strain in the left ventricle during diastole with cine-MRI and deformable image registration. Journal of biomechanical engineering 127(7), pp. 1195-1207.

Veves, A., Murray, H. J., Young, M. J., and Boulton, A. J., 1992. The risk of foot ulceration in diabetic patients with high foot pressure: a prospective study. Diabetologia 35(7), pp. 660-663.

Weaver, J. B., Doyley, M., Cheung, Y., Kennedy, F., Madsen, E. L., Van Houten, E. E., and Paulsen, K., 2005. Imaging the shear modulus of the heel fat pads. Clinical biomechanics (Bristol, Avon) 20(3), pp. 312-319.

Wu, J. Z., Dong, R. G., Smutz, W. P., and Schopper, A. W., 2003. Nonlinear and viscoelastic characteristics of skin under compression: experiment and analysis. Bio-medical materials and engineering 13(4), pp. 373-385.

Yarnitzky, G., Yizhar, Z., and Gefen, A., 2006. Real-time subject-specific monitoring of internal deformations and stresses in the soft tissues of the foot: a new approach in gait analysis. Journal of biomechanics 39(14), pp. 2673-2689.

Yuan, Y., and Verma, R., 2006. Measuring microelastic properties of stratum corneum. Colloids and surfaces 48(1), pp. 6-12.

Zobitz, M. E., Luo, Z. P., and An, K. N., 2001. Determination of the compressive material properties of the supraspinatus tendon. Journal of biomechanical engineering 123(1), pp. 47-51.